Electrical Resistance Tomography for sewage flow measurements

Wu, Chenning

Award date:
2020

Awarding institution:
University of Bath

Electrical Resistance Tomography for sewage flow measurements

Submitted by

Chenning Wu

For the degree of Doctor of Philosophy

University of Bath

Department of Electronic and Electrical Engineering

Abstract

Sewage network management is critical to efficiently collecting and transporting wastewater; thus requires proper monitoring schemes. Electrical resistance tomography (ERT) has been reported in many industrial applications due to its high temporal, low cost, non-invasive, and non-radiation emitting features. In this thesis, an ERT system is developed for monitoring sewage flow to allow for further system automation and control. A bespoke ERT data acquisition device, which cost much less than the current commercially available ERT devices, was firstly developed and tested in the lab-scale experiments,. The performance of the ERT device was demonstrated in both the static and dynamical scenarios, proving its capability in capturing flow behaviours. Particularly, the functional ERT method was exploited to extract dynamic information by combining time-series of ERT measurements. Such method allows for the visualization of flow dynamics as well as the estimate of flow velocities. In addition, the system was also evolved for operating in horizontal partially filled pipes, where free flowing sewage happens. The major problem related to the partially full flow is that some electrodes lose contact with the fluid and hence results in erronueous measurements. This problem raises the following two challenges: 1) we need to recognize and eliminate the erronueous data points; 2) we need to reconstruct images with the resultant incompete datasets. The former criteria was met by modifying the ERT data acquisition hardware in the way that it can detect the non-contact electrodes. A localized ERT imaging method was proposed originally to improve the spatial resolution for frequency difference ERT problems so that ERT could be adopted as a guiding tool in lung tumour tracking applications. This localized image algorithm was then applied to the deal with the incomplete datasets to enhance the image reconstruction and robustness of the ERT system; hence tackles the second challenge involved in the part full flows. This ERT wastewater metering development aims to achieve as cost effective as the traditional flowmeters but can provide visualized monitoring which can be interpreted into flowrate, gas/liquid/solid distribution, and conductivity.

Acknowledgements

First and foremost, I would like to thank my supervisor Prof Manuchehr Soleimani for his invaluable support and encouragement throughout my entire PhD study. His enthusiasm in research and abundant knowledge have always inspired and motivated me. Over half of my PhD journey did not happen on campus and I definitely would not have come this far without his consistence motivation and guidance.

Secondly I need to give a lot of praise to people from Ashridge engineering Ltd, whom I worked closely with on daily basis. Each person during my time at Ashridge has helped me on the project as well as make the office a fun place to work. A special mention to Mr Martin Hutton who is my line manager at the company as well as my project industrial supervisor. He has been there teaching me practical engineering skills and giving me opportunities for my exposure within the industry.

Next I would like to thank Innovate UK for funding the Knowledge Transfer Partenership project and everyone involved in this project. Their support has helped me in not only just funding, but also through them I have collaborated with the company as well as other people. This has been extremely crucial to my personal development.

Of course, the rest of the ETL group as well as my friends from the university of Bath couldn't go without mention. They have made my time in Bath such a joyful memory and passively imparted their own small part on my development.

Last but not the least, massive thanks to my parents. Most of my academic years have been entirely supported by them and I would never have been where I am without them. So truly thank you for being there through my ups and downs and always believing in me.

List of figures

List of tables

List of Abbreviations

AMP	Asset management period
CC	Correlation Coefficient
ECT	Electrical Capacitance Tomography
EIT	Electrical Impedance tomography
ERT	Electrical Resistance Tomography
FEM	Finite Element Method
MIT	Magnetic Induction Tomography
NOSER	Newton's One-Step Error Reconstructor
PE	Position Error
RE	Relative Error
RES	Resolution
SBTV	Split Bregman Total Variation
SD	Shape Deformation
SNR	Signal to Noise Ratio
SVD	Singular Vector Decomposition
TV	Total Variation
ROI	Region of Interest
MRI	Magnetic Resonance Imaging
CT	Computed Tomography
HMI	Human Machine Interface
PET	Positron Emission Tomography
tdEIT	Time Difference Electrical Impedance Tomography
fdEIT	Frequency Difference Electrical Impedance Tomography
EIDORS	Electrical Impedance and Diffuse Optical Tomography
GWFD	Global Weighted Frequency Difference
MGWFD	Modified Global Weighted Frequency Difference
ROI_WFD	Limited region Weighted Frequency Difference

Contents

Chapter 1 Introduction and motivation

Electrical Impedance tomography (EIT) is a recently established form of impedance mapping technique. Electrical resistance tomography is a particular case of EIT, which only considers the real part of the complex impedance within the view region. It approximates for the internal resistvity distribution by computing based on the knowledge of the injected currents and measured voltages on the boundary of the domain. Since the method was proposed, its low cost, non-invasive features have made the technology attractive compared to the conventional X-ray tomography systems. In particular, one of its biggest advantages is the high data capture speed, which cannot be achieved using other hard-field techniques such as magnetic resonance imaging and ultrafast ray. However, the major downside of ERT is that its spatial resolution is not comparable to structural imaging techniques because of its severe ill-posed nature. Therefore, extensive research has exploited its temporal advantages such that serial ERT data/images can be synthesized to unveil the time-correlated information in the dynamical context where the internal conductivity distribution changes rapidly. In these cases, instead of focusing on individual images, information can be obtained from functional ERT by applying a mathematical operation on a sequence of images and the corresponding pixel waveforms. For instance, EIT has been developed as a real-time monitoring tool in clinical applications to quantify lung collapse, tiddal recuitment, and lung overdistnesion to titrate positive end expiratory pressure and tidal volume [1] by visualizing local ventilation and lung perfusion distribution[2-6]. In the industial scenario, dynamical imaging plays an important role in determining flow regimes and velocity profiles in the slurry transportation processes as well as flow distribution monitoring involved in mixing processes [7]. This thesis aims to research the use of ERT imaging system for the application in sewage flow measurements.

1.1. Background of sewer

The modern sewer system is responsible for ensuring that wastewater is transported and treated correctly. The development of UK sewer systems can date back to 3200 BC, when signs of early drainage systems appeared in Scotland. However, most of these primitive systems had numerous flaws

which caused cholera epidemics and foul odours. From 43 to 410 AD, Romans occupied Britain and introduced their advances in cleanliness, including public bathhouses, complex drainage systems, latrines and aqueducts. A fall in standards comes with the end of the Roman Empire and a basic sewer system existed in London in the 1550s in the form of open ditches running into the river Thames. Little else was then done to transform the sewerage system until 1800s, when the outbreak of several cholera epidemics occurred. A much more effective system that revolutionised the way we disposed of waste in the UK was established by Joseph Bazalgette and it was quickly adopted throughout the country thereafter[8].

The way modern sewer networks work is summarized below and can be visualized in Figure 1.1:

- Wastewater disposed of from households are channeled into underground foul water drains and sewers. Separate drains and sewers are used for collecting surface water, including rainwater and melted ice, and transporting it back to the rivers and seas.

- The foul water is taken to water treatment stations, where several cleaning processes, including screening, primary treatment, secondary treatment, and final treatment, take place.

- After the water has been treated, it is usually returned to rivers and streams. At the same time, the sludge collected along the process can also be recycled to agricultural land as fertiliser as well as be used to generate energy.

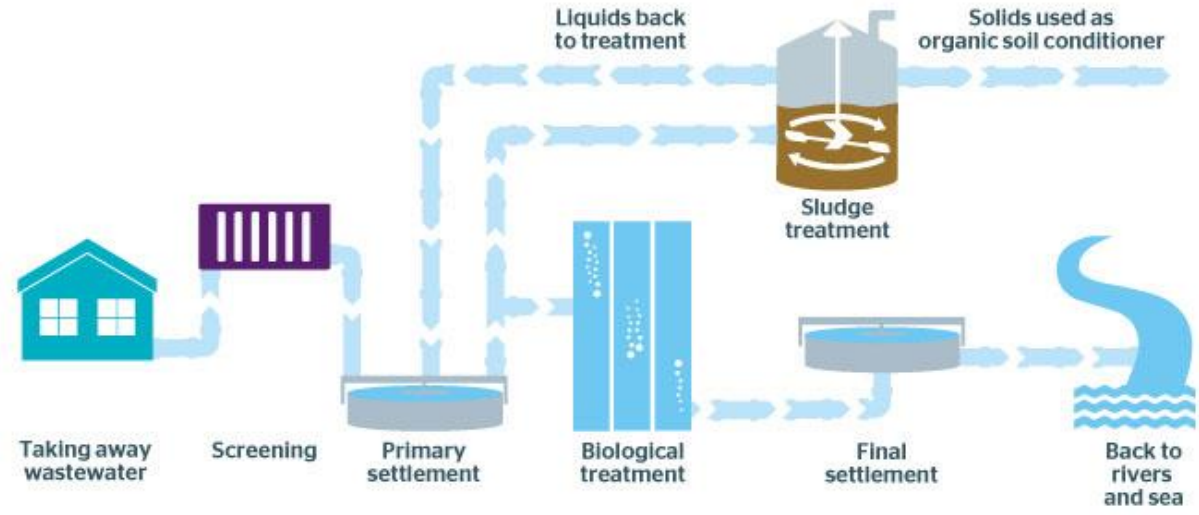

Figure 1.1 Typical sewer system processes [9]

Every day in the UK about 347,000 kilometers of sewers collect over 11 billion litres of wastewater. Sewer flooding is a key measure because it is one of the worst service failures customers can suffer. In 2016-16, 37,434 areas were externaly flooded and 4,344 properties were internally flooded by sewage[10]. Sewer flooding can occur due to blocked or broken sewer lines, inflitration of excessive stormwater or malfunction of pumps. About 75% of sewer blockages are caused by putting unsuitable products down the sink or toilet, such as fat oils and grease or accumulation of flushed wet-wipes and other ‘non-woven’ textiles. In these cases, untreated sewage is discharged into not only the houses but also the environment prior to reaching sewage treatment facilities. Untreated spills and overflows from the wastewater network to the environment can pose risks to public health and the environment.

To avoid this, sewers need to be regularly cleaned, maintainted and kept free of blockages and defects wherever possible. Operators of sewer networks aim to continually improve the management of their assets to deliver better customer services and reduce the risks of environmental incidents such as flooding and outflow events, against a backdrop of increasing pressures from climate change and urbanisation. Effective monitoring, real-time data and reliable networking are driving a transformation in the way sewers are managed.

1.2. Motivation

Developing integrated and collaborative drainage and wastewater monitoring system to improve the sewer asset management is still remaining a challenging topic. There are growing interests in remote sensing methods for wastewater storages; on the other hand local in-situ sensors are explored and used in sewage transportation systems. Currently, various technologies are available to perform the monitoring activities, including both sampling and chemical testing in laboratories and on-site inspections. Sewerage is an instrinsically complex system given the constituent flowing inside and the various sewerage constructions, it is an usual practice to incorporate multiple technologies into one system or sometimes, one device. Such integration, however, can complicate design as well as maintenance, and hence increase the expenses.

Considering the limitations of the current sewer flow measurement solutions, process tomography techniques have emerged to offer alternative solutions for wastewater monitor. Tomographic devices provide the real time concentration distribution and allow for the visualization of the flows inside pipes. Nevertheless, they are still at the stage of research; and the devices used are not explicitly designed for the waste flow, of which the costs are not comparable with the existing sewer measuring equipments. The idea of this study comes from the fact that wastewater flow is essentially multiphase flow; hence the study advances and transfers the previous understanding of process tomography for multiphase flow analysis.

1.3. Aims and objectives

This thesis aims to explore the use of electrical resistance tomography technology as a potential wastewater smart meter in order to meet requirements of wastewater flow measurements. ERT has mainly been developed for process flow studies, which shares some similarity with the sewer flows but with very different cost factors to those required in sewer flow measurements. So the aim of this thesis is to develop a bespoke low-cost ERT system specifically tailored for smart wastewater metering. The associated objectives are:

1. Develop a low cost ERT hardware device for flow measurements;

2. Evaluate the dynamical imaging capability of the proposed ERT sensor;

3. Investigate incomplete data problems associated with partially full pipes and improve image reconstruction techniques specifially for recovering inclusions in part full pipes.

1.4. Thesis Organisation

The work can be separated into three main topics following the proposed objetives: the ERT hardware development (Chapter 4); ERT dynamical imaging analysis (Chapter 5); partially full pipe investigation and the associated image reconstruction enhancement (Chapter 6 and 7). The contents of each chapter are summarized as follows:

Chapter 2 presents a literature review of sewer systems, flow measurements and ERT. It firstly reviews the principle of how sewer networks operate together with common problems that need urgent attention. Following that, the existing technologies involved in measuring different aspects of sewage flows are outlined. The other focus of this chapter is to introduce the role of ERT in measuring process flows, especially multiphase flows, and how it could be distinguished from other electrical tomographic systems. This then could help guide the development of one ERT system for exploring specific properties of the mixture in sewers.

Chapter 3 introduces the mathematics behind the ERT reconstruction problems, starting with the formulation of an ERT model based on Maxwell's equations. The forward problem is then established concerning different electrode models and is solved using the finite element method. Different imaging algorithms are reviewed considering the system operating scenarios, for example, total variation is employed when sharp boundary preservation is desired; and temporal one-step solver is applied to the dynamical movement imaging. Quantitive indexes for image quality evaluation that will be used throughout the work are also described in this chapter.

Chapter 4 details the development of an ERT data acquisition system dedicated in wastewater metering applications. The design specifications are reviewed and how the design of each module within the device reflects on them are also explained. The overall system performance is demonstrated by lab-based tests in both dynamical and static setups; and results are presented and analysed in this chapter.

Chapter 5 follows chapter 4 and investigates the dynamical imaging aspect of the proposed ERT system. It shows that the temporal resolution can facilitate the functional imaging which combines the information of a series of measurements and compensates for the low spatial resolution of one system. We specifically performed a 2.5 dimentional (2.5D) visualization of dynamical movements and the velocity calculation of these movements in 2D prelimitary phantom tests. The visualization is demonstrated by an in-water handwriting practice where time-series ERT images can recover letters written in a water-based ERT phantom. Flow velocities are explicitly performed which contributes to the flow metering requirements of monitoring sewage systems.

Chapter 6 describes the development of a limited region reconstruction method. This method was developed for imaging local changes within a pre-defined region of interest (ROI). It was developed in the context of tumour tracking applications where the ROI could be determined by a hard-field imaging technology. Naturally, frequency difference data was used for reconstruction due to the lack of time reference data in this application. As the conductivity changes caused by frequency changes are not as noticeable as those by inserting inclusions, the localized method can also be applied to enhance the system immunity to noises in a time difference system.

Chapter 7 addresses the problem arisen from the part full pipe flows, that is, some electrodes will lose contact with the fluid. The problem is then resolved by firstly modifying the hardware to allow for detecting electrode absences. Then these correponding measurements are eliminated from the datasets, resulting in an incomplete dataset. The reduced available data can further make the image reconstruction more ill-posed, so the localized imaging method developed from Chapter 6 is applied to enhance the image qualities.

1.5. List of publications

A number of publications have been made which are directly related to some of the Chapters as part of the project. They are:

- *'**Implementation of low cost Electrical impedance tomography hardware system**'[11]* was presented at 2018 World Congress of Industrial Process Tomography 9 (WCIPT9) in Bath, UK.
- *'**Smart water meter using Electrical Resistance Tomography**'[12]* follows up the first conference paper and was published in Sensor, which forms a majority part of the work in Chapter 4 as well as part of Chapter 5.
- *'**In-water handwriting in multi-medium using electrical impedance imaging**'[13]* was accepted in IOP SciNotes. This work was built upon together with some work from[12] to form Chapter 5.
- ***Frequency difference EIT with localization: A Potential Medical Imaging Tool during Cancer Treatment**'[14]* was published in Early 2019, which created a localized imaging method to enhance reconstruction quality in the context of medical applications. This work contributes to Chapter 6.
- *'**Limited Angle Electrical Resistance Tomography in Wastewater Monitoring**' [15]* was published again in Sensor. It incorporates the method developed in [14] into the ERT device designed in [12] to tackle the incomplete data issue arisen from part full pipe flow.
- ***'Ionic liquid based distributed touch sensor using electrical impedance tomography'** [16] was published in IOP SciNotes. This work hasn't contributed to the thesis but has demonstrated the capability of the proposed ERT device in different applications.*

Chapter 2 Literature reviews

This chapter mainly explores how tomographic approaches can be adopted for monitoring wastewater flow. Firsly, the sewer systems operation principles are briefly explained, which reveals the importance of monitoring the processes. Next, this chapter gives an overview of the capabilities of different electrical tomographic sensors and then examines their applications for specific sensing tasks. Following that, the discussion is focused on reported applications of ERT in multiphase flow measurements. The purpose is to obtain how these establishments can assist sewer flow measurements with two underlining parameters, namely flow velocity and flow regime. Last but not the least, this chapter will address the basic ERT operation principles together with the elementary functions of the ERT data acquisition systems. Sensor designs suited for the various specific applications are also demonstrated here.

2.1. Sewer flow measurement

The ability to meet the future demand for water in the face of increasing hydrological variability will depend on not only the water quantity but also the quality. Sewage is generally a mixture of domestic wastewater from baths, sinks, washing machines and toilets, industrial wastewater and rainwater run-off from roads and other surfaced areas. Proper collection, treatment and discharge of sewage help protect and improve water quality. Effective wastewater treatment is designed to remove various contaminants of sewage solids, pathogens, nutrients, toxic chemicals and metals so that treated wastewater can be returned to the environment. The other by-product of sewage treatment is sewage sludge, which needs to be appropriately re-utilized or disposed of [17]. A sewer system comprises a network of pipelines and technical installations. The system collects and transports waste and stormwater from more than one source to wastewater treatment plant or receiving water. Sewer systems are mostly gravity fed, which means that the pipes slope downward from the source to the sewer mains; this type of system is called gravity main. In every sewer main, there are periodical vertical pipes that meet the ground with manholes. These are access points that are needed when a problem arises in the

sewer main. In the scenario where, for example, the wastewater treatment plants are placed in high-lying areas, then grinder pumps or lift stations are used to push the sewage up to the needed levels; and this is called rising main. This process is energy intensive and there are several factors that would impact the performance of the system as a whole, such as the material, length and topography.

Generally, the main physical components of sewage are: cellulose material (paper, sanitary towels, rags etc.); rubber/plastic; solids (faeces) and water based conveying liquid. They can cause severe blockages if not treated properly and these blockages within the sewer network can cause a whole lot of problems and need to be promptly dealt with. There are approximately 300000 sewer blockages every year, costing £100 million clearing blockages in the UK[18]. As a result, thousands of properties suffer sewer flooding caused by these blockages every year, leading to high clean-up bills and increased insurance costs. Water companies are now looking for new ways of reducing blockages, and thus the chances of flooding. These means include modelling to identify hot-spots, monitoring for progressive operational deterioration, and intervening proactively [19]. It has been concluded through statistical analysis that the majority of blockages occur in pipes of diameter 225 mm or less and mostly upstream of a junction [20]. Moreover, the flow velocities can affect the risk of blockages, vice versa. Therefore, flow monitoring at the locations with high likelihood of blockages is essential for continuously inspecting the sewer and identifying the intermittent sewer blockages. Timely identification of the location and the state of developing blockages are key to proactively address this problem.Heavy rainfall is another common cause for sewage flooding. Though weirs inside the sewers permit any excess to overflow and divert into rivers, such overflow can pose significantly damaging effect onto the local river ecosystem. Hence, the sewage network need to be properly monitored to ensure optimal operations and thus reducing the chances of potential flooding [21].

Flow and load surveys can also play an important role in planning for a new wastewater treatment build scheme. Moreover, it can help examine the existing sites where works are failing and a remedial solution is required. The current UK investment cycle for the water industry is from 2020-2025 (AMP7), during which the water authorities' goal is to encourage water companies to adopt methods to increase lifetime of pipes rather than replacement.

Thanks to the advancement in the recent system digitalisation, data from on-line instrumentation is increasingly being used for process optimization and control and for moniotirng compliance critical operations. Various on-line intrumentations are introduced to accomplish a wide range of flow measurement tasks and to further manage risks, maximise efficiency and provide the business with reliable information. In sewage processes, flow monitoring devices aim to measure scalar parameters such as flow level, flowrate, temperature, pressure, etc, so that we can make sure that the fluid is at the right place and the right time. For example, level monitoring and control is a fundamental requirements in protecting tank overfill and monitoring combined sewer overflow. Hydrostatic pressure sensors, ultrasound transmitters, microwave (radar) transmitters, and capacitive sensors are commonly used in level measurement applications [22]. Flowrate is another parameter that could indicate the violation of low and high flow conditions. Sewers must accommodate for a wide range of flow rates over the course of a day, especially for the peak flow rate, as flow quantities depend upon population density, water consumption and the extent of commercial or industrial activity in the community [23]. The flowrate measurements are typically achieved by flow meters such as ultrasonic Doppler velocity profilers, electromagnetic meters, Coriolis mass meters, and Venturi meters, which are commercially available from [22, 24-26].

Another example of process improvement has been developed within the field of chemicals. Conductivity is a measure of the ability of fluid to pass electrical currents. This ability is directly linked to the concentration of ions in the fluid, which comes from, for example, dissolved salts and inorganic materials. Obviously, the more ions present, the higher the conductivity of water, vice versa. Within sewerages, conductivity fluctuation can be caused by the changes in fluid temperature, water level, as well as the salinity levels or total dissolved solids [27]. Hence, conductivity has been introduced as one of the most useful and commonly measure that can be used as an early indicator of changes in a water system[28-30]. Consequently, natural flooding, evaporation or man-made pollution that can detriment water quality, can be reflected on the significant changes in conductivities, whereas bodies of water maintain a fairly constant conductivity that can be used as a baseline of comparison to future

measurements. Currently, a conductivity sensor that has been incorporated in multiparameter sensing system to monitor water quality within the process are commercially available [31-33].

In recent years, efforts have been focused on creating a smart water network, which aims at helping the utility system as a whole make better and more efficient decisions based on the information from a well-integrated multisensing system. For example, the SMART Sewer from em-solutions proposed to 'Detect blockages before they become flooding events' by deploying a wireless communication enabled level monitor into the wastewater network and working together with an Artificial Intelligence analysis engine [34]. Another completion of installing a smart sewer system in the City of South Bend, Indiana, US was made. It is a network of depth sensors, flow sensors, and smart valves that measures water levels and redirect wastewater from trunk lines approaching capacity to less stressed lines[35].

2.2. Process tomography

Measurements of the flow and position of fast moving components in industrial mixture and processes can be technically challenging due to the materials, safety and cost. The tomographic imaging of objects offers an unique opportunity to unfold the complexities of structure without the need to invade the object. The development of tomographic instrumentation started in the 1950s and has led to the widespread availability of body scanners. Significant advances have promoted process tomography into the mainstream as an industrially deployable technique. Tomographic approaches aim to derive data taken from multiplicity of sensors observing different attributes of a process; and obtain a rich dataset of measurements that detail the particular properties of the mixture within the process. Process tomography has been applied to imaging of mixing processes, separators, chemical reactors, and industrial pipelines and vessels[36]. The goal of process tomography has been to sense and interpret complex data in order to extract qualitative and quantitative information of the behavior of fluids moving within processes. Dynamic behaviours are commonly sought from which temporal properties of the process can be deduced. In all applications, there is trade-off between the spatial and temporal resolution.

Two different approaches have been used to derive information from tomographic measurements as illustrated in Figure 2.1. In the case of Figure 2.1 (a), measurements are reconstructed to produce visualization and the resultant images are then interpreted to obatian further information, such as fluid velocity. On the other hand, Figure 2.1(b) presents a second method where parameters are directly interpreted from the measurements via direct feature extractions and then visualization can be provided if required.

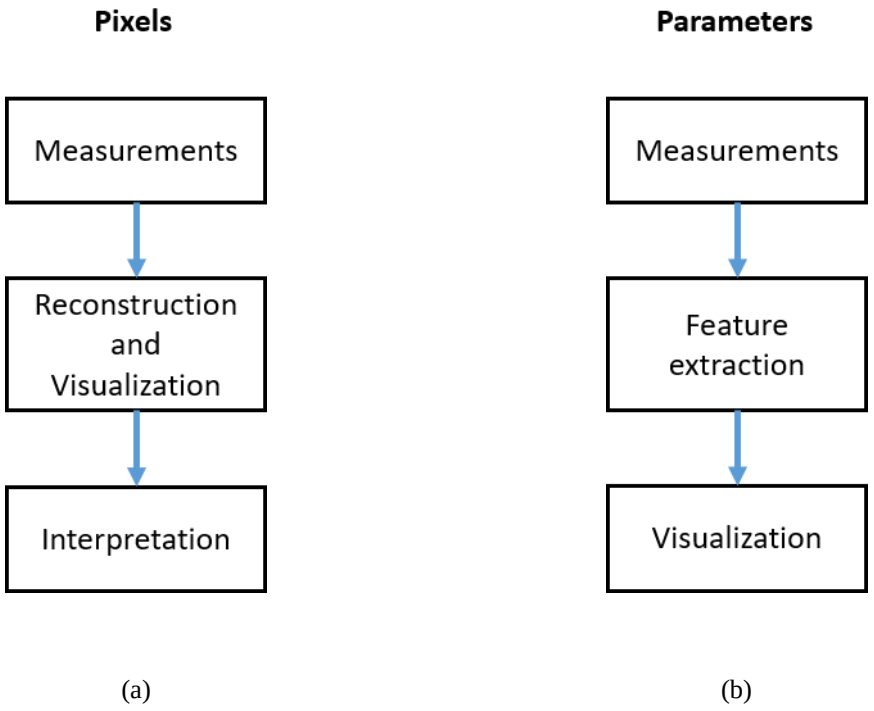

Figure 2.1 Approaches to ERT measurement analysis[37]

Tomography is defined as a method of producing an image (2D cross section or a 3D distribution) of an object by combining the measurements obtained from the use of penetrating signals. There are two main broad types of tomography:

Hard-field Tomography: is when the direction of travel of energy waves through the viewing area is constant. Hence, the image is built up as a result of the distortion of the waves caused by the objects. Some well-known imaging techniques, such as X-ray computed tomography and Magnetic Resonance Imaging (MRI), fall in this category.

Soft-field Tomography: Other factors can influence the transmitting signal, such as the distribution of the electrical parameters inside and outside the view region. The examples of such tomographic systems include Electrical Impedance Tomography (EIT), Electrical Capacitance Tomography (ECT), Magnetic Induction Tomography (MIT). The characteristic of soft-field tomography poses difficulties on computing the image reconstruction algorithm. Several Imaging modaltities have been used in process tomogarphy, among which the most common approaches having been related to electromagnetic probing. They are capacitance, impedance and electromagnetic induction tomography. ERT is a particular case of EIT when only the in-phase voltages are measured given stimulation currents; thus, the real component of the complex impedivity is considered as the dominant property of materials. A list of reported applications using these electrical tomography are presented in Table 2.1.

Table 2.1 Recent reported applications of electrical tomography

Process	Modality	Status
Hydrocyclone monitoring[38] Monitoring pressure filtration[39]	EIT	Industrial tests
Nylon polymerization[40] Nuclear waste site charaterization[41] Waste storage ponds[42] Subsurface resitivity[43] Leaks in burried pipes[44]		Field tests
Bubble column dynamics Foam density distribution[45] Mixing in stirred vessel[46] Slurry transport [47] Blast furnace – hearth wall thickness[48]		Laboratory tests
Bead milling [49]	ECT	Industrial tests

Pneumatic conveying [50] Density flowmeter [51]		
Flame monitoring [52] Fluidized beds [53] Bubble column dynamics [54] Powder flow in dipleg [55] Belt conveyor [56] Solid rocket propellant [57] Imaging wet gas		Laboratory tests
Onset of crystallization in steel production Flow of molten steel[58]	MIT	Industrial tests
Metal solidification [59]		Theoretical

2.2.1. Electromagnetic induction tomography

Electromagnetic Induction Tomography, more commonly known as magnetic induction tomography (MIT), is an imaging technique that maps all the passive electrical properties (i.e. conductivity, permeability, and permittivity) of a material. MIT operates by exciting the region of interest with an oscillating magnetic field generated from alternating current flowing through coils. The measurements can capture the modifications of the targeting field caused by the changes of the material distribution within the view region. MIT does not require electrical contacts with the object, hence is known as non-invasive and non-intrusive modality.

MIT sensors are used on a wide variety of materials including metals, aqueous fluids and biological tissues. It has been applied to a variety of applications, most of which has been in either medical imaging that examines cross-sectional images of the human body, or in non-destructive evaluations (NDE) for visualizing and monitoring the distribution of material in vessels and pipelines.

The major factor that differs MIT from the other electrical methods is in the operation of the sensor array, and there are two key issues associated with it: the use of coils; the requirements of magnetic screening can be considered to be more troublesome than electrical [60].

2.2.2. Electrical Capacitance Tomography

Electrical Capacitance Tomography (ECT), as suggested by the name, involves the reconstruction of the dielectric distribution in an imaging domain from a set of measurements taken at the domain boundary. ECT was developed in the early 1980's, firstly used for flow imaging in multi-phase pipe flow. In contrast to EIT, electrodes are often located outside the vessel making the technique non-invasive as well as non-intrusive. The favorable features of ECT sensors for these applications are the non-invasive nature of the sensing mechanism, the fast imaging speed, safe to use, sensor flexibility for fitting around any vessel geometry, and low cost.

However, ECT has its limitations, among which is the low spatial resolution. This is because the measured capacitance variations in flow systems are typically very small and there is need for a minimum electrode plate area to provide sufficient signal to noise ratio for the reception signals; hence, the number of independent measurements that ECT sensors can provide is limited. Also, ECT systems are primarily applied for permittivity distributions in flow systems involving low conductive materials.

2.2.3. Electrical Resistance Tomography

Different materials display different electrical properties, so a map of resistivity can be used to infer the internal structure in Ω. Therefore, ERT is an imaging tool with important applications in the fields of medicine, geophysics, environmental sciences and nondestructive testing of materials. In medical applications, ERT can be used to detect pulmonary emboli, monitor apnoea, monitor heart function and blood flow, and detect breast cancer. In geophysics and environmental sciences, ERT can be useful for locating underground mineral deposits detection of leaks in underground storage tanks and for monitoring flows of injected fluids into the earth, and environmental cleaning. Finally, in nondestructive

testing, ERT can be used for the detection of corrosion and of small defects, such as cracks or voids, in metals.

2.3. ERT in sewer monitoring

Domestic sewage contains approximately 99.9% water and the remaining includes organic and inorganic, suspended and dissolved solids, together with microorganisms. The composition of the wastewater is clearly a function of the uses to which the water was subject. Depending on the particular locations of interest as well as the condition of the flow, sewage flow can be mainly considered as either two-phase flow, e.g. air-liquid flow, or three phase flow, e.g. air-liquid-solids flow. Therefore, the sewage flows are essentially multiphase flows. The problems associated with monitoring sewage flows are therefore similar to those that involved in the multiphase flow processes. Attempts of developing ET based device for monitoring sewage processes has been made. For example, ECT was introduced to monitor wastewater infiltration where the filtration membrane cleaning service is triggered when the ECT detects the impurity accumulation area exceeding a certain level[61]. Another example uses ERT to study the infiltration in the land application system of a wastewater treatment plant, in which the water content changes was obtained by tracking the resistivity changes in ERT profiles[62]. ERT has also been applied for monitoring batch mixing involved in wastewater treatment process- water aeration. It provides an opportunity in understanding, optimising and controlling mixing through monitoring changes in concentration of different materials[63].

When considering the feasibility of adopting ERT system for monitoring sewerage flow, we need to refer to the Monitoring Certification Scheme established by the environmental agency to ensure quality environmental measurements [64]. The minimum rate operating conditions for fluid conductivity are regulated to be 50 µS/cm to 1200 µS/cm. It also sets the requirements for a flowmeter designed to operate in a partially filled pipe under free surface flow conditions that fill levels should be between 15% and 85% of the pipe diameter.

2.3.1. ERT in Multiphase flow

Liquid, gas, and solids are three forms of substances in nature, known as phases; and the classification of flows depends on the combination of phases, namely single-phase flow, multiphase flow. Obviously, multiphase refers to more than one phase emerging simultaneously. Examples of their use include energy generating processes, food processing, chemical reactor processes, and pharmaceutical processes. Multiphase flow is a common but complex phenomenon as the phase distribution and the velocity profiles vary significantly with fluid properties, operating conditions and geometry of the flow pipes [65]. Measurement techniques in two-phase flows are very different from those employed in single-phase flows. In fact, some peculiar quantities existing in the multiphase flow, such as, the void fraction and the interfactial area concentration, require specifically designed instruments. The ability to image multiphase flow interactions in real time has always been a highly desirable capability to further understand the complex dynamics among interacting phases in any flow system. Many flow maps were originally constructed on the basis of results obatained by flow visualization and the measurement of void or pressure fluctuations by using an intrusive point sensor. The main drawbacks of these methods are the application of the sensors, which disturb the flow field, and the use of subjective criteria to distinguish the boundaries between various flow patterns.

In recent developments, multiphase flow measurement is commonly realized by process tomography such that the tomographic images contributes to, for example, identifying the various flow patterns, phase distribution, and velocity profiles. Generally, two topologies of multiphase flow can be usefully identified at the beginning, namely disperse flows and seperated flows. Disperse flows concern those consisting of finite particles, drops or bubbles distributed in a connected volume of the continuous phase. On the contrary, the seperated flows consist of two or more continuous streams of different fluids separated by interfaces. It is worth noting that ERT only produces electrical conductivity distribution. Therefore, theses conductivity-based information obtained from ERT systems needs to be interpreted to relevant engineering data.

ERT has been heavily applied in multiphase flow studies by the means of estimating the phase fraction through the mixture's dielectric properties of fluid [66, 67] without distorting the flow field, including identifying the flow regimes [68-70], visualizing multiphase flow [71, 72], mass flow rate measurement [73]. Additionally, ERT sensors can estimate the velocity profiles by cross-correlation between two identical sensors [74, 75]. Some mature applications using ERT as a sensing tool are listed in Table 2.2.

Table 2.2 Multiphase flow measurement in industrial applications using ERT

Measured parameters	**Multiphase**	**Feature**
Oil/water two phase flow patterns in horizontal pipe[76]	Oil/water	Multivariate maximum Lyapunov exponent extraction
Disperse phase veloity and instantaneous flow rate[77]	Gas/liquid	Dual-plane ERT system combined with cross-correlation technique
Gas/oil/water distribution, optimal frequency[78]	Gas/oil/water	ECT/ERT dual modality
Multiphase flowrate[79]	Gas/liquid	Accurate multiphase flowrate realized by using a slotted orifice plate
Flow regime in horizontal pipeline, e.g. slag, plug and wavy flow[80]	Gas/liquid	Proper orthogonal decomposition method
Gas concentration and velocity distributions[67]	Gas/liquid	High conductive multiphase flow
Liquid distribution in a lab scale trickle bed reactor[81]	Gas/water/solid	Boundaries of flow regime transition were identified and pulsing flow velocity was estimated

2.3.2. Flow parameters

Flow parameters, which are computed from measurements provided by tomographic systems, have been developed to help build mathematical flow models and quantatitively understand the flow behaviours. In this section, we will summarize key flow parameters that could be particularly desired in sewage flow metering application, i.e. the volumetric flowrate and the flow patterns in horizontal pipelines. In

sewage piping and pumping system, the flow velocity must be kept within certain limits operation and to avoid solids settling and sedimentation, as well as potential wear and tear due to abrasion; ultimately sewage flowrate needs to monitored to maintain to ensure sewer function. Flow patterns is another key measure that can influence the multiphase pressure drop, holdup, system stability, exchange rate of momentum, and heat and mass during the phase-change heat transfer processes[82]. Thus, it is vital to analyse the flow patterns encountered in sewer flow for understanding the flow phenomena. In this section, we will focus on two-phase flow, which is one of the most common flows in nature as well as in industrial applications.

2.3.2.1. Flow rate

Obviously, one of the general requirements for a flowmeter is that one should show either the totalised volume and/or volumetric flow-rate, particularly in gas/liquid or oil/liquid flows. ERT has been developed for making volumetric flowrate measurements, i.e. volume (m^3) of liquid in unit time (s), in two-phase flows. Here we take an example of gas-liquid flow where liquid is the continuous phase and gas is disperse phase. In a dual-plane ERT system, where two planes of ERT electrodes are spaced apart in the stream-wise direction, in order to measure the volumetric flowrate of gas, Q_g (in m^3) in the pipe, the phase distribution α_g (no unit) and the local axial velocity v_g (in m/s) of the gas phase in the cross section are obtained; and Q_g can be deducted following:

$$Q_g = \int \alpha_g v_g dA \tag{2.1}$$

where *A* represents cross sectional area (in m^2). (2.1) can be extended to

$$Q_g(t) = \iint \alpha_g(x,y,t) v_g(x,y,t) dxdy \tag{2.2}$$

where $\alpha_g(x,y,t)$ denotes the gas void fraction at location (x,y) within the flow cross section in the pipe at time t, $\alpha_g(x,y,t) \in [0,1]$; $v_g(x,y,t)$ represents the axial velocity of the gas phase at location (x,y) in the flow at time t [83].

The flow can then be further classified into two categories based on the dispersed phase distribution, i.e. uniform and non-uniform. And the methods to calculate the flow velocities and void fraction involved in the two types of flows are pixel-correlation method and eigenvalue-correlation method respectively. In the sewer flow applications, we are more interested into the non-uniform flow. Hence, we define the unit number that the measured cross section is plotted out into, N, and (2.2) can be expressed as:

$$Q_g(t) = \sum_{n=1}^{N} \alpha_n(t) \cdot v_n(t) \cdot A_n \tag{2.3}$$

Where A_n is the area of the unit n; $\alpha_n(t)$ is the void fraction of the unit n at time t. $v_n(t)$ can be obtained by cross-correlation.

2.3.2.2. Local volume fraction distribution

Volume fraction (or sometimes void fraction) is another important parameter in studying multiphase flows. This can help unveil the concentration of solids in the stationary bed type of flows, or/and the water level in the stratified flows. A general local volume fraction distribution α_d can be determined indirectly from the conductivity distribution by applying Maxwell's equation. Equation shown below describes the disperse phase fraction [84]:

$$\alpha_d = \frac{2\sigma_1 + \sigma_2 - 2\sigma_m + \frac{\sigma_m \sigma_2}{\sigma_1}}{\sigma_m - \frac{\sigma_2}{\sigma_1} + 2(\sigma_1 - \sigma_2)} \tag{2.4}$$

Where σ_1 is the conductivity of the first phase, σ_2 is the conductivity of the second phase, and σ_m is the local mixture conductivity distribution determined from either image reconstruction or a data processing method.

Equation (2.4) has been proved good agreement with experimental data over a wide range of void fraction. Generally, it can be simplified if the second phase is assumed to be non-conductive, such as debris or air:

$$\alpha_g = \frac{2\sigma_1 - 2\sigma_m}{\sigma_m + 2\sigma_1} \quad \textbf{(2.5)}$$

Such simplification ignores the temperature as well as the ionization process that change the conductivity of the dispersed phase, e.g. gases.

2.3.2.3.Local velocity profile

Velocity field can be obtained via changes of some other quantity, such as concentration distribution under the influence of the velocity field; this is called indirect approach. One of the most well-known indirect method in process tomography is the cross-correlation velocimetry, which infers the fluid axial velocity based on cross-correation between signals measured at different positions (e.g. upstream and downstream) of a pipeline. In Figure 2.2 an example of a commonly used dual-plane tomography system can demonstrate such cross-correlation based velocimetry principle. The intended velocity limits would affect the placement of sensor arrays, i.e. L, together with the desired data acquisition speed of a tomography system. Especially, the targeting objects need to be successfully captured by the sensing arrays; hence the minimum time allowed for the objects to travel from one array to another is limited by the time interval of two successive tomography scans. For a given maximum velocity of a targeting flow system, v_{max}, the traveling time over a distance of L is L/v_{max}. Consequently, the data collection speed will then need to meet v_{max}/L.

There are two types of correlation methods: the pixel-correlation method and the eigenvalue-correlation method, shown in Figure 2.3. The pixel-correlation method suggests that a sequence of tomographic images from two or more sensor arrays are collected and the velocity can be computed based on cross-correlation between the pixel values in two images, as shown in Figure 2.4. Figure 2.4 displays the discretized cross-sections, in which the object moves from A(x_1, y_1) to B(x_2, y_2). The correlation function

can be applied to extract the transit time and hence the resultant velocities. On the other hand, the eigenvalue based method correlates extracted features, which is obtained from the mean value and the variance of the boundary measurements. This method avoids the image reconstruction and can be faster but lack of distributed velocity visualization. These two methods reflect the two approaches to synthesize ERT measurements conveyed in Figure 2.1.

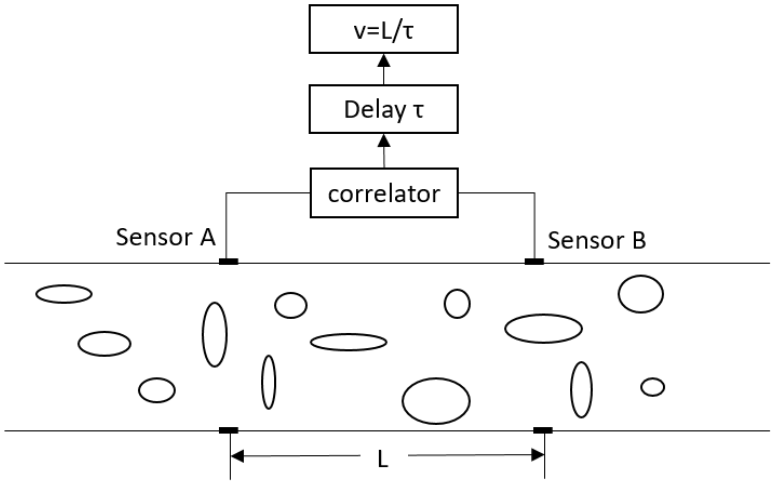

Figure 2.2 Dual plane ERT velocity measurement of two-phase flow

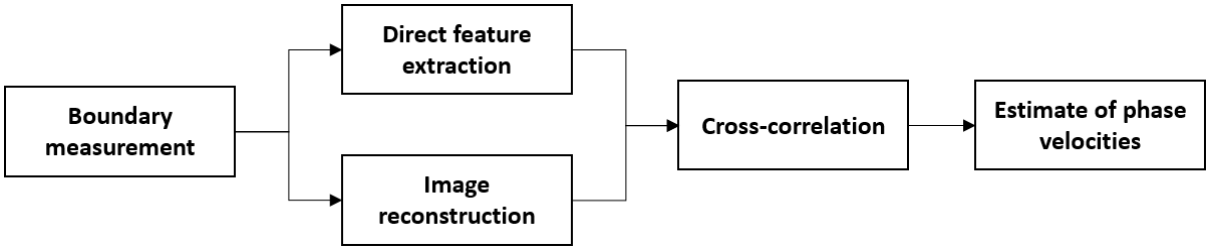

Figure 2.3 Two approaches to estimate velocities

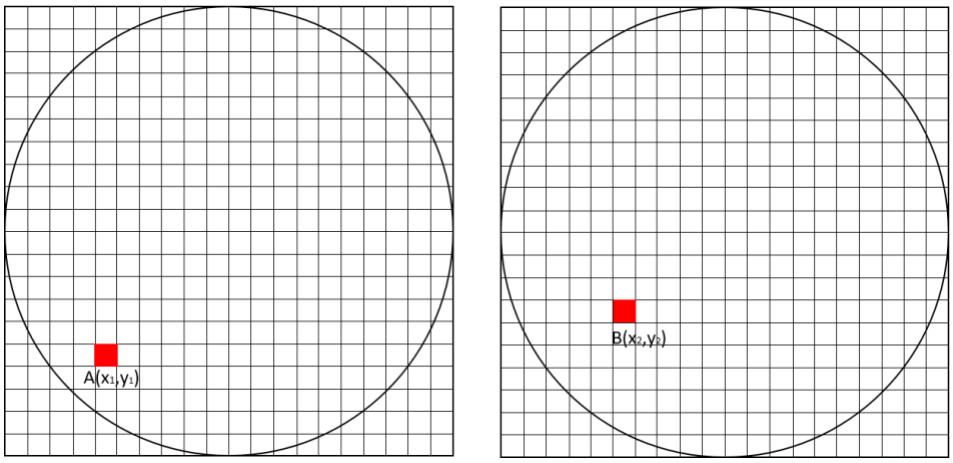

Figure 2.4 The principle of the pixel-based cross-correlation velocity calculation method

2.3.2.4. Flow regime

A particular type of geometric distribution of the components is called a flow pattern or flow regime. the flow regime actively depends on a number of factors: the fluid tranport and material properties, flow rates, flow direction, the shape and size of the vessel, and the orientation (vertical, horizontal and inclined). Studying flow patterns is important to understand the flow behaviours and unveil the potential problems one system may have. ERT has been heavily investigated to identify flow regimes in multiphase flows thanks to its high temporal speed and visualization capability. Simailarly to the velocity computation, the flow regime identification can also be solved by vision based and non-vision methods. The former approach achieves the flow regime recognition by analyzing dynamically reconstructed ERT images whilst the latter applies feature extraction technique on ERT raw data[69, 85]. This feature extraction technique compensate for the long processing time involved in the image reconstruction; however, is more applicable for stable and simple two-phase flows. Some typical horizontal two-phase models are summarized below:

1. Air-liquid two phase flow pattern

Figure 2.5 illustrates the definition of different flow regimes for the flow of an air/liquid mixture in a horizontal pipe. In general, the flow pattern are primarily dependent on the relative amount of gas and liquid and the local phase velocities. When small bubbles are dispersed in the liquid phase and their velocities are fairly uniform, this is called dispersed flow. As the quantity of bubbles increases, small bubbles join together and form a bubble flow. If the bubbles keep developing into even larger bubbles such that sequences of liquid slugs followed by longer gas bubbles flow through the pipes, this is called slug flow. When the liquid flows at the bottom of the pipe with gas at the top, the flow patterns are catergorized stratified or wavy flows considering the interface.

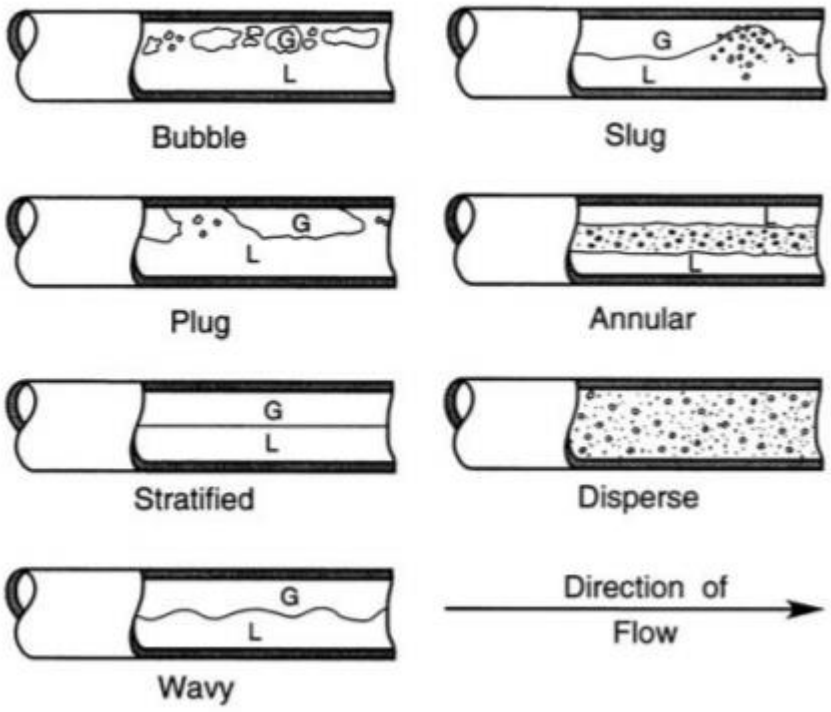

Figure 2.5 Sketches of flow regimes for flow of air/water mixtures in a horizontal pipe [86]

2. Solid-liquid two phase flow pattern

Figure 2.6 concerns the flow regimes of slurry (solid/liquid mixture) flows in a horizontal pipeline. Homogeneous flow occurs when the particles are small so that their settling velocity is much less than the turbulent mixing velocities in the fluid and the flow is well-mixed. When larger particles are present, vertical gradients will occur in the concentration and the regime is termed heterogeneous. This heterogeneous regime can turn into a saltation flow when the some particles settle and form a packed bed at the bottom of the pipe whilst some particles are in suspension.

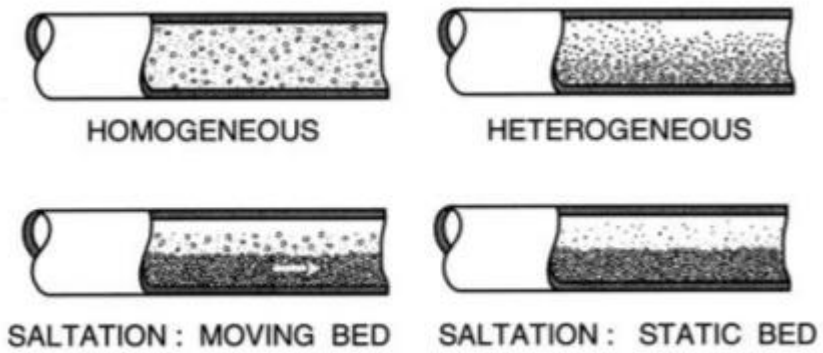

Figure 2.6 Flow regimes for slurry flow in a horizontal pipeline [86]

2.4. EIT hardware system reviews

EIT is a well-established modality aimed at mapping the internal conductivity distribution within a domain. The first commercial EIT system was reported in the early 1980s for medical use and was referred to as the Sheffield APT (applied potential tomography). An EIT system designed for biomedical imaging inherently requires different specifications from the one for process engineering imaging. For example, the strength of injection currents needs to be small to ensure the safe operation for clinical use, whereas this is not a concern when designing for industrial applications. Also, most medical application oriented designs prefer multi-frequency operation so that the frequency-varying impedance of bio-material can be studied. Yet a process tomography system normally considers the optimal frequency which could achieve a high framerate; this can significantly simplify the system architecture. The first commercial EIT for process application was launched in 1997, referred to as Manchester system[87]. Since then EIT instruments have evolved with advances in analogue and digital electronics. There are a wide variety of hardware systems that have been designed and built with varying degrees of success for both biomedical research and process engineering, listing in Table 2.3 below.

Table 2.3 Review of the existing commercial and academic EIT systems

System	No. of Electrodes	frame speed (fps)	Frequency (Hz)	Excitation	DAQ method	Application areas
Sheffield Mk1 [88]	16	16	50kHz	Single current	Analogue	Biomedical
Sheffield MK3.5 [89]	8	25	Multi 2k-1600k	Single current	Digital	Biomedical
KHU Mark 2.5 [90]	16	Up to 100	Multi 10-500k	Single currents	Analogue	Biomedical
Dartmouth High-speed EIT [91]	32	<100	Multi 10k-10M	Multiple currents/ voltages	Analogue	Biomedical
ACT-III [92]	32	480	30k	Multiple currents	Digital	Biomedical

OXPACT [93]	32	25	10k, 40k, 160k	Multiple currents	Digital	Biomedical
ACE1[94]	32	<33.2	<200		Analogue	Biomedical
MARK I-b[87]	16	20	1.2k-72.8k	Dual currents	Analogue	Process engineering
FIC (University of Leeds) [95]	Dual plane 16 each	1000	10k-320k	Dual currents	Digital	Process engineering
Tianjin University design [71]	16	1041	50k	Single current	Digital	Process engineering
The university of Cape Town system [96]	16	1000	n/a	Single current	Analogue	Process engineering

Several commercial EIT devices are currently available and being used in ICUs: ulmovista® 500 (Dräger Medical GmbH, Lündbeck, Germany), Goe-MF® II (CareFusion - Becton, Dickinson and Company, San Diego, United States), Mark 1® and Mark 3.5® (Maltron International Ltd, Rayleigh, United Kingdom), BB® (Swisstom AG, Landquart, Switzerland) and Enlight® (Timpel S/A, Sao Paulo, Brazil)[97]. A few EIT systems have also been commercially developed for industrial solutions, such as Displacement Current Phase Tomography system from Tech4Imaging [98], Rocsole EIT pipe sensor [99] and the itoms FLOW-ITOMETER EIT sensors[100].

An important charateristic of one device that could fundamentally impact the trade-off between the complexity and the performance is the excitation source. The common approach in EIT systems is to inject current and to measure voltages on the surface electrodes as opposed to applying voltages and measuring currents. This method reduces the effect of contact impedance on voltage measurements due to the high input impedance of the voltage measurement system. The EIT system can be categorized based on the number of stimulating sources either as a single driver system or a multiple driver system. In the single source systems, a current flow is generated by using one pair of electrodes and the resulting voltages are then measured between pairs of the remaining electrodes. Consequently, the current source is then switched to another pair of electrodes and the voltages measurements repeat until a complete set of measurements are collected. The most widely used single source EIT systems are the Sheffield EIT data-collecting systems, MARK 1, MARK 2 and MARK 3 [88, 101, 102]. On the other hand, in a

multiple driver system, current fields are established by driving multiple electrodes simultaneously while voltage measurements are made at all or an selected set of electrodes. The sum of currents from all active sources should ideally be zero at all time such that currents injected into the active electrodes have to sink from anther active electrodes. There are a few exisiting systems that use multiple sources, such as Oxford Brookes systems (OXPACT-II, OXPACT-III) and Dartmouth systems. Both theory and practice have shown that a multiple source system can provide better precision data than a single source system for the same number of electrodes. This is due to the fact that the single source configuration needs multiplexers to switch the current source between electrodes which will introduce the significant shunting capacitance. Another advantage of using multiple sources is that it reduces the sensitivity of data to errors in electrode placement. However, the multiple source intruments clearly compromise hardware simplicity for performance. In the industial applications, where the imaging resolution does not matter as much as it would in medical applications, single source instruments are the most favourable. In order to speed up the data transmission that a system can operate in real-time, attempts of using multiple voltmeters to undertake voltage measurements at receiving electrodes simultaneously have been made in a few single source ERT systems that are termed 'parallel' systems.

Another factor that could determine the ERT imaging quality is the current driving pattern. Current patterns that can result in good image reconstructions should meet the following criterions: 1) it can provide more independent measurements; 2) the boundary voltage must be as large as possible and meanwhile the voltage dynamic voltage should be compressed properly; 3) electric field built within the region should be as even as possible. Researchers have proposed many current drive patterns, in which the most commonly used are adjacent, cross and opposite for single source driving topology. With the adjacent pair strategy, current is applied between adjacent electrode pairs and voltages are measured between every other pair of adjacent electrodes. In a typical 16 electrode sensing system shown in Figure 2.7, the first current is injected into the electrode pair (1,2), and voltages are measured at the remaining electrodes between adjacent pairs (3,4), (4,5) … (15,16). Then the injection electrodes shift to the next pair (2,3) and voltages are taken at electrode pairs starting from (4,5) to (16,1). This process is repeated for all current driving pairs and forms a total of $N_E \times (N_E - 3)$ measurements, i.e.

208, in one frame of data. The adjacent electrode pair mechanism is now widely used due to the high signal to common voltage ratio, high number of independent measurements and simplicity of hardware and software implementation.

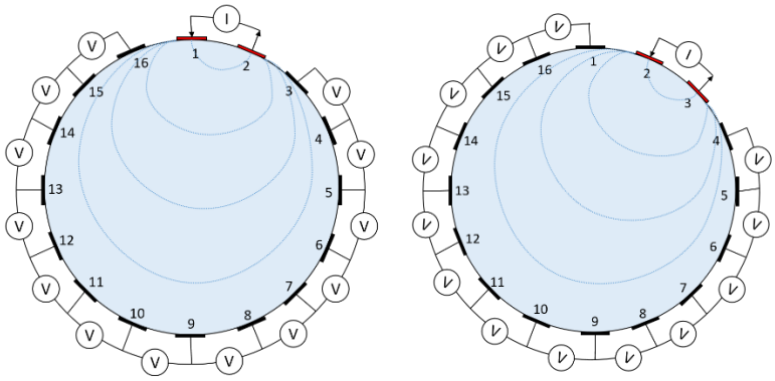

Figure 2.7 Adjacent current pattern

The main difference between the adjacent and the opposite driving strategies is that, in the latter, currents are injected between diametrically opposite electrode pairs rather than between adjacent electrode pairs. This gives rise to a relatively higher current flow through the centre of the vessel and therefore a bettern uniformity across the whole region. In the example shown in Figure 2.8, currents are injected into the opposite electrode pairs (1, 9), (2, 10) … (8,16), and under each injection voltages are meaured from the the rest of the electrodes against a chosen electrode. For instance, for a current injected via (1, 9), electrode 2 is selected as the reference electrode, and voltages between (2, 3), (2, 4), …, (2, 16) are collected. In total, $(N_E - 3) \times N_E/2$ measurements make up one frame of data, of which half are independent of one another. Obviously, the opposite method has fewer available independent measurements for the same number of electrodes in comparison to the adjacent method, which will worsen the ill-posedness of image reconstruction.

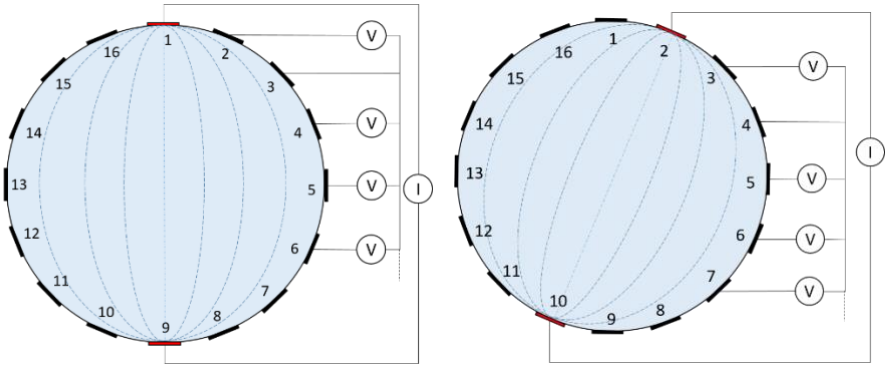

Figure 2.8 Opposite current pattern

Chapter 3 EIT computational methods

Tomography intends to image the cross-section of an object without altering it. For a given domain under known boundary conidtions, the measured electrical singals are determined only by the electrical property distribution over the domain. Sophisiticated computational and modeling methods should be applied to extract information of interest. ERT is a particular case of EIT, hence in this chaper, we will explain the mathematics behind general EIT problems, including the formulation of a forward model, regularization related with ill-posed inverse problems. Particularly, the most widely used L2 norm regularization, Tikhonov algorithm, and L1 norm regularization, Total variation algorithm, are discussed in depth. In addition, the temporal one step solver is also unfolded to solve the dynamical problems that are involved in process flows. Last but not the least, several image quality parameters, which attribute the analysis of reconstructions throughout the work, will be explained.

3.1. EIT reconstruction

The EIT reconstruction problem is to obtain an approximation to the interior conductivity distribution from the boundary measurements. Methods of EIT imaging can be divided into absolute imaging and difference imaging. In absolute imaging problem, the conductivity distribution is estimated using one set of boundary measurements, and at the instance of measuring the conductivity model is invariant. The realization of absolute imaging is very sensitive to the ubiquitous modeling errors which can result from inaccurate knowledge of auxiliary model parameters, such as contact impedances, electrode positions and boundary of the target. On the other hand, a change in the conductivity is estimated in the difference imaging based on datasets measured either at different time instances (time-difference) or stimulation frequencies (frequency-difference). The main advantage of the difference imaging is that the global modeling errors can be cancelled by the subtraction of the datasets. The image reconstruction in difference imaging is conventionally carried out using linear approach.

3.1.1. Forward problem

As mentioned previously, EIT is a type of soft-field tomography, which means that the current injected into the object scatters and causes uncertain voltage changes on the boundary. In practice, changes in the conductivity distribution can causes arbitrary responses

to boundary voltage measurements at a given precision.Therefore, finding the conductivity distribution requires the simultaneous equations relating to every voxel or pixel for the entire system. To solve the inverse problem, a forward model needs to be set up for some assumed conductivity so that the predicted voltages can be compared with the measured data.

In the EIT forward problem, the excitation currents and the conductivity distribution of a domain are known, then the potential distribution of the same domain is desired. A MATLAB based free toolkit called Electrical Impedance Tomography and Diffuse Optical Tomography Reconstruction Software (EIDORS) is used to solve the forward problem throughout this research.

3.1.1.1. Mathematical model

The EIT forward problem is established from the basic Maxwell's equations of electromagnetics, which models the electric field $\boldsymbol{E}$ and the magnetic field $\boldsymbol{H}$ as functions of space and time:

$$\nabla \times \boldsymbol{E} = -\frac{\partial \boldsymbol{B}}{\partial t}$$
$$\nabla \times \boldsymbol{H} = \frac{\partial \boldsymbol{D}}{\partial t} + \boldsymbol{J} \qquad \textbf{(3.1)}$$

where $\boldsymbol{D} = \varepsilon \boldsymbol{E}$ is the electric flux density and $\boldsymbol{B} = \mu \boldsymbol{H}$ is the magnetic flux**.** $\boldsymbol{J}$ is the current density and is composed of the conducting current density $\boldsymbol{J_c} = \sigma \boldsymbol{E}$ and the internal source current density $\boldsymbol{J_s}$.

Now we will consider a sinusoidal excitation, $\boldsymbol{E}(\boldsymbol{x}, t) = Re(\boldsymbol{E}(\boldsymbol{x})e^{i\omega t})$, where $\boldsymbol{E}(\boldsymbol{x})$ is a complex function of space. Then the time harmonic Maxwell's equations become:

$$\nabla \times \boldsymbol{E} = -i\omega\mu \boldsymbol{H} \qquad \textbf{(3.2)}$$

$$\nabla \times \boldsymbol{H} = i\omega\varepsilon\boldsymbol{E} + \boldsymbol{J} = (\sigma + i\omega\varepsilon)\boldsymbol{E} + \boldsymbol{J_s} \quad \textbf{(3.3)}$$

Considering the operation frequencies for process imaging, which are typically within the range of 10kHz to 200kHz, quasi-static can be assumed. Under such quasi-static assumption, the domain can be approximated as constant field such that direct currents are assumed for simplification. Therefore, magnetic part in (3.2), $-i\omega\mu\boldsymbol{H}$, together with $i\omega\varepsilon$ in (3.3) is negligible. Also, the EIT target region typically has no internal source, which brings $\boldsymbol{J_s}$ to zero. And now (3.2) and (3.3) can be rewritten as:

$$\nabla \times \boldsymbol{E} = 0 \quad \textbf{(3.4)}$$

$$\nabla \times \boldsymbol{H} = \boldsymbol{J} = \sigma\boldsymbol{E} \quad \textbf{(3.5)}$$

$\boldsymbol{E}$ is obtained from the gradient of the voltage:

$$\boldsymbol{E} = -\nabla u \quad \textbf{(3.6)}$$

According to Kirchhoff's current law, the net current leaving a junction of a network of conductors is zero which can be stated as:

$$\nabla \cdot \boldsymbol{J} = 0 \quad \textbf{(3.7)}$$

Substituting equation (3.5) into (3.6) and taking the divergence in accordance with (3.7), gives the voltage distribution in the medium:

$$\nabla \cdot (\sigma\nabla u) = 0 \quad \textbf{(3.8)}$$

Equation (3.8) sets up the forward model that describes the electric potential u within inside the body with a given conductivity distribution σ.

3.1.1.2. Boundary conditions:

Equation (3.8) above describes the potential field within a medium given the potential measurements $u|_{\partial\Omega}$ on the boundary, which is specified by Dirichlet Boundary Condition. The term Dirichlet

boundary condition means that the condition involves the value of the solution itself on the boundary. Hence, it suggests that the voltage on the electrode is the voltage measured on that electrode:

$$u|_{\partial\Omega} = V_l \ on \ E_l \ l = 1,2,3,...\text{L} \tag{3.9}$$

E_l denotes the area under the l^{th} electrode.

The driving current is described by the Neumann boundary condition, which states that the current density on the boundary are known:

$$\frac{\sigma \partial u}{\partial \vec{n}} = \begin{cases} J_l & on \ E_l \\ 0 \ \ on \ \partial\Omega \ / \bigcup_{l=1}^{L} E_l \end{cases} \tag{3.10}$$

where J_l denotes the current density on the l^{th} electrode and $\partial\Omega \ / \ \cup_{l=1}^{L} E_l$ indicates the boundary space acquired outside the electrodes area.

All EIT systems require electrodes on the boundary for driving and measuring purposes. The solution of the EIT forward problem requires reinforcing proper boundary conditions, which would require a reasonable and appropriate electrode model development to account for the eletrode interactions within the object. Four most commonly known electrode models, namely continuum model, gap model, shunt model, and complete electrode model, are considered. The continuum model is the simplest model used in ERT; it assumes that all of $\partial\Omega$ is accessible to input current and there is effectively an infinite number of electrodes. This assumption is obviously far from the reality. The gap model improves the continuum model by considering the gap between electrodes and the current density *J* is zero in the gap. It is, however, not comprehensive as it neglects the shunting effect of metal electrodes and could result in an overestimation of the resistivity. The shunt model further refines the electrode model by assuming a constant potential on electrodes. Therefore, the shunt boundary condition can be mathematically modelled as:

$$I_l = \int_{E_l} \frac{\boldsymbol{\sigma} \partial u}{\partial \vec{n}} \cdot d\Omega \tag{3.11}$$

$$V_l = u = constant$$

Given that the electrodes have to be in contact with the medium, a voltage drop across the contact impedance is introduced into the forward problem. Such contact-impedance effect is particularly vital in the absolute image reconstruction method. The complete electrode model is then developed upon the shunt model incorporating the contact impedance effect. The complete electrode model is the most sophisticated description of the electrode/body interactions that takes into account the contact impedance Z_l. The complete electrode model boundary conditions are shown below:

$$\begin{aligned} & \mathrm{u} + Z_l \frac{\boldsymbol{\sigma}\partial u}{\partial \vec{n}} = V_l \\ & \int_{E_l} \frac{\boldsymbol{\sigma}\partial u}{\partial \vec{n}} \cdot d\Omega = I_l \\ & \frac{\boldsymbol{\sigma}\partial u}{\partial \vec{n}} = 0 \text{ on } \partial\Omega \,/\, \cup_{l=1}^{L} E_l \end{aligned} \qquad \textbf{(3.12)}$$

3.1.1.3. Finite element method (FEM)

For accurate EIT reconstruction, the prerequisite is to have a forward model capable of predicting the voltages on electrodes for a given conductivity distribution [103]. This forward model must also be able to predict the electric fields in the interior given an assumed conductivity distribution. An analytical solution for the forward problem is only applicable in simple cases, such as circular geometries with homogenous conductivity distributions. However, in most practical situations, especially in medical applications, the geometries of objects are complex. Hence, numerical techniques were introduced to solve the EIT forward problem [104]. As we are interested in non-homogeneous conductivity distributions on the domain, the finite element method (FEM) is the natural choice. FEM is a mathematical tool to solve partial differential equations numerically. In comparison to other methods, such as the finited difference method (FDM), the complex geometries can be implemented relatively easily with FEM.

In general, FEM approximates the variations involved in a process defined by partial differential equations by an ensemble of much simpler variations defined over small, elemental volume elements. The response of each element is expressed in terms of a finite number of degrees of freedom characterized as the value of an unknown function at a set of nodal points. The voltages on the nodes, which are known as nodal voltages, are assumed as an interpolation function of the vertices. A collection of such elements is called a finite element mesh, and we suppose that there are K elements with N vertices. We will approximate the potential using this mesh by functions which are linear on each simplex, and continuous across the faces. Basis functions (also referred to as shape functions), defined over the support of each element, are used to interpolate the governing equations. The procedure to solve the partial differential equations involved in the EIT problem are discussed below.

Firstly, we divide the region into smaller regions that we call elements. In the case of a 2D problem, it is commonly discretized into triangular elements. Figure 3.1(a) presents an example of a 2D FEM mesh of a circular view region.

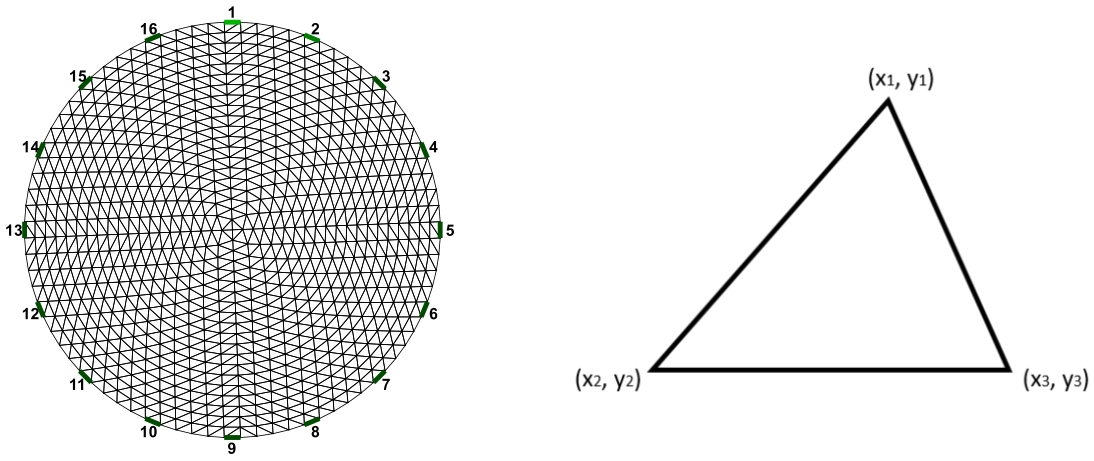

(a) (b)

Figure 3.1 (a) FEM mesh of a 2D circular region; (b) one triangle element from FEM mesh

Secondly, we need to select functions to describe the variation of the function inside each element. One of the usual choices is to take a polynomial $u(x, y) = a_0 + a_1 x + a_2 y$ (known as linear element). Then

the value of the trial function u for a given position x inside an element can be formulated by the values of u at the N nodes of the element ($[u_1, u_2, \dots, u_N]$).

We consider a triangle element taken from a 2D FEM mesh with vertices numbered as node 1 (x_1, y_1), node 2 (x_2, y_2), and node 3 (x_2, y_2). The nodal voltages are u_1, u_2, and u_3, respectively and can be written as:

$$\begin{aligned} u_1 &= a_0 + a_1 x_1 + a_2 y_1 \\ u_2 &= a_0 + a_1 x_2 + a_2 y_2 \\ u_3 &= a_0 + a_1 x_3 + a_2 y_3 \end{aligned} \quad \textbf{(3.13)}$$

One can use (3.13) to solve coefficients a_0, a_1, and a_2 by taking an inversion:

$$\begin{bmatrix} a_0 \\ a_1 \\ a_2 \end{bmatrix} = \begin{bmatrix} 1 & x_1 & y_1 \\ 1 & x_2 & y_2 \\ 1 & x_3 & y_3 \end{bmatrix}^{-1} \begin{bmatrix} u_1 \\ u_2 \\ u_3 \end{bmatrix} \quad \textbf{(3.14)}$$

And the trial function $u(x, y)$ becomes

$$u(x, y) = \sum_{i=1}^{3} u_i \, N_i \quad \textbf{(3.15)}$$

Where $N_i = [1 \quad x \quad y] \begin{bmatrix} 1 & x_1 & y_1 \\ 1 & x_2 & y_2 \\ 1 & x_3 & y_3 \end{bmatrix}^{-1}$ is known as the shape function or interpolation function associated with the node i.

Now we extend (3.15) to the the entire region and the potential is denoted as $u(x, y)_{FEM}$, which is discretized by K FEM elements:

$$u(x, y)_{FEM} = \sum_{j=1}^{K} \sum_{i=1}^{N} \mathrm{u}_{i,j}(x, y) \, N_{i,j} \quad \textbf{(3.16)}$$

Where j denotes the different element and i denotes the different nodes inside the j^{th} element. Here $N_{i,j}$ are zero when out of the element j.

Since the shape functions $N_{i,j}$ are not differentiable, we need to instead derive the weak solution for of the equation (3.8). We multiply (3.8) by a shape function A and integrate over the region **Ω**:

$$\int_{\Omega} A\nabla \cdot (\sigma \nabla \mathrm{u}_{FEM})\, d\Omega = 0 \text{ in } \Omega \tag{3.17}$$

Then applying Green's second identity and the vector derivative identity:

$$\nabla \cdot (A\sigma \nabla \mathrm{u}_{FEM}) = \sigma \nabla \mathrm{u}_{FEM} \cdot \nabla \mathrm{A} + \mathrm{A}\nabla \cdot (\sigma \nabla \mathrm{u}_{FEM}) \tag{3.18}$$

Therefore (3.17) becomes:

$$\int_{\Omega} \nabla \cdot (A\sigma \nabla \mathrm{u}_{FEM})\, d\Omega - \int_{\Omega} \sigma \nabla \mathrm{u}_{FEM} \cdot \nabla \mathrm{A}\, d\Omega = 0 \tag{3.19}$$

Invoking the divergence theorem:

$$\begin{aligned} \int_{\Omega} \nabla \cdot (A\sigma \nabla \mathrm{u}_{FEM})\, d\Omega &= \int_{\partial\Omega} A\sigma \nabla \mathrm{u}_{FEM} \cdot \boldsymbol{n}\, d\mathrm{S} \\ \int_{\Omega} \sigma \nabla \mathrm{u}_{FEM} \cdot \nabla \mathrm{A}\, d\Omega &= \int_{\partial\Omega} \sigma \nabla \mathrm{u}_{FEM} \cdot \boldsymbol{n}\, A dS \end{aligned} \tag{3.20}$$

The Dirichlet boundary condition in (3.12) can now be rearranged as:

$$\sigma \nabla \mathrm{u}_{FEM} \cdot \boldsymbol{n} = \frac{(V_l - \mathrm{u}_{FEM})}{Z_l} \tag{3.21}$$

On E_l and combining it into (3.20), we can get:

$$\int_{\Omega} \sigma \nabla \mathrm{u}_{FEM} \cdot \nabla \mathrm{A}\, d\Omega = \sum_{l=1}^{L} \int_{E_l} \frac{1}{Z_l} (V_l - \mathrm{u}_{FEM}) A dS \tag{3.22}$$

Here we assume $A = \sum_{j=1}^{N} \phi_j N_j$. The total current on electrodes can be written as integrals of current density over electrodes, and for the l^{th} electrode the current is:

$$I_l = \int_{E_l} \frac{1}{Z_l}(V_l - \mathrm{u}_{FEM})dS$$
$$= \frac{E_l}{Z_l}V_l - \frac{1}{Z_l}\sum_{i}^{N} N_i \int_{E_l} \phi_i \, dS \quad \textbf{(3.23)}$$

Now the FE system equations can be rearranged in the form:

$$\begin{bmatrix} \alpha & \beta \\ \beta' & \gamma \end{bmatrix} \begin{bmatrix} \mathrm{u} \\ V \end{bmatrix} = \begin{bmatrix} 0 \\ I \end{bmatrix} \quad \textbf{(3.24)}$$

Where,

$$\alpha_{i,j} = \int \sigma \cdot \nabla N_i \cdot \nabla N_j d\Omega + \int \frac{1}{Z_l}(N_i \cdot N_j)dS$$

$$\beta_{i,j} = -\int \frac{1}{Z_l}\Phi_j dS$$

$$\beta_{i,j}{}' = -\int N_j dS$$

$$\gamma = \begin{bmatrix} \frac{E_l}{Z_l} & \cdots & 0 \\ \vdots & \ddots & \vdots \\ 0 & \cdots & \frac{E_l}{Z_l} \end{bmatrix} \quad \textbf{(3.25)}$$

$$[\mathrm{u}] = \begin{bmatrix} \mathrm{u}_1 \\ \vdots \\ \mathrm{u}_N \end{bmatrix}$$

$$[\mathrm{V}] = \begin{bmatrix} \mathrm{V}_1 \\ \vdots \\ \mathrm{V}_L \end{bmatrix}$$

$$[\mathrm{I}] = \begin{bmatrix} \mathrm{I}_1 \\ \vdots \\ \mathrm{I}_L \end{bmatrix}$$

3.1.1.4.Jacobian matrix

Jacobian matrix, by definition, is the discrete Frechet derivative of a non-linear function which maps the perturbation of the solutions to perturbations on the boundary data. It is widely used in optimization-

based EIT reconstruction problems. The Jacobian matrix reflects the changes of output voltages with respect to the changes of conductivities in an EIT problem:

$$\Delta\sigma|_{\Omega} \mapsto \Delta V|_{\partial\Omega} \tag{3.26}$$

where $V(I^d) = [V(I_1^d)V(I_2^d) \dots V(I_k^d)]$ is the vector of the boundary measurements corresponding to k driving current patterns, then the Jacobian matrix can be defined as:

$$J = \begin{bmatrix} \frac{\partial V(I_1^d)}{\partial \sigma_1} & \cdots & \frac{\partial V(I_1^d)}{\partial \sigma_k} \\ \vdots & \ddots & \vdots \\ \frac{\partial V(I_k^d)}{\partial \sigma_1} & \cdots & \frac{\partial V(I_k^d)}{\partial \sigma_k} \end{bmatrix} \tag{3.27}$$

Jacobian can be practically solved by its definition (3.27) where each element is perturbed by a small amount $\Delta\sigma$ in turn and then calculate the perturbation ΔV on the boundary. However, this method can be extremely inefficient for large scale of finite element models. Instead, we calculate Jacobian as an integral of the scalar dot product of the gradients of current and measured fields. The Jacobian matrix can be calculated based on the discretization of the domain such that the conductivity is piecewise constant on polyhedral domains. For the k^{th} element Ω_k with a current pattern I^d injected into the volume, the associated measruement pattern potential $u(I^m)$ can be calculated. Then

$$J = \frac{\partial V^{(d.m)}}{\partial \sigma_k} = -\int_{\Omega_k} \nabla u(I^d) \cdot \nabla u(I^m)\, dV \quad \text{on pixel/voxel k} \tag{3.28}$$

where $V^{(d.m)}$ is the m^{th} measurement under the d^{th} current pattern. Each row of the Jacobian matrix describes the sensitivity distribution inside the volume with regards to a particular measruement and current pattern at the time.

3.1.2.Inverse problem

The inverse problem attempts to determine the conductivity distributions, x, from a finite number of boundary voltage measurements, y. It is an inverse of the following forward problem:

$$y = f(x) \tag{3.29}$$

And can be represented by:

$$x = f^{-1}(y) \tag{3.30}$$

According to Hadamard, a mathematical model of a physical model is well posed if:

1. For all admissible data, a solution exists;
2. For all admissible data, the solution is unique;
3. The solution depends continuously on the data.

However, due to the limitation of electrode size and placement restrictions, the number of independent measurements is always less than the number of image elements to be estimated, which is called the rank-deficient problem. This makes the unique solutions of such systems non-exist. Even worse, small changes in measurements could result in extremely large amount of changes in the model estimation, which fails the third condition. Hence, the EIT inverse problem is inherently an ill-posed problem. To overcome such situations, regularizations are introduced to impose additional information or constrain for stabilization.

The algorithms developed for EIT image reconstruction can be divided into two main categories, deterministic methods based on linearization and the non-linear inversion methods. The linearization of EIT problem is valid only under the condition that the conductivity changes are below $\pm$20% of the reference value[105]. That is the perturbation from the linearization point is small where the conductance varies not too much from the background. And the measurements can be approximated in a linear fashion with respect to the distribution changes. The linearized methods can be subdivided into the direct methods that obtains the solution in a single regularized step, e.g. Tikhonov regularization, and the iterative methods which approximates the initial estimates and the regularized inverse solution

at each iteration, such as Landweber iteration, conjugate gradient algorithm, and the Newton one-step error reconstruction (NOSER) [106]. On the other hand, the non-linear method seeks a full reconstruction of the conductivity distribution using the iterative approach that considers instrinsic nonlinearity[107]. The non-linear solutions methods are particularly useful when a reference data is not available for calibrating the forward model and therefore a linearized difference imaging method is not possible, i.e. normally absolute imaging method. The non-linear approach can also be divided into direct and iterative methods. The essence of iterative non-linear solutions methods is to repeat the process of calculating Jacobian and solving a regularized linear approximation, which can be computationally expensive especially when 3-D problems are considered. On the other hand, the direct methods, including layer stripping algorithm, scattering tranform[105]. Throughout this work, the goal is to reconstruct a change in conductivity between two states measured at either different times or frequencies, and these difference imaging problems are commonly solved by global linearization.

EIT reconstruction is the process of estimating conductivity from the boundary voltage measurements V_{meas}, which is also known as the inverse problem,

$$V_{meas} = F(\sigma) + \boldsymbol{e} \tag{3.31}$$

where $\boldsymbol{F}$ is a forward operator, which estimates the boundary voltages using linear approximation from calculated Jacobian, and $\boldsymbol{e}$ is the mismatch between measurements and the estimation from the forward model. To simplify (3.31) by using a linear approximation:

$$V_{meas} - F(\sigma_0) \approx J(\sigma - \sigma_0) \tag{3.32}$$

where J is the Jacobian or sensitivity matrix of $\boldsymbol{F}$ calculated at the initial conductivity estimate σ_0. Defining $\Delta\sigma = \sigma - \sigma_0$, and $\Delta V_{meas} = V_{meas} - F(\sigma_0)$, then (3.32) can be written as:

$$\Delta V_{meas} = J\Delta\sigma. \tag{3.33}$$

As described previously, the Jacobian matrix is singular, that is, the we have more unknowns than data. Then if only consider the excess of data, the natural solution to (3.33) would be to use the Moore-Penrose generalized inverse (also called the pseudo-inverse):

$$\Delta\sigma_{MP} = J^{\dagger}\Delta V_{meas} = (J^{*}J)^{-1}J^{*}\Delta V_{meas} \quad \textbf{(3.34)}$$

Where $J^{\dagger}$ is the Moore-Penrose inverse, J^{*} denotes Hermitian transpose (also called conjegate transpose). Such pseudo-inverse computes the best fit solution to:

$$\Delta\hat{\sigma} = argmin(\|\Delta V_{meas} - J\Delta\sigma\|). \quad \textbf{(3.35)}$$

And this lacks a unique solution.

3.1.2.1.Singular value decomposition

The singular value decomposition (SVD) is the generalization to non-square matrices of orthogonal diagonalization of Hermittian matrices. The decay of singular values suggests the extent of the instability of inverse problems and thus it is a very useful tool for understanding the ill-conditioning of matrices. With a rectangular matrix $A \in \Re^{m\times n}$ with m≥n, then the SVD of A is a decomposition of the form:

$$A = \mathbb{U}\Sigma V^{T} = \sum_{i=1}^{n} u_i \sigma_i {v_i}^{T} \quad \textbf{(3.36)}$$

Where $\mathbb{U} = (u_1, u_2, \dots, u_n)$ and $V = (v_1, v_2, \dots, v_n)$ are matrices with orthonormal columns called singular vectors, $\mathbb{U}^{T}\mathbb{U} = V^{T}V = I_n$. And the diagonals of Σ includes the singular values which are positive singular values $(\sigma_1, \sigma_2, \dots, \sigma_n)$ sorted in a non-increasing order. As the elements of diagonal matrix Σ are uniquely determined by the matrix being decomposed, the plot of singular values can be considered as a valuable tool in studying the ill-conditioning of a problem. The idea of how ill-conditioned the Jacobian is can be evaluated by its condition number, which is defined as the ratio of its largest singular value to its smallest one. The smaller the condition number is, the more well-conditioned it is.

A logarithmic plot of the singular values of a Jacobian matrix is presented in Figure 3.2. The calculations are based on a 2D circular EIT model with homogeneous conductivity distribution 1 and 16 electrode injecting currents in adjacent pair drive patterns, which made up a total of 208 measurements in one

frame. As expected from the ill-posedness nature of inverse problem, there is a remarkable gap between the large and small singular values, which indicates a rank deficiency. This also explains that among 208 measurements, only 104 of them are independent and the rest, which are linearly dependent, cannot be used to solve the inverse problem.

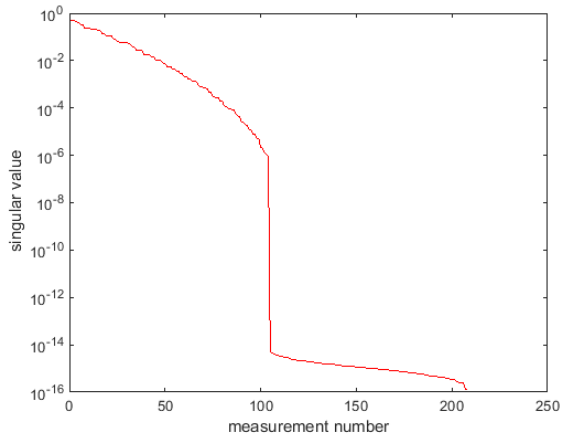

Figure 3.2 Singular value plot of a 16 electrode EIT system measurements

We can use the singular spectrum $\mathbb{U}^* V_{meas}$ of a set of measurements V_{meas} to determine how useful that set of measurements will be at a given error level.

3.1.2.2.Tikhonov reconstruction

The conventional L^2- norm method of solving (3.33) is seeking to minimize the residual:

$$\Delta\hat{\sigma} = argmin(\|\Delta V_{meas} - J\Delta\sigma\|_2^2). \quad \textbf{(3.37)}$$

Tikhonov algorithm is the most popular direct regularization method. Tikhonov regularization imposes additional information, which is known as a prior, and hence the least square minimization problem incorporating regularization term can be formulated as below:

$$\Delta\sigma = argmin(\|\Delta V_{meas} - J\Delta\sigma\|_2^2 + \alpha L\|\Delta\sigma\|_2^2) \quad \textbf{(3.38)}$$

where α is the regularization parameter controlling trade-off between regularization and fidelity; and L is the regularization functional. As α gets smaller, $\Delta\sigma$ tends to approach a generalized solution (3.34).

Let the first-order derivative of the Tikhonov function with repect to $\Delta\sigma$ equal to zero, and the solution becomes:

$$\Delta\sigma = (J^T J + \alpha L)^{-1} J^T \Delta V_{meas} \quad \textbf{(3.39)}$$

3.1.2.3. Total variation regularization

The total variation problem is defined by replacing the penalty term L1 norm of the gradient of the image:

$$R(\Delta\sigma) = \|\nabla\Delta\sigma\|_1 \quad \textbf{(3.40)}$$

where $\|\cdot\|_1$denotes the L1 norm, and ∇ is the gradient.

The unconstrained formulation for the linearized model of EIT problem as following:

$$\Delta\sigma = argmin\left(\frac{1}{2}\|J\Delta\sigma - \Delta V_{meas}\|_2^2 + \alpha\|\nabla\Delta\sigma\|_1\right). \quad \textbf{(3.41)}$$

The introduction of the TV method, however, makes the inverse problem non-differentiable, so the traditional gradient class inversion algorithms are not applicable.

In this work, minimization of functions of TV norms is solved by the Bregman iteration technique, i.e. error forgetting [108], which benefits the advantages of quick convergence and a constant regularization parameter. The split Bregman algorithm, that combines the Bregman distance with splitting technique, was proposed in [98]. It was proved a good performance when applied to EIT with higher resolution, better noise resistivity and faster convergence compared with other TV algorithms[109], such as linearized alternating direction method of multipliers (LADMM)[110]. This makes SBTV algorithm a good candidate especially in medical applications.

The implementation of the split Bregman method can be accomplished by introducing auxiliary variables to separate the non-differentiable L^1-norm penalty term and L^2-norm functional so that they can be solved in two alternating steps. Then (3.41)(3.55) becomes a constrained optimization problem:

$$\Delta\sigma = argmin(\tfrac{1}{2}\|J\Delta\sigma - \Delta V_{meas}\|_2^2 + \alpha\|d\|_1) \text{ s.t. } d = \nabla\Delta\sigma \quad \textbf{(3.42)}$$

where d is an auxiliary variable.

The corresponding unconstrained solution of by applying the Lagrange equation is

$$\Delta\sigma = argmin\frac{1}{2}\|J\Delta\sigma - \Delta V_{meas}\|_2^2 + \alpha\|d\|_1 + \frac{\beta}{2}\|d - \nabla\Delta\sigma\|_2^2 \quad \textbf{(3.43)}$$

where β is the split parameter.

Applying the Bregman iteration method, the original problem can be transformed into the following sub-problems:

$$(\Delta\sigma^{k+1}, d^{k+1}) = argmin\frac{1}{2}\|J\Delta\sigma - \Delta V_{meas}^k\|_2^2 + \alpha\|d\|_1 + \frac{\beta}{2}\left\|d - \nabla\Delta\sigma - b_d^k\right\|_2^2 \quad \textbf{(3.44)}$$

$$b_d^{k+1} = b_d^k + \nabla\Delta\sigma^{k+1} - d^{k+1}. \quad \textbf{(3.45)}$$

The minimization of can be handled by separately solving the minimization of $\Delta\sigma$ and d as below:

$$\Delta\sigma^{k+1} = argmin_{\Delta\sigma}\left(\frac{1}{2}\left\|J\Delta\sigma - \Delta V_{meas}^k\right\|_2^2 + \frac{\beta}{2}\left\|d - \nabla\Delta\sigma - b_d^k\right\|_2^2\right)$$

$$d^{k+1} = argmin_d\left(\alpha\|d\|_1 + \frac{\beta}{2}\left\|d - \nabla\Delta\sigma^{k+1} - b_d^k\right\|_2^2\right).$$

This was computed as the following procedure and initially assign value to $\Delta\sigma^0 = 0$, and then set $d^0 = b_d^0 = 0$:

Step 1: $B\Delta\sigma^{k+1} = \beta\left(d^k - b_d^k\right) + J^T\Delta V_{meas}^k$,

where $B = J^TJ + \beta I$

Step 2: $d^{k+1} = shrink(\Delta\sigma^{k+1} + b_d^k, {}^{\alpha}/_{\beta})$

Step 3: $b_d^{k+1} = b_d^k + \Delta\sigma^{k+1} - d^{k+1}$

Step 4: $\Delta V_{meas}^{k+1} = \Delta V_{meas}^k - J\Delta\sigma^{k+1}$

In addition to the Total Variation regularization discussed above, a Besov regularizer was proposed and evaluated to produce a superior image reconstruction [98], that is, the regularization term becomes $\|u\|_{BV} + \|u\|_{B1,1}$. The inclusion of multiple regularizers helps to reconstruct smooth images with little effect on the convergence time.

3.1.2.4. Temporal one-step solver

A dynamic Tikhonov based method can be used in the applications where conductivity changes are very fast with respect to the EIT frame rate [111]. Attempts to enhance the temporal resolution of images in the situation where the resistivity distribution inside the object changes rapidly in time have been undertaken. [112]proposed the first Kalman filter based method that is formulated as a state-space estimating problem to track fast impedance changes. [113]further combined the Kalman filter and Kalman smoother approaches and evaluated the method with real phantom measurements. [114]estimates the resistivity distribution after the voltage measurements corresponding to each curent pattern with the aid of the extended Kalman filter (EKF). EKF outperformances the lineraized Kalman filter in the cases where the state changes greatly from the assumed linearized state, however, at the expense of increase computational burden. In addition, another dynamic EIT image reconstruction algorithm, Temporal one-step solver (TOS), which is based on one-step linear Gauss-Newton method, was proposed in [111]. It improves Kalman filter based algorithms by introducing regularization prior and the weighting of the measured data; hence it is advantageous for cases in which the data is noisy and the conductivity changes are rapid with respect to the frame rate. It is formulated in the way that one sequence of data is treated as one single inverse problem with a regularization prior which accounts for both spatial and temporal correlations between image elements. Specifically, the data frame sequence is concatenated as $\widetilde{\Delta u_t} = [\Delta u_{t-d}; \dots; \Delta u_t; \dots; \Delta u_{t+d}]$ and the resulting concatenated images $\widetilde{\Delta\sigma_t} = [\Delta\sigma_{t-d}; \dots; \Delta\sigma_t; \dots; \Delta\sigma_{t+d}]$. The forward problem can then be modified to:

$$\widetilde{\Delta \boldsymbol{u}_t} = \tilde{\boldsymbol{J}}\widetilde{\Delta \boldsymbol{\sigma}_t} + \boldsymbol{noise} \tag{3.46}$$

Which can be augmented as:

$$\begin{bmatrix} \Delta \boldsymbol{u}_{t-d} \\ \vdots \\ \Delta \boldsymbol{u}_t \\ \vdots \\ \Delta \boldsymbol{u}_{t+d} \end{bmatrix} = \begin{bmatrix} \boldsymbol{J} & \cdots & \boldsymbol{0} \\ \vdots & \ddots & \vdots \\ \boldsymbol{0} & \cdots & \boldsymbol{J} \end{bmatrix} \begin{bmatrix} \Delta \boldsymbol{\sigma}_{t-d} \\ \vdots \\ \Delta \boldsymbol{\sigma}_t \\ \vdots \\ \Delta \boldsymbol{\sigma}_{t+d} \end{bmatrix} + \begin{bmatrix} \boldsymbol{n}_{t-d} \\ \vdots \\ \boldsymbol{n}_t \\ \vdots \\ \boldsymbol{n}_{t+d} \end{bmatrix} \tag{3.47}$$

Here J is assumed to be constant and $\tilde{J} = I \otimes J$, where the identity matrix has the size of 2d+1, and $\otimes$ is the Kronecker product. The temporal inverse problem can be rewritten as

$$\left\| \widetilde{\Delta \boldsymbol{u}_t} - \boldsymbol{J}\widetilde{\Delta \boldsymbol{\sigma}_t} \right\|^2 + \boldsymbol{\lambda}^2 \left\| \widetilde{\Delta \boldsymbol{\sigma}_t} \right\|^2 \tag{3.48}$$

Applying GN one-step solver, (3.48) can be solved as

$$\widetilde{\Delta \boldsymbol{\sigma}_t} = (\boldsymbol{J}^T \boldsymbol{W} \boldsymbol{J} + \boldsymbol{\alpha}^2 \mathbf{R})^{-1} \boldsymbol{J}^T \boldsymbol{W} \widetilde{\Delta \boldsymbol{u}_t} \tag{3.49}$$

where W models the measurement accuracy, and for difference EIT with identical channels $W = I$. The regularization matrix R here is set to a combination of multiple prior matrices as opposed to the traditional identity matrix:

$$\boldsymbol{R} = \boldsymbol{a}_1 \boldsymbol{diag}\left(\boldsymbol{J}^T \boldsymbol{J}\right) + \boldsymbol{a}_2 \boldsymbol{eye}\left(\boldsymbol{size}(\boldsymbol{J}, \mathbf{1})\right) + \boldsymbol{a}_3 \boldsymbol{R}_3 \tag{3.50}$$

In which $\mathrm{diag}(J^T J)$ contributes to a NOSER prior, $eye\left(size(J, 1)\right)$ denotes zeroth-order Tikhonov regularization matrix, and R_3 is another type of regularization matrix that represents the discrete Laplacian filter. Such addition of multiple priors benefits the system with an enhanced reconstruction; thus a better immunity to noises.

3.2. Image quality measures

Given an EIT measurement system, the overal system performance can be affected by many factors, such as the reliability of the data, noise level, and the selected image reconstruction algorithms. This is due to the complexity of an ERT system, which involves body interface (i.e. cables and electrodes),

electronic stimulation and measurement hardware, and image reconstruction software. Several system evaluation criterion have been prevously proposed [115-117]. We adopted parameters proposed in [118] to quantitatively analyze the image quality throughout this work especially in the cases where the true situations are available for comparison.

An impage can be discretized into N pixels and can be represented by a column vector $\hat{x}$. A threshold of one-fourth of the maximum amplitude is applied, which detects most of the visually significant effects:

$$[\hat{x}_q]_i = \begin{cases} 1, & [\hat{x}_q]_i \geq \frac{1}{4}\max(\hat{x}) \\ 0, & otherwise \end{cases}. \quad \textbf{(3.51)}$$

We adopt this threshold to binarize images so that simplicity can be achieved in further computing the evaluation parameters.

1. Position Error (PE)

Position error describes the mismatch between the real position P_0 and the position of the reconstructed object P_q. The numerical location can be represented by the center of gravity (CoG) of the target and PE can then be defined as:

$$PE = |P_0 - P_q|. \quad \textbf{(3.52)}$$

Evidently, the significance of PE indicates the unreliable interpretation of reconstructed images. Hence, PE is preferred to be small and uniform aross the whole region.

2. Amplitude Response (AR)

Amplitude response measures the ratio of the image pixel amplitude in the target to that in the reconstructed image:

$$\mathrm{AR} = \sum_{\mathrm{k}} [\hat{\mathbf{x}}]_{\mathrm{k}} / V_T \tag{3.53}$$

where V_T is an original target volume. AR describes how targets at different locations contribute to the overall image amplitude. It should ideally be uniform over the region of interest

3. Shape Deformation (SD)

In the simplified cases where anomalies used in the tests are in circular form, shape deformation is defined the fraction of the reconstructed one-fourth amplitude that fails to fit within a circle of the area equivalent to the real image:

$$\mathrm{SD} = \sum_{\mathrm{k}\notin\mathrm{C}} \left[\hat{\mathbf{x}}_{\mathrm{q}}\right]_{\mathrm{k}} \Big/ \sum_{\mathrm{k}} \left[\hat{\mathbf{x}}_{\mathrm{q}}\right]_{\mathrm{k}} \tag{3.54}$$

where C is a circle centered at $\mathrm{P_q}$ with an area equal to $\mathrm{A_q}$. SD should also be low and uniform as large SD may result in incorrect interpretation of inclusions.

4. Resolution (RES)

Resolution measures the size of reconstructed inclusion as a fraction of size of entire imaging region. In this work, it is defined as the area ratio of the recognizable anomaly to the entire sensing area instead of the diameter ratio:

$$RES = \sqrt{A_q / A_0} \tag{3.55}$$

where $A_q = \sum_k \left[\hat{x}_q\right]_k$ is the number of pixels in $\hat{x}_q$ and A_0 is the number of pixels over the entire medium region. RES should be uniform, in order to accurately represent the shape of the target conductivity distribution.

5. Correlation Coefficient (CC)

Correlation coefficient compares the similarity of the reconstructed images to the real distribution. For two grayscale images $\hat{x}_q$, $\hat{x}_0$, the correlation is defined by:

$$CC_{\hat{x}_q,\hat{x}_0} = \frac{cov(\hat{x}_q, \hat{x}_0)}{\sigma_{\hat{x}_q}\sigma_{\hat{x}_0}} \quad \textbf{(3.56)}$$

where cov is covariance, and σ_X, σ_Y are standards deviations of the pixel values. The closer CC is to 1, the more similar the reconstructed image $\hat{x}_q$ is to the real images $\hat{x}_0$.

6. Relative Error (RE)

Relative error, which quantifies the difference between the reconstructed image and the real image with respect to the real image, can be defined as:

$$RE = \frac{\|x_0 - \hat{x}_q\|_2}{\|x_0\|_2} \quad \textbf{(3.57)}$$

where x_0 is the pixel vector of the real image. As the definition suggests, the smaller RE is, the higher quality of the reconstructed image it is.

Chapter 4 ERT hardware development

In the previous chapters, we have shown how ERT could be a good fit for measuring wastewater flows. Addtionally, the exsiting technologies for building ERT/EIT systems and their performances have been reviewed. This chapter presents the electronics hardware design and bespoke signal processing to create an embedded ERT sensor for measuring sewer flows. The ERT device is aimed towards industrial real-time data acquisition applications at low cost. Therefore, the dedicated analogue signal conditioning module, zero-cross switching scheme, together with single source excitation enable the system to perform cost effective serial measurements whilst still provide reliable real-time capturing. The system performance was evaluated via both stationary and dynamic lab-scale experiments. This chapter is widely based on the journal article 'Smart Water Meter Using Electrical Resistance Tomography'.

4.1. Introduction

In the UK, the underground sewer system, with a total length of 347,000 km, carries over 11 billion liters of wastewater every day [119]. The operational conditions of sewer systems can change over time due to blockages caused by sediment and fats in the untreated wastewater, and structural changes associated with ageing; hence, it is vital to gather sufficient information on the current condition of a sewer system to proactively prevent the service failures. Currently, conventional non-tomographic technologies that are only capable of providing flowrate measurements, such as ultrasonic Doppler velocity profilers, electromagnetic meters, Coriolis mass meters, and Venturi meters, are commercially available. However, the wastewater flow behaviour comprises more than one phase due to the complexity of its compositions, which cannot be differentiated by traditional flow meters. Process tomographic scanners, as a result, can be good alternatives by providing real-time cross-sectional images on the phase distribution.

Process tomography provides measurements of concentration distribution and flow profile within a process instrument by collecting data via remote sensors. Electrical tomography is one of the most

extensive tomographic modalities that can provide cross-sectional profiles of the distribution of materials or velocities in a process vessel or supply information about transient phenomena in the process. The advantages of such technology, such as high temporal resolution, low cost, no radiation hazard and non-intrusive/non-invasive, have made electrical tomography a promising technology in monitoring and analyzing various industrial flows [120]. Electrical tomography can be further divided into Electrical Capacitance Tomography (ECT) and Electrical Impedance Tomography (EIT), based upon the dielectric properties of the continuous phase in the domain. EIT measurements provide information on the real and imaginary parts of the impedance, as well as the phase angle. However, in the process industries, applications commonly rely on the conductivity difference between two phases to obtain the concentration profiles. Therefore, Electrical Resistance Tomography (ERT) are dominantly employed in imaging conductive flow measurements [121]. Various ERT hardware systems have been developed as research tools for process engineering studies [7, 67, 71, 72, 95, 96].

As mentioned previously the minimum rated operating conditions for fluid conductivity shall be 50 μS cm^{-1} to 1200 μS cm^{-1} [64]; this makes ERT a good candidate for playing an important role in monitoring wastewater flow. One of the major concerns in sewers is blockages caused by built-up grease, sanitary products, food scraps, etc. ERT can distinguish between different concentrations by their conductivities; further identification of transitions between homogeneous and heterogeneous flow regime can be implemented by direct/indirect interpretation of measurements. Since obstacles in pipeline systems can disturb the dynamic flow behavior [122], blockages can change the flow within the sensing area. Therefore, by properly characterizing wastewater flow regimes, early detection of sewer blockages can be achieved.

In this chapter, we will firstly review the operation principle of existing ERT hardware system and establish an understanding of the procedure to design one ERT data acquisition system. Subsequently an ERT DAS device will be developed, dedicated to wastewater applications. A top-down view of the proposed design will be presented and explained, and each module included in the design will be described in detail. Lab-scaled stationary experiments were conducted to verify the accuracy of the measurements. Image reconstructions, including a quantitative image quality analysis, as well as

numerical analysis, namely Signal to Noise Ratio (SNR) and cross-correlation, will be presented to evaluate the system performances.

4.2. System Overview

An overview of a 16-channel ERT hardware system is presented in Figure 4.1. The system incorporates: (1) A sensor array equally spaced around the domain periphery; (2) An effective data acquisition system (DAQ) device; (3) A personal computer that interacts with the DAQ, exacting and processing information.

The proposed DAQ system is a 16-channel serial ERT device, as shown in Figure 4.2, operating at 50 kHz using the adjacent driving and measuring protocol. It features the user configurable current injection at 50 kHz over the range of 6 mA to 18 mA, as well as the load-adaptive capability. The DAQ system is designed in a modular manner, and may be broken down into four modules:

- *An excitation source;*
- *An electrode switching module;*
- *A reception module;*
- *A central control unit functioned by an STM32 microcontroller*

These four modules are prototyped on three separate boards, i.e., excitation and reception board (top layer), switching board (middle layer) and microcontroller board (bottom layer). The advantages of this architecture are easy assembly, high mobility, and compactness.

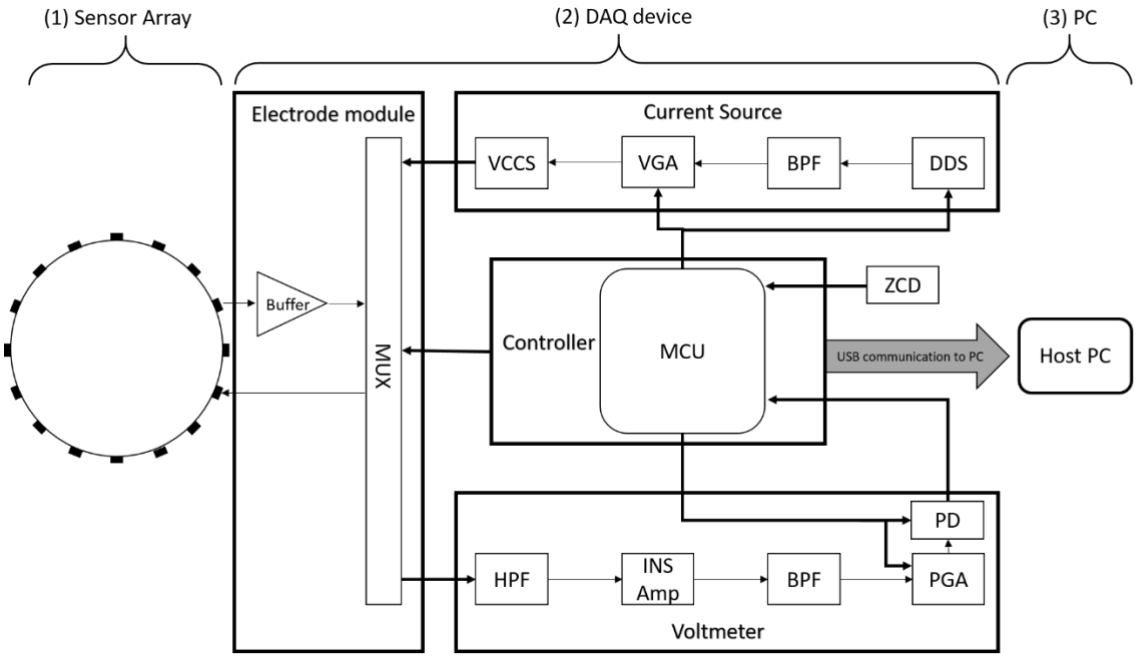

Figure 4.1 System overview

Figure 4.2 16 channel ERT device

4.3.Design and Methods

4.3.1. Excitation Source

Current, as opposed to voltage, is chosen as an excitation signal to the periphery of the conducting medium on the premise that a current source has a high output impedance, so that the effects of electrode contact impedance will be negligible. The current source presented in this chapter is composed of a signal generator, a band-pass filter, a variable gain amplifier and a voltage controlled current converter.

Two vital design specifications of the current source that could largely affect one ERT system performance are the operation frequency and the current strength. Large current injection in industrial

applications, without the limitation from safety considerations, is generally preferable to enhance the measurement sensitivity especially in the case when continueous phase is highly conductive. On the other hand, when the continuous phase is not very conductive, i.e. distilled water, large current injection can increase the stress on voltage compliance and thermal behaviour of electronics. Considering the conductivity of sewer flows, the current range is specified as 5mA and 15mA. The excitation frequency, which is one of the most importatnt factors in determining data acquisition speed, is also desired to be large. Therefore, a high specification of current source, especially with high output impedance, the large commonmode voltage rejection ratio, and large current at high frequencies can remarkably increase system reliablity as well as measurement sensitivity. However, this is very challenging due to the limitation from electronics and can increase the system complexity and hence the cost. It has been acknowledged that the operating frequencies of an ERT system should be kept relatively low within the range of 10kHz to 200kHz. This is particular important in large scale deployment where the gross parasitic capacitance associated with the sensor arrays can be significant under high frequencies. Current sources with single frequency output have been commonly limited to under 100kHz in many process EIT systems. we can simplify the design by generating single sinusoidal current of 50kHz.

Excitation signals in alternative waveforms have great advantages in reducing the effect of electrode polarization and isolating the direct current offset potential. Sinusoidal waveforms further provide access to full electrical impedance demodulation, and hence, the capability of spectroscopic measurements. Low-cost monolithic devices which can generate accurate waveforms via direct digital synthesis have recently become commercially available. DDS has been recognized as an attractive alternative to analogue Phase-Locked Loops (PLLs) for generating highly accurate, frequency-agile, and low distortion waveforms. A DDS can benefit the system with its fine resolutions at low frequencies (up to 200 kHz), inherent stability, and compactness. Hence, in the reported design, a Direct Digital Synthesizer (DDS) AD9837, is selected to produce a sinusoidal signal. The frequency of signal is programmed by the central control unit via SPI interface and an external 5MHz reference clock has been chosen as the dynamic performances are seen no differences compared to the other 16MHz option. However, an unfiltered DDS output signal has a 0.3V DC offset and rich in spurious content introduced

by a Digital to Analogue Converter (DAC). Thus, a fast settling Sixth-order Butterworth Bessel band-pass filter with a passband of 20 kHz centred at 50 kHz follows the DDS.

A variable gain amplifier (VGA) is used to allow for a flexible current excitation within the range of 6 mA to 18 mA. The VGA is essentially a non-inverting amplifier incorporating with a programmable digital potentiometer (DigiPot) and fixed value resistors. The value of DigiPot determines the gain of the VGA and is set via user commands at the beginning of collections referring to a look-up table.

One of the difficulties in designing an ERT system for process applications is the wide range of conductivities, varying from several μS cm^{-1} to a few hundred mS cm^{-1}. Hence, a current source that is able to provide a constant current supplying over a wide range of load impedances is a necessity. A dual op-amp voltage controlled current source developed by [123], which is capable of preserving high output impedance over a wide range of operating frequencies, is built around commercially available current feedback amplifiers in our system. The output current is a result of input voltage, V_{in} and the sensing resistor R_{sense}, following the equation:

$$I_{out}=V_{in}/R_{sense} \quad \textbf{(4.1)}$$

As mentioned previously, one of the most important capabilities of a current source is generating constant currents regardless the load. We connect the proposed current source to various loads, i.e. resistors of different values, and measure the current flow through it. Figure 4.3 presents two currents, which were intended to be 6.8mA and 11mA, inject into a resistor varying from 50ohm to 2400ohm. As can be observed from the test results, the current source is able to generate constant currents over the range of loading required by the sewer systems. Higher currents, however, did struggle to preserve the consistency more than the small currents. This is because the stray capacitance effect that has yet been compensated by an external circuitry can be more significant under a larger current operation.

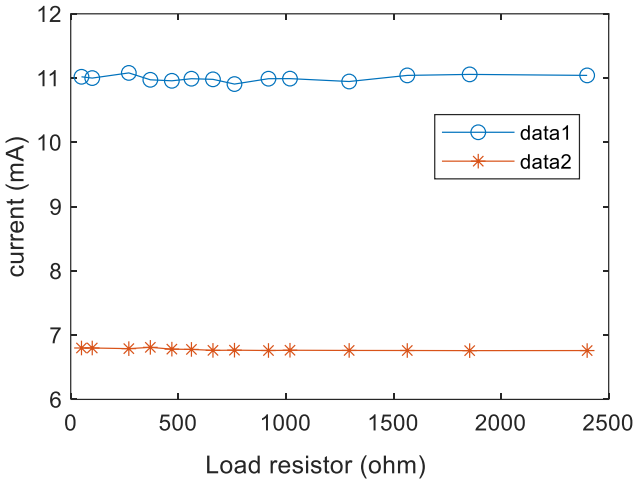

Figure 4.3 Current source tests

4.3.2.Electrode Switching Module

In this system, a serial collection protocol is employed; furthermore, it is critical to have a fast switching mechanism to achieve an overall data acquisition speed. Due to the non-idealities of multiplexers, including the non-zero on-resistance, charge injection, various settling time and retained charge, an appropriately designed switching circuit is essential to not only fulfil fast signal transients but also give the least chance of distorting receiving signals.

A multiplexer with the lowest possible on-resistance is desirable to maintain good linearity. However, the low on-resistance also means a large charge injection, which will result in a voltage glitch occurring at the multiplexer input when switching channels. To compensate for this, the source impedance of a multiplexer should be kept as low as possible. Therefore, a buffer amplifier with a high input impedance and an extremely low output impedance should be placed at each multiplexer input to settle a full-scale step.

A total of four 16:1 multiplexers are exploited, of which two are for the selection source and sink ports and the remaining two for selecting differential voltage ports. Four quadruple low-cost precision Junction gate Field-Effect Transistor (JFET) input operational amplifiers are introduced for buffering the received signal from the electrodes.

4.3.3. Reception Module

4.3.3.1. Signal Conditioning

Common-mode errors have been considered as being among the most significant sources of measurement errors. As described previously, the proposed design uses a single-end current source topology, the impedance between the grounded side of the current source and the amplifiers in the reception module is the main factor that introduces common-mode signal [124]. To eliminate common-mode errors, two techniques are implemented: (1) an instrumentation (INS) amplifier with a high common-mode rejection ratio (CMRR) at the desired frequency (i.e., 50 kHz) is selected to determine the differential voltage between two voltage signals; (2) fast high pass filters at the inputs of the instrumentation amplifier are used to remove the Direct Current (DC) component of the incoming voltage signals without compromising the acquisition speed.

An Eighth-order Butterworth bandpass filter (BPF) follows the INS amplifier to filter out any distortion that is introduced by the INS amplifier. The BPF is centered at 50 kHz with a 40 kHz passband (−3 dB) and 200 kHz stopband (−40 dB), which results in an approx. 100 μs step response time.

The voltage responses to the current injection can vary over a wide dynamic range from a few millivolts to several volts, depending on the size of the vessel as well as the medium/inclusion in the vessel. To accommodate for diverse applications of the system, another VGA of the same topology as the one employed in the excitation source is incorporated after the BPF, so that the measurements can fall within the acceptable range of the Analog to Digital Converter. This is achieved by a calibration process which happens both at the startup of the system operation and along the whole acquisition process, so that the system can adapt to any unpredictable changes.

4.3.3.2. Peak Detection

In an ERT system, only the in-phase component is required for reconstructing the conductivity distribution. An analogue precision peak detection circuit is implemented to obtain the amplitude of the differential voltage, as displayed in Figure 4.4. The maximum value of the incoming signal is captured

by charging up a capacitor, C_1. Specifically, when the input signal is rising, C_1 is charged to a new peak level; whereas D_1 and D_2 prevent C_1 to be discharged when the signal is falling. It is also vital to have a reset switch, Q_1, coupling the capacitor, which is performed by an N-channel enhanced Metal Oxide Semiconductor Field-Effect Transistor, so that the capacitor can be discharged and ready for the next series of signals. The active-high reset signal comes from the microcontroller and will be further discussed in 4.3.4

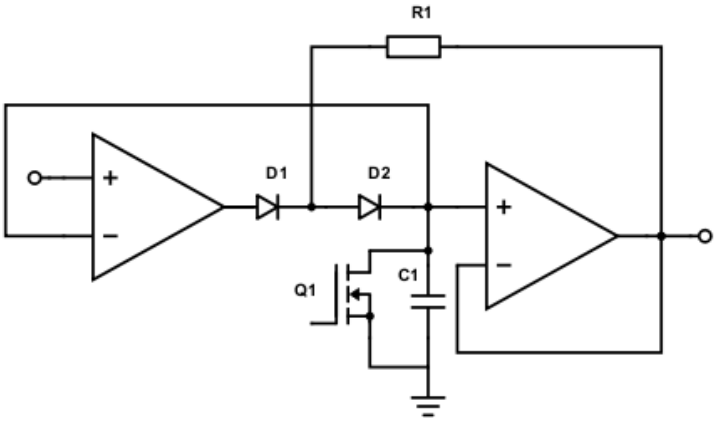

Figure 4.4 Peak detection circuit

The proposed peak detection technique is capable of generating high precision measurements with a high signal to noise ratio. The simplicity, and hence, the cost efficiency of the system, are achieved by replacing the complex phase shift demodulation technique with such peak detection circuit when compared with the conventional ERT device. In Figure 4.5, the error percentage between the input voltage and the output voltage captured by the peak detection circuit is plotted. As can be observed, the overall error is within 2.5% and is fairly consistent over the range from 200mV to 3000mV, which gives a chance of calibration for the output of the peak detection circuit over the entire measurement range.

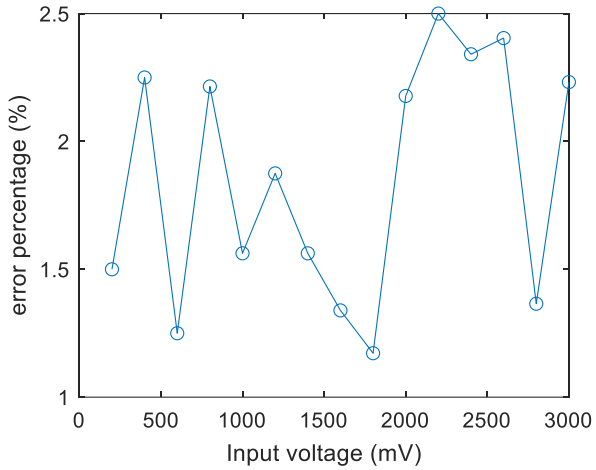

Figure 4.5 Error percentage plot of peak detection circuit

4.3.3.3. Analogue to Digital Converter (ADC)

The general dynamic range of collected signals is from 1:10 to 1:40 [125]; hence, with a minimum 1% accuracy, a 12-bit analogue to digital conversion is necessary. The built-in 12-bit ADC is used to continuously read voltage measurements using Direct Memory Access (DMA) mechanism, which allows for an automatic data transfer from ADC to memory without the usage of the Central Processing Unit (CPU). A total of 35 ADC readings are taken and 5 extrema are eliminated so that each voltage measurement is a result of an average over 30 ADC readings. The averaging technique benefits the system with a better signal to noise ratio by the factor of $\sqrt{N}$ (N is the number of times of averaging).

4.3.4. Central Control Unit

An STM32F4 microcontroller handles the commands to programmable integrated circuits (ICs), data exchange between a host PC and the device, and data processing. The sequence of operation follows the flowchart in Figure 4.6(a) below. After the system initialization, based on the choice of injection current level from the user command, a VGA gain on the injection side (VGA_i) is set for current. At the same time, an initial gain is also set for the reception side VGA (VGA_r), which is normally the smallest value in the look-up table. A calibration process is then performed after a whole frame of data is collected and a corresponding gain for VGA_r is calculated. Following that, a startup operation that allows for 5 frames (each frame contains 208 switches) of switching is carried out before the data

transmission happens. This startup operation enables the system to settle; hence, a better quality of data will be obtained in the later collection procedure. The authentic measurements then start on the command received at the end of the startup stage. A re-calibration check takes place each time a whole frame of readings is fed into the ADC. If any readings in this frame have reached 4095, then the calibration process will happen again to set a new VGA_r gain accordingly.

The sequence of one measurement follows that shown in Figure 4.6(b). The timing is essentially governed by a series of pulses of the stimulation frequency, i.e., 50 kHz, which is generated by the zero crossing detection of the input signal. The multiplexer switches at every 17 cycles of pulses and leaves the system operating at 14 fps. The peak detection reset signal occurs after 9 cycles from the switching instance to give signals sufficient settling time. Subsequently, the ADC conversion happens at cycle 11; the reading and averaging of measurements finishes in 4 cycles.

Communication between the host PC and the ERT device is accomplished via Universal Serial Bus (USB) micro-AB at full speed (12 Mbps). On the host terminal, data could be received and stored either by REALTERM terminal emulator software or MATLAB. It's worth noting that only after a whole frame of 208 measurements all taken, this one frame of data is transmitted to the host PC at once, as indicated in Figure 4.6(c).

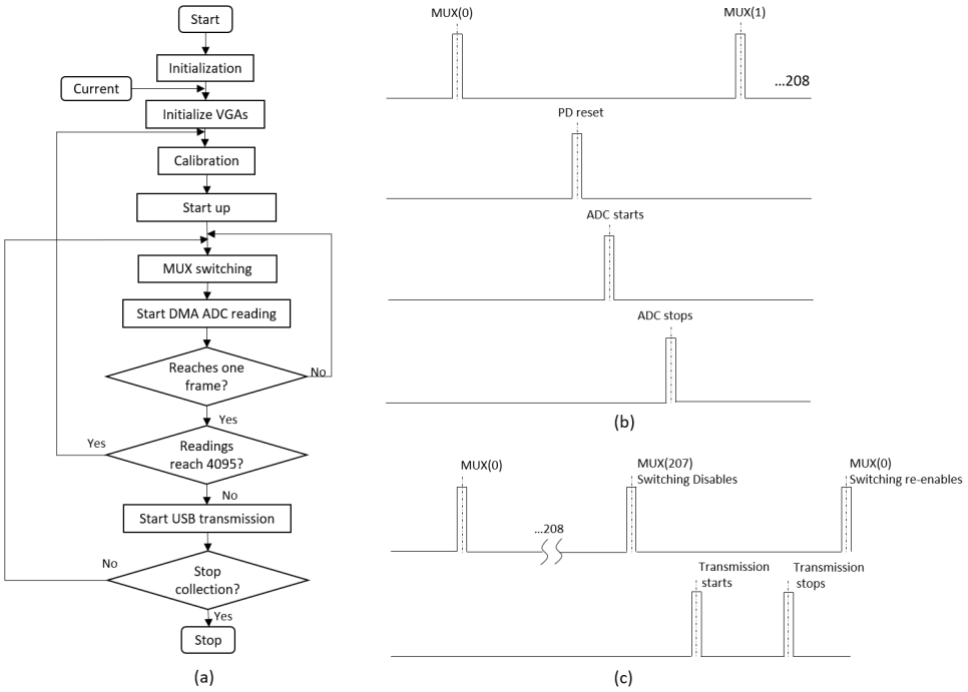

Figure 4.6 (a) Operation procedure of the microcontroller command (b) Timing simulation between two switching instances (c) Timing simulation between two frames of collection.

4.4. Device performance

4.4.1. Signal to Noise Ratio (SNR)

To help understand the quality of measurements collected from the proposed 16 channel ERT system, a uniform background test is firstly conducted under the lowest possible current injection, 6 mA, and the voltage measurements $\mathbf{u_b}$ are captured in Figure 4.7(a). Signal-to-Noise Ratio (SNR) evaluates the precision of measurements by indicating the ability to produce the same results under the unchanged conditions [126]; it can be calculated by:

$$\mathrm{SNR}=10\log\frac{[\bar{v}]_i^{\,2}}{\sigma[\mathrm{v}]_\mathrm{i}} \tag{4.2}$$

where $\sigma[\mathrm{v}]_\mathrm{i}$ is the variance of measurements and $[\bar{\mathrm{v}}]_\mathrm{i}$ is the mean value of total measurements. Here we have collected 1000 frames of measurements for computing the system SNR. And in Figure 4.7(b), an example of the SNR histogram of 13 measurements under the first projection where the active electrodes are 1 and 2 is plotted. As expected, a higher SNR occurs at adjacent electrode measurements, i.e.

measurement 1 and 13, that have a larger trans-impedance, while a lower SNR occurs at opposite-electrode measurements that have a smaller trans-impedance. The overall average SNR over 208 measurements is 59.54 dB, demonstrating the good reliability of the device.

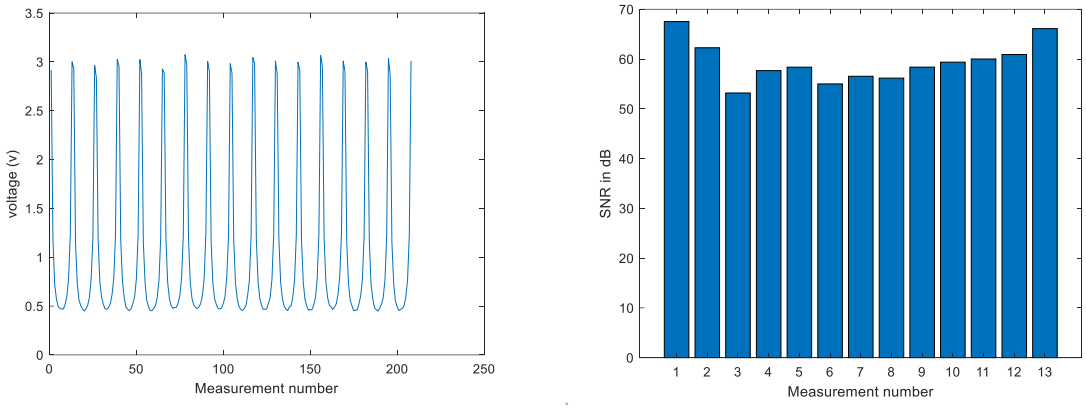

(a) (b)

Figure 4.7 (a) Background dataset plot (b) SNR plot of 13 measurements in background test.

4.4.2. Static Tests

To evaluate the performance of the proposed system, multiple static experiments were carried out in a cylindrical phantom of 25 cm diameter with 16 electrodes attached evenly on the periphery, as indicated in Figure 4.8. In all tests, saline is used as a background medium, and is prepared with the solution of NaCl and tap water. The image reconstructions involved in both the static and the dynamical tests were performed in MATLAB using the precalculated Jacobian matrix.

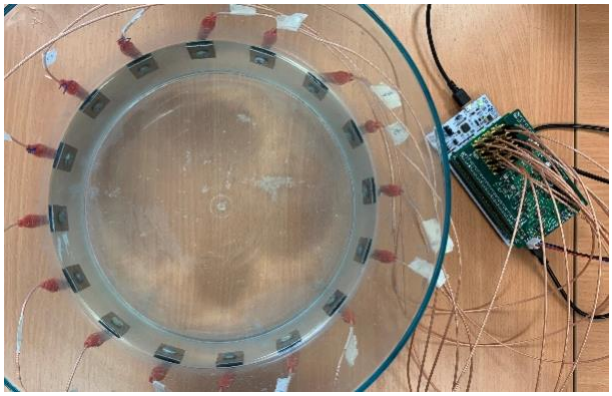

Figure 4.8 The EIT system for experiments

4.4.2.1.Single Sample Tests

Four sets of experimental tests using plastic (Teflon) rods in the sizes of 2 cm (small), 3 cm (medium) and 4 cm (large) diameter, and a plastic ballpoint pen in the size of 5 mm (Xsmall) are reported in this section. In the large and medium sample cases, 6 mA current was injected; whereas 16 mA current was used to stimulate the system in the small and Xsmall sample tests. This is because the signal changes induced by small inclusions are not as significant as those by larger inclusions and are more vulnerable to the background noise. Each object was placed at various locations within the tank, and results are displayed and compared with the real distributions in Table 4.1-4.3.

Table 4.1 Large sample tests.

Location1	Location2	Location3	Location4	Location5	Location6	Location7
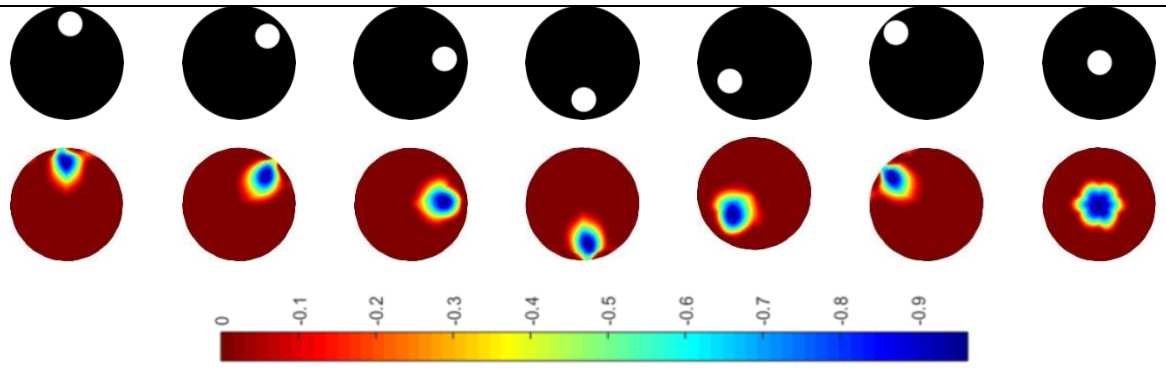						

Table 4.2 Medium sample tests.

Location1	Location2	Location3	Location4	Location5	Location6	Location7
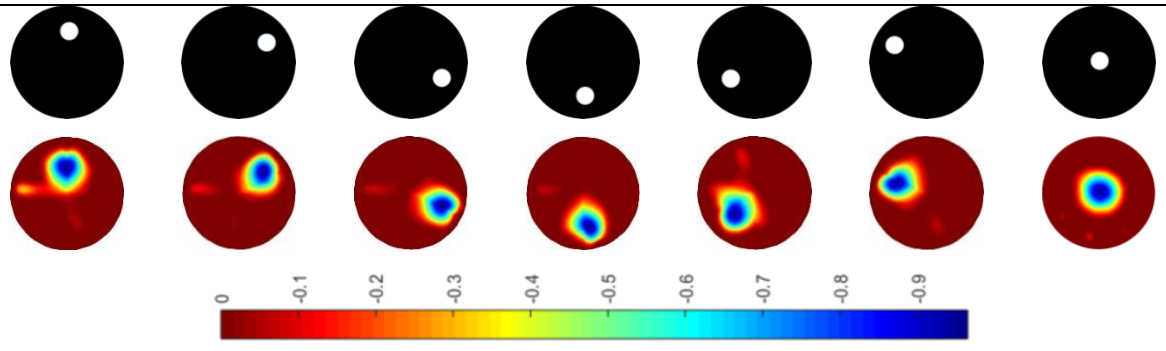						

Table 4.3 Small sample tests.

Location1	Location2	Location3	Location4	Location5	Location6	Location7
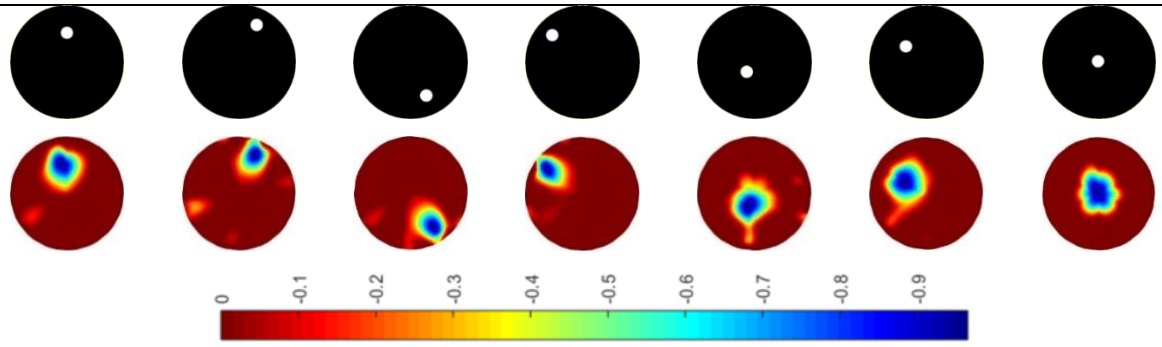						

Table 4.4 Extra small (Xsmall) sample tests.

Location1	Location2	Location3	Location4	Location5	Location6	Location7
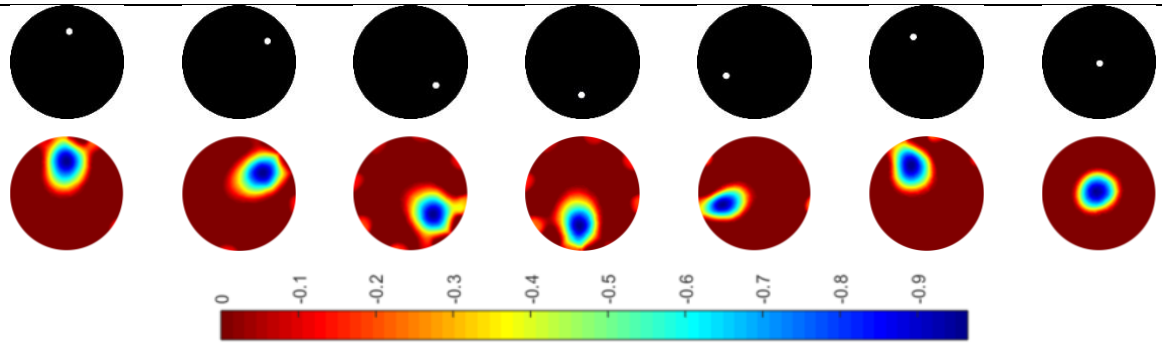						

As indicated from Table 4.1-Table 4.4, the reconstructed images are well defined within the view region, and can reflect the location variations when compared with the real distributions. However, notable image distortion can be observed as objects move further away from the boundary of the domain. This is caused by the inherent ill-posed nature of ERT that it has a high sensitivity to the changes occurring near the boundary. This poses a more significant effect when the targets are rather small and the changes in impedance by objects could be more severely contaminated by noises occurring at the boundary. Hence, even with a stronger excitation, images still struggle to preserve the shape and size of the real images in the small sample test (Table 4.3) and the Xsmall sample test (Table 4.4). It is worth noting that even the extra small object, whose size is only 0.04% of the area of the tank, is still detectable by the system. This is benefited from the high SNR of the ERT system and gives the system the confidence of capturing small obstacles and hence potential blockages at an early stage in the field applications.

It certainly needs to be pointed out that the reconstructed images seem to be insensitive to the diameter of the targets. In other words, the size of the objects in the reconstructed images are do not reflect the real size of the targets, especially in the case of Xsmall. This is largely because the ill-posed nature of an EIT problema and the image reconstruction method we chose in these tests, i.e. Tikhonov. The signal responses due to the insertion of an extremely small inclusion can be very small and this poses more difficulty to recovering the object. The difficulty also exists in tuning for the regularization parameter α. We need a relatively large α to stablize the system, on the other hand, a large α can contaminate the real signals and introduce the artifects. The sizes of the targets may not necessarily be revealed by the reconstructed object size but can be reflected by the value if not normalized. This can be demonstrated in the multiple sample tests where objects of different sizes are in the same tank.

Quantitative image quality analysis is reported to further compare the reconstructed images with the real distribution. Two evaluation parameters are employed here, i.e., Position Error (PE) and Shape Deformation (SD) from [127], and are plotted against locations. PE is preferably as small as possible so that it could provide reliable information on the location of blockages in the smart-metering applications. The PE of the four objects are plotted in Figure 4.9(a). Position errors in all tests are managed to be kept below 1 cm, which indicates good tracking of potential blockages. The SD plots of four samples at various locations are presented in Figure 4.9(b). The ability to preserve the shape and size of objects declines as the objects get smaller, as expected. Moreover, the variation of SD becomes larger as the size of objects increases. The SD performance could be further improved by applying an advanced reconstruction algorithm in offline post-process or applying a size orientated threshold technique.

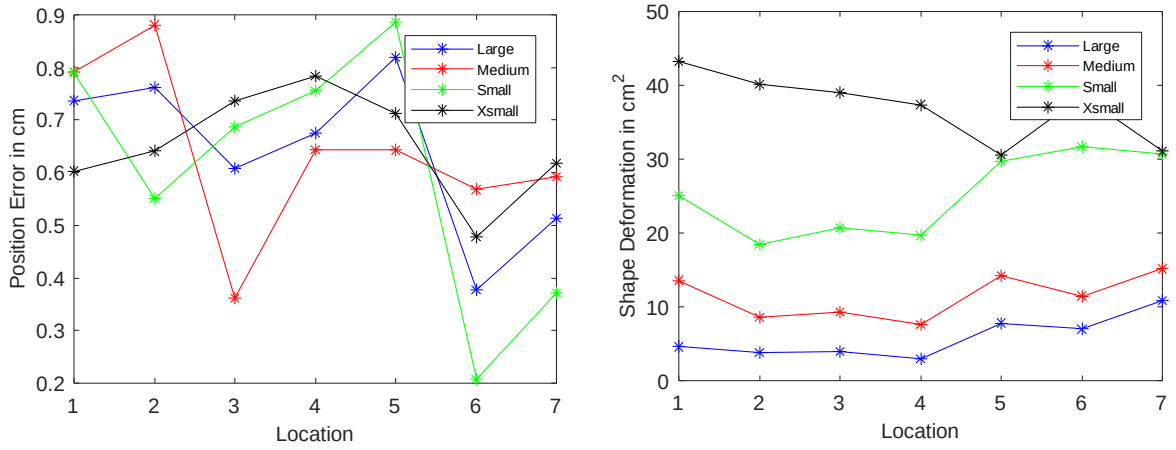

(a) (b)

Figure 4.9 Reconstruction accuracy plots (a) Position Error; (b) Shape Deformation.

4.4.2.2.Multiple Sample Tests

Another set of tests with more than two samples in the tank are also performed in Table 4.5. The results give a good insight of the distinguishability of the system. When the objects are placed equally close to the boundary, all of them can reveal themselves in the recovered images; however, smaller objects tend to have lower amplitude responses. Difficulties arise when any of the objects were placed in the center of the view region, and objects are effectively merged into one in the reconstructed images (i.e., Location3 and Location6 in Table 4.5).

Table 4.5 Multiple sample tests.

Location1	Location2	Location3	Location4	Location5	Location6	Location7
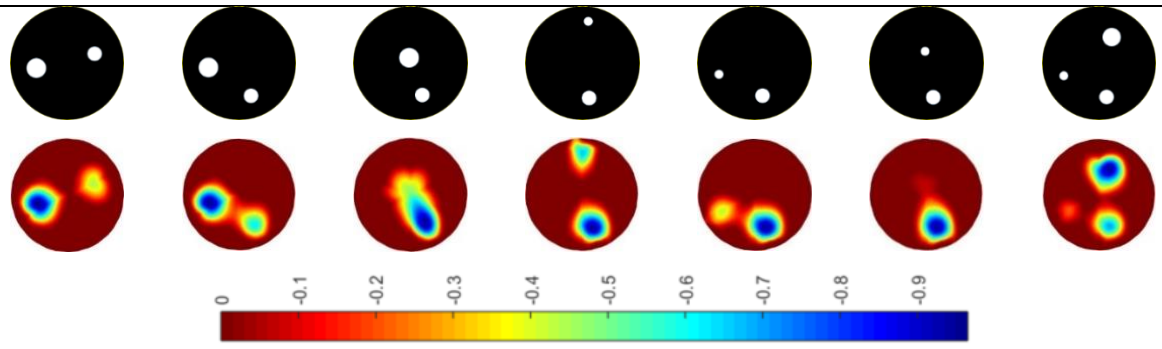						

4.4.3. Dynamical Tests

In order to study the feasibility of flow monitoring with the framerate offered by the proposed ERT hardware system, dynamic tests were carried out by continuously moving an object in this section. For the purpose of simplification, 2-dimensional flow simulation, which is accomplished using measurements obtained from one electrode plane, is considered.

Experiments were conducted using the same phantom setup as single stationary tests previously in 4.4.2 employing the large sample (4 cm diameter plastic rod). Two types of movement are studied: the circular movement where the sample moves along the inner wall of the tank clockwise (Figure 4.10(a)); the cross movement where the sample moves across the region along the diameter from one side to another (Figure 4.10(b), (c)).

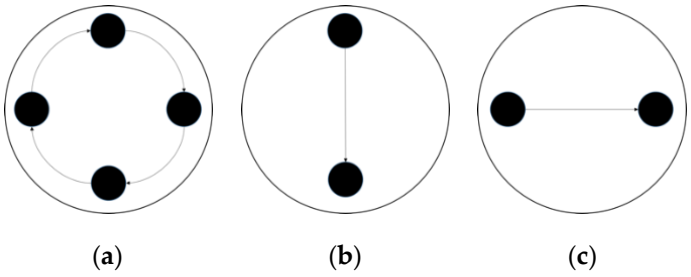

Figure 4.10 Movement indications of (a) circular (b) vertical cross (c) horizontal cross.

- *Circular movements*

The circular movement provides a good insight into employing ERT into monitoring dynamics within process equipment such as impeller-based mixers, hydro-cyclones and centrifugal separators [127]. Several reconstructed images along the movement path are presented in Table 4.6. The sample is well defined, even under the continuous movement, and this illustrates that the data capture speed is sufficiently high compared to the rate of movements.

Table 4.6 Large sample circular movement test reconstructed images.

Location1	Location2	Location3	Location4	Location5	Location6	Location7
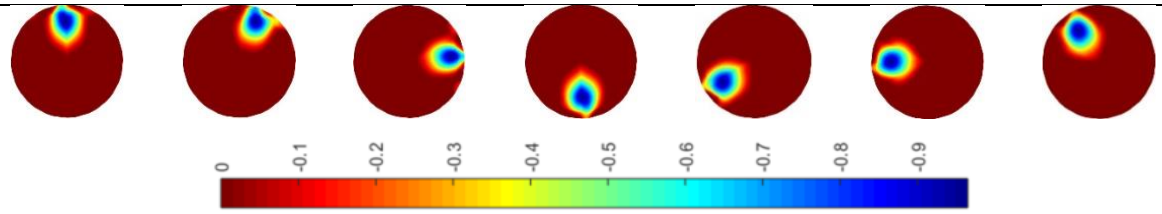						

To demonstrate the sample movement over the given time margin, a 3D volume model is introduced in Figure 4.11. In Figure 4.11(a), the top view of the sample motion describes the circular movement within the phantom and a helical 3D volume model in Figure 4.11(b) provides the time taken for such movement to complete. The 3D modelling helps not only visualize the movement of targets but obtain volume information given the angular speed derived from the system framerate (will be further discussed in Section 5.1).

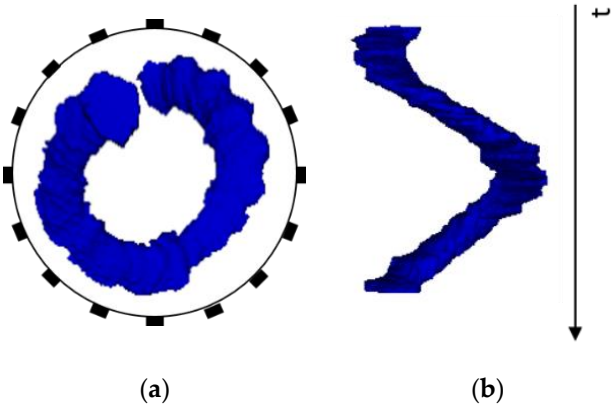

(**a**) (**b**)

Figure 4.11 Circular motion 3D volume model (a) top view (b) helical 3D view with time axis.

- *Along Diameter Movements*

The 2D cross movements can be extended into 3D processes where two electrode planes can be implemented; flow patterns in horizontal slurry transport pipelines [77] can then be investigated. Again, seven critical slices of images of each type of cross movements are displayed in Table 4.7 and

Table 4.8. The results prove that the movements are successfully monitored.

Table 4.7 Large sample vertical cross movement test reconstructed images.

Location1	Location2	Location3	Location4	Location5	Location6	Location7
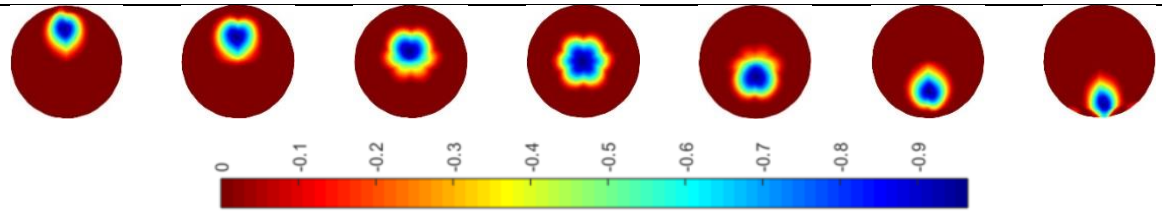						

Table 4.8 Large sample horizontal cross movement test reconstructed images.

Location1	Location2	Location3	Location4	Location5	Location6	Location7
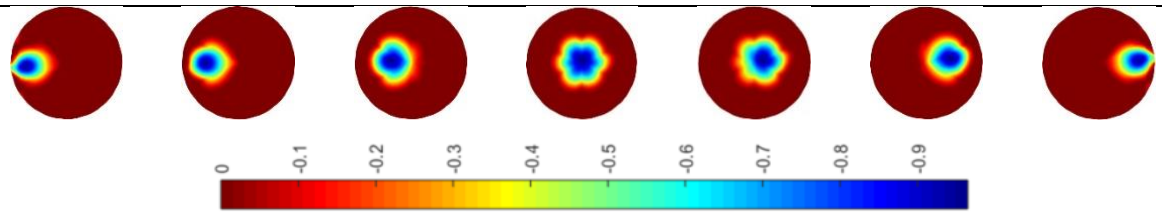						

4.5. Conclusion

Existing ERT devices did not have meet the cost requirements for the proposed sewer flow measurement applications. Therefore a bespoke ERT data acquisition hardware was designed and demonstrated its use to image pipes with different flow constituents including solids and liquids. The impact of this development is an embedded sensor monitoring the quality and rate of flow in water and sewage networks, feeding into water quality and availability improvements.

The device incorporates a serial measurement structure with a common mode error cancelling method to allow for a cost-effective but fast data capture design. Furthermore, it features the flexibility of injecting current from 6mA to 18mA whilst being able to repond to the wide synamic load range. A data collection rate of 14 fps, as well as an overall mean SNR of more than 59.54 dB, has been achieved. The system performances in both the static and dynamic range were studied in lab-scale experiments. With the smallest sample size reported being 0.04% of the phantom, the system managed to locate inclusions with a position error of less than 1 cm. Also, successful motion tracking was achieved by clear visualization of the movements.

Chapter 5 Dynamical ERT imaging

ERT has been reported featuring high-temporal resolution but low spatial resolution. Such characteristics make the ERT system a good candidate providing functional information by the combination of a time-series of ERT images. In this chapter, we will visualize and analyze dynamical movements by post-processing the ERT images provided by the DAQ device developed in Chapter 4. In the absence of the field testing for sewage flow measurements, we demonstrated such dynamical capabilities using lab-based phantom experiments. The visualization was fulfilled in the content of recovering handwritten letters in a 2D water based phantom. The results from this study showed that complex shapes can be obtained thanks to the good temporal resolution, although this would not have been possible in individual images with low spatial resolution. Moreover, we demonstrated the dynamical imaging capability of the ERT system in multiphase flow measurements, i.e.velocity estimation. The functional ERT offers an opportunity in integrating control systems into sewer flow systems to further facilitate the automation of the systems. The content is based largely on publication 4 and part of publication 2. The focus of this chapter is time correlated reconstruction and more importantly dynamical image representation through targeted post-processing.

5.1. Introduction

Recent advances in computing technology and the increasing fusion of computer and machine into daily life have led to notable developments in seamless human-machine interface (HMI) system. Such systems can recognize hand gestures and motions, and therefore allow the control of robotic machines to perform dexterous tasks. The establishment of this link between humans and machines can help with better control of robotics in various applications, such as surgery operations, restoring a degree of normality to amputees or safely handling hazardous materials. [128-130]. Recent years have also seen scientific growth in various domains of the process engineering, including process optimization and advanced instrumentation and control. In these areas, HMIs replace manually activated switches, dials and other controls with graphical representations of the control process. Since the HMI is software

based, they achieve controls with software parameters, allowing them to be adapted and adjusted easily[131].

In the industrial field, from food to petrochemical industries, the control of flow is the key problem from both economic and product quality point of view. This requires the high precision of flow metering in order to precisely control the processes. Accurate flow measurements and control largely depend on the flow velocity calculation, where difficulty arises from the complex flow profiles. In the case of dynamic multiphase flow, the continuous transition of flow patterns is one of the most important factor that generates errors during flow measurement. Thus, the comprehensive determination of phase velocity profiles becomes crucial[77].

In this chapter we will investigate the functional imaging aspect of ERT systems to assist the automization of flow monitoring and control. It is well known that ERT has low special resolution but can offer a very good functional information resulting from high temporal resolution; accordingly it can unfold the temporal information by post-processing a series of ERT images. This dynamical capabilities can be demonstrated by i) combinging dynamical images for creating 2.5D shapes, as shown in Figure 5.1, to visualize objects movements, and ii) dynamical image processing for velocity profiles calculations. The motion visualization provides graphical description of the process whilst the velocity computation delivers a quantitative analysis of flow; hence they together make ERT a potential HMI tool in controlling flow operations.

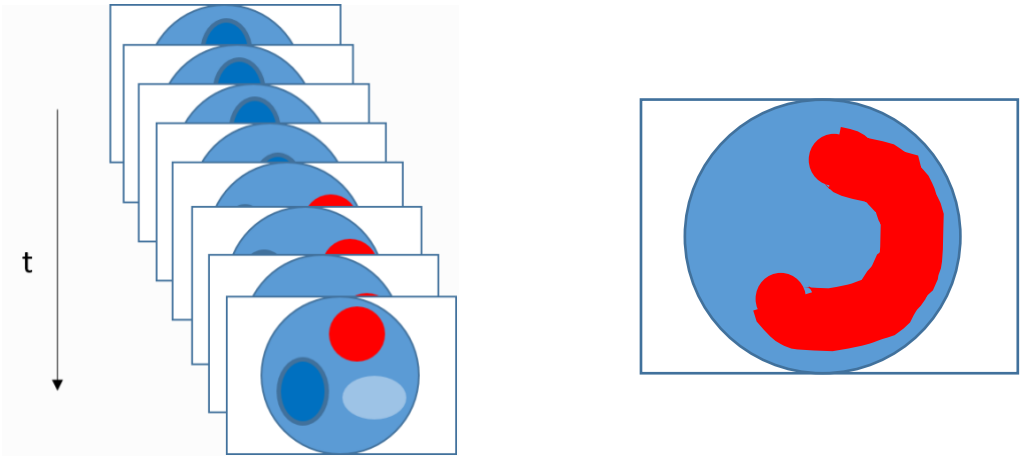

Figure 5.1 Diagram of 2.5D images

We will use the ERT device designed in Chapter 4, which has a data capture rate of 14 fps, to perform both the in-water handwritting and velocity measuring tasks. Experiments will be conducted in a 2-dimentional lab-based phantom for preliminary study. The key method involved in both scenarios is the temporal ERT reconstruction, which accounts for the time correlation between adjacent frames of data in the dynamical tests. Further post-processing of reconstructed images will then unveil the desired information. The motion visualization functionality was demonstrated by recovering handwritten letters in a 2D water-based phantom. The time-series flow information can be globally interpreted into geometric figures, and can be further fed into controllers to achieve automation. Specifically, we proposed the handwriting recognition scheme to recover the written letters/shapes. Analysis of image similarity between actual handwriting movements and the one follow with the ERT scheme shows a good correlation and demonstrates how an ERT system can be used to create a robust handwriting in water. The impact of this study is introducing ERT as an HMI tool not only facilitating the industrial flow process engineering but also offering a vision based inertial sensing method. Flow velocity analysis is particularly favourable in multiphase flow measurements and has been established for many years. Typically, cross-correlation method has been adopted for estimating velocity profile in ERT. For example, in [132-134], measurement of angular velocities of swirl flows using ERT was examined. A dual-plane ERT system was also designed to measure the disperse phase velocity in gas-liquid flow in vertical upward pipe in [135, 136]. In this section, the pixel based cross-correlation method is adopted to compute the time-shift over which the targeting phase travels for a given distance and the velocities can be calculated accrodingly. The reported deviation of the calculated velocities from the real ones will also be considered.

5.2. Methodology

5.2.1. Movement visualization

A Successful movement tracking practice requires both an EIT sensing system that could track the motion of dynamical movements, and a trajectory recovery technique to postprocess successive ERT

images. Essentially, the object movements in the water can cause time-varying conductivity distribution changes; and hence can be considered as dynamic ERT problem. Solving such dynamic estimation, questions arise how to estimate parameters that are time-varying. The ordinary (static) imaging algorithm, which reconstructs individual frames of data, would not be an optimal approach in the dynamic situations. Therefore, we will apply the temporal on-step solver with Tikhonov regularization explained in 3.1.2.4. Figure 5.2 presents the overal procedure of the handwriting implementation.

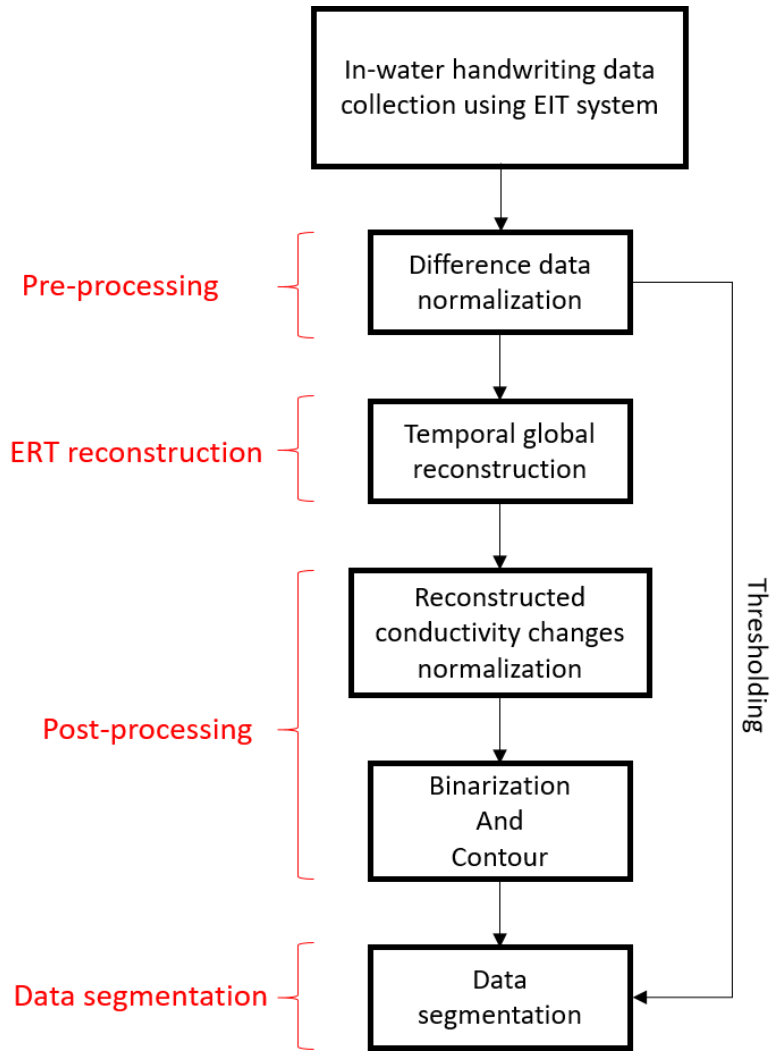

Figure 5.2 In-water handwriting procedure

- *Step 1: Pre-processing*

The handwriting practice can be intrinsically formulated as time-difference ERT problem. The difference data that is created by the movements of 'pen' should then be distinguished from the random system noises. Here we introduce a pre-processing method, difference data normalization, which will

globally scale the difference data to the range of -1 and 1. Then we will use the normalized difference as a reference to separate between letters, i.e. Step 3 Data segmentation.

- *Step 2: Temporal reconstruction*

The Temporal reconstruction method is detailed previously and we will re-arrange the equations *(3.49)* *(3.50)*:

$$\widetilde{\Delta\boldsymbol{\sigma}_t} = \boldsymbol{B}\widetilde{\Delta\boldsymbol{u}_t}$$
$$\boldsymbol{B} = \left(\boldsymbol{J^T W J} + \boldsymbol{a_1}\mathbf{diag}(\boldsymbol{J^T J}) + \boldsymbol{a_2 eye}\left(\boldsymbol{size}(\boldsymbol{J}, \mathbf{1})\right) + \boldsymbol{a_3 R_3}\right)^{-1}\boldsymbol{J^T W} \quad \textbf{(5.1)}$$

This can significantly speed up the computation as pre-calculations of matrix *B* was made before the input of difference data series $\widetilde{\Delta u_t}$.

- *Step 3: Post-processing*

Now that we have successive frames of ERT images of the handwriting movements, it is generally agreed that post-processing is required to stabilise image quality for further analysis. There are mainly two steps involved in this process, binarization and contouring.

Due to the inherent ill-posed nature of the EIT problem, the signal responses to the changes occurring near the boundary of the domain are stronger than those in the middle of the medium. Handwriting trajectories can happen aross the entire phantom. Hence, further normality is firstly needed to so that the uniform resolution in the imaging region among all the frames can be achieved. Here we scale the reconstructed conductivity changes to the range of 0 to 1. Subsequently, binarization was achieved by thresholding the ERT images such that only the pixels that can reflet the movements are emphasized and marked as one. Following that is the contouring, which preserve the movement trajectories and form the final motion figures. The significance of binarization is distinguishing the targets from the rest of the flow and hence tracking the particular movements of interest.

- *Step 4: Data Segmentation*

A data segmentation process refers to identifying the start points and the end point of a stroke. To simplify the problem, we only considered single-stroke writings such that each charater/shape was completed in one stroke and the ‘Pen’ was taken out of the water once one character is written.

Wherefore, segmentation is fundamentally to differentiate the signal changes caused by the actual writing operation from the background noise. The norm of difference between background and inclusion data calculated previously in the pre-processing is used here to seperate between letters. The time window within which the writing is happening can then be marked by the norm above a predefined threshold. The threshold is set empirically and in the manner that any changes caused by handwriting motion would be captured whilst background noises would be discarded; hence will differ in individual situations. Data segmentation allows us to extract the frames that contain the writing information.

5.2.2. Velocity measurement

A velocity field can be inferred by computing correlations between images of different time instants based on a sequence of reconstructed tomographic images as illustrated in Figure 5.3(a). In a system with one ring of electrodes, the cross-sectional plane of interest is divided into finite elements, which is defined as the pixel correlation method [77]. For instance, in Figure 5.3(b) the view region is discretized into 5x5 pixels. The procedure of computing flow velocities can be illustrated in Figure 5.4.

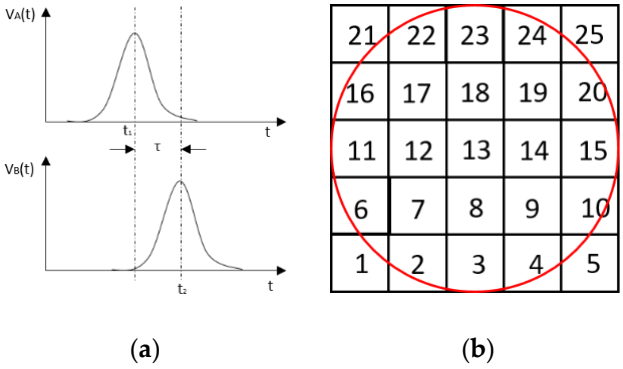

(**a**) (**b**)

Figure 5.3 (a) examples of signals from pixel A and B; (b) indication of pixel units division within the view region.

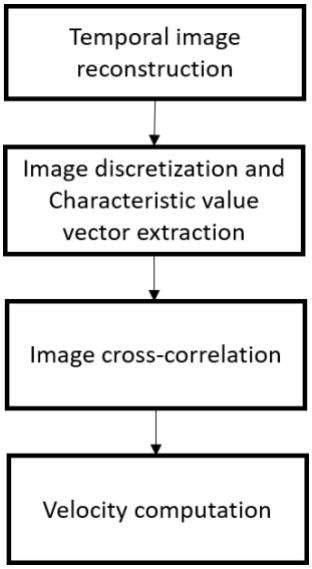

Figure 5.4 Velocity measurement procedure

To begin with, a collection of time-series measurements are captured and reconstructed using temporal imaging method. Each reconstructed image is discretized into finite number of pixels, with each unit having a value indicative of the resistivity of the region it occupies. Then, the profile of individual pixels (i.e., the characteristic vector) can be obtained from the variations of its resistivity estimation over the entire capturing time frame, as shown in the example in Figure 5.3(a). By discretely cross-correlating between two targeting pixels' profiles (5.2), the resulting vector of correlation coefficients $R_{AB}(\tau)$ peaks at the time that can reflect the delay between signals V_A and V_B, i.e., τ [127].

$$R_{AB}(\tau)=\frac{1}{N}\sum_{n=1}^{N} V_A(n\Delta t)V_B(n\Delta t+\tau)\,, \tag{5.2}$$

where signal V_A and V_B are the characteristic vectors of pixels A and B that the cross-correlation is applied to; N is the length of vector, and Δt is the time-step.

Subsequently, the resulting time delay τ together with the distance, which can be either angular or axial depending on the applications, the velocity can then be given by:

$$v=d/\tau$$
$$\omega = \theta/\tau \tag{5.3}$$

5.3. Experiments and Results

A complete ERT system is composed of three main components, namely sensors, the data acquisition system, the computational software. Both experiments were conducted using the ERT data acquisition system developed previously in Chapter 4 (shown in Figure 4.2), which can collect data at a speed of 14 fps. Two tests were set up in two water tanks with different diameters but both having one ring of 16 electrodes to perform 2D dynamical movements.

5.3.1.Handwriting visualization

The handwriting exercise is carried out in the water tank using a plastic rod as a pen, as shown in Figure 5.5. Measurements are taken under a current injection of 8mA, 50kHz. Letters are written to in the presented phantom and recovered using the proposed methods. Here we use the same value of regularization parameters a_1, a_2, a_3 for all handwriting practice since the experimental setup is the same among all tests. They chosen based on expirical experience and they are 0.1, 1, 0.1 respectively.

(a) (b)

Figure 5.5 (a)ERT sensor water phantom and (b) a plastic rod

5.3.1.1. Single letter

The EIT based handwriting is implemented by the combination of many low spatial resolution imaging creating letter using points on path of trajectory of the plastic bar. Individual EIT images are synthesized to produce letters. Figure 5.6(a) shows images of frame 85 to 109 involved in forming a letter L in Figure 5.6(b). Each frame acts as a point in letter L. 65 informative frames out of a total number of 238

frames of data that have been collected can be extracted by applying data segmentation method to the graph in Figure 5.7, with a threshold of 0.1, and superimposed to form the letter.

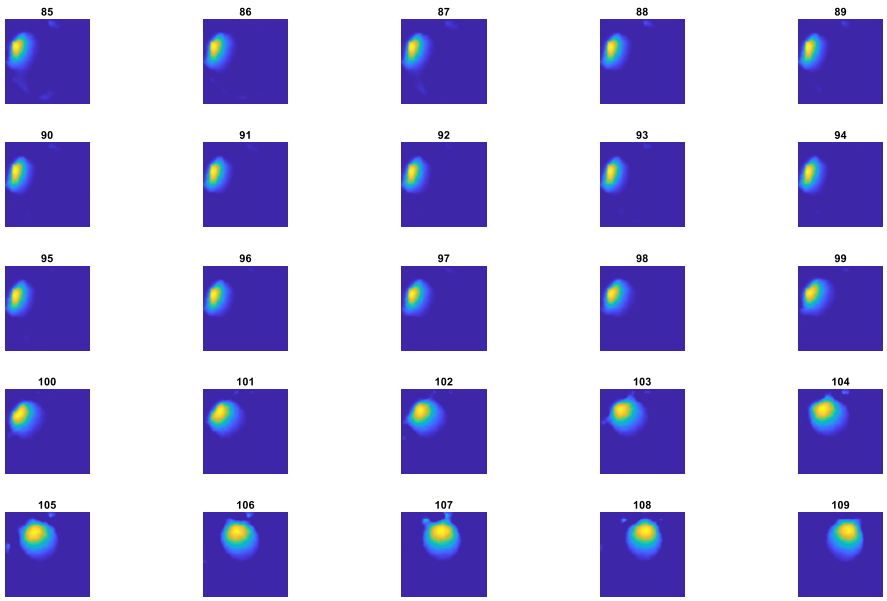

(a)

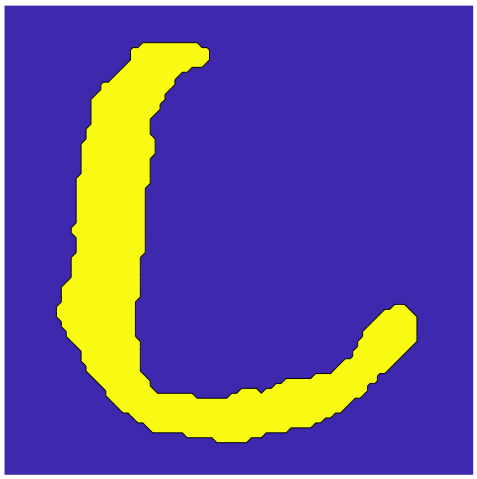

(b)

Figure 5.6 (a) Frames of EIT images used to construct letter L (b) Letter L

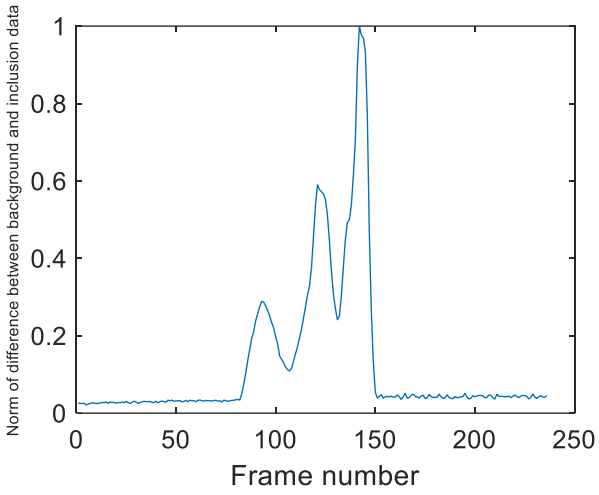

Figure 5.7 Norm of difference between background and inclusion data in “L” test

5.3.1.2. Multiple letters

More challenging applications of multiple letter recognition are investigated in this section. Figure 5.8 shows the letters of word EIT, XMAS, DAN, HAN, manuch, soleimani.

(a)

(b)

(c)

(d)

(e)

(f)

Figure 5.8 Reconstruction of word (a) EIT, (b) XMAS, (c) DAN, (d) HAN, (e) manuch, (f) soleimani

In the example of the word 'XMAS', a total 640 frames of EIT images were considered and the norm difference is plotted in Figure 5.9. When the norm is smaller than 0.1, it indicates that the rod is out of the water. Hence, one can see the distinct frame window of each letter in the word 'XMAS'. It is possible to use various letter recognition methods to further enhance these handwriting, but this is beyond scope of this work. Using finger pressure point on a fabric based EIT [137, 138] using the same method presented here can give rise to a fabric-based handwriting and use of a dielectric (plastic rod) with electrical capacitive tomography [139] enables in air handwriting.

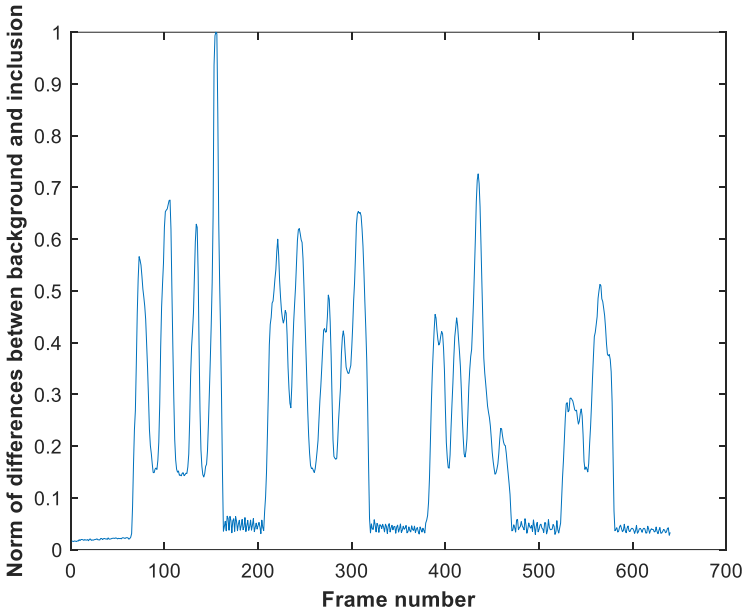

Figure 5.9 Norm of differences between background and inclusion data in XMAS test

5.3.1.3.Correlation Analysis

To evaluate the performance of the EIT handwritings, a Pearson correlation coefficient is used, which compares the similarity between the real and reconstructed images over the entire view region.

In the example another version of the word ‘EIT’ is used. A printed word ‘EIT’ with the thickness of lines the same as the diameter of the plastic rod is created, as shown in Figure 5.10(a). Then, the in-water handwriting was accomplished by making the plastic rod follow the trajectory of printed word. Individual letter in the reconstructed word, presented in Figure 5.10(b), is compared to the printed written letters accordingly. The correlation coefficients of letters ‘E’, ‘I’, and ‘T’ are 0.647, 0.712 and 0.548 respectively.

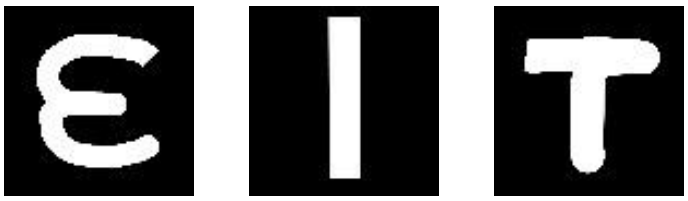

(a)

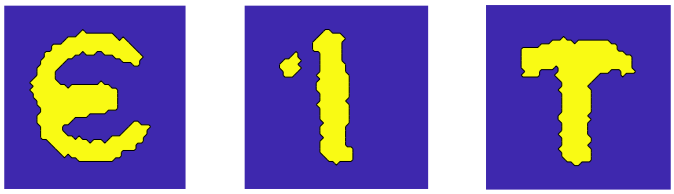

(b)

Figure 5.10 (a) Printed writing (b) reconstructed writing of letters ‘E’, ‘I’, ‘T’.

It’s also worth noting that the letters with complex trajectories poses more difficulty on EIT reconstruction and this can be confirmed with the lower coefficients. Overall, the coefficients are all above 0.5, which reveals a satisfactory correlation of the EIT reconstructed letters with the printed ones.

5.3.2. Velocity measurement

The velocity measurements are developed based on the dynamical experiments in Chapter 4.4.3, in which circular and across the diameter movements were considered. The images presented previously can provide a good insight into the capability of capturing dynamical movements with the designed ERT device. Here we will further interpret the temporal images into velocity information.

The circular movement starts from pixel 23 and completes one lap in 366 frames. Therefore, pixel 23 is set as a reference whose characteristic vector against frame number is plotted in Figure 5.11. The pixel profile plots provide information of the time instances when the sample enters and leaves the corresponding pixels. In the example of pixel 23, as described in Figure 5.11, the sample was placed at pixel 23 before the beginning of capturing and started moving out of the pixel after frame 10 until frame 57 when the object was completely out of this pixel; the object appeared back in pixel 23 from frame 324. The circular movement finishes one lap within 366 frames, which can be calculated as 26.14 s given that the data capture speed is 14 fps. This is comparable to the actual time spent on completing one lap, which is measured by a timer, i.e., 26.38 s.

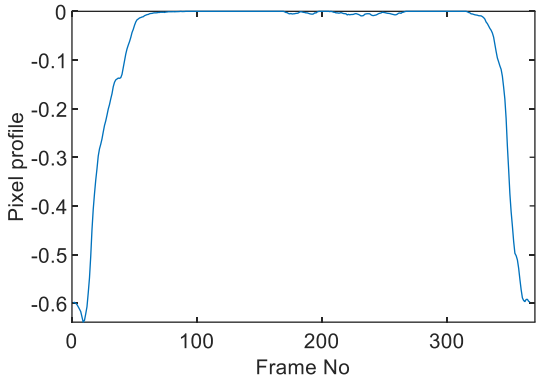

Figure 5.11 Characteristic value vector plot of pixel 23.

Six pixels along the circular path are chosen to correlate with the reference pixel and results are displayed in the time-shifting manner in Table 5.1. Transit time can then be referred to the frame number of the peak in each cross-correlation plot. The time-step of adjacent frames, which is the reverse of the framerate of DAQ device is given, and the speed calculation is hence attainable.

Table 5.1 Pixel characteristic vector plots and cross-correlation plots of circular movement.

	Pixel 20	**Pixel 15**	**Pixel 9**
Pixel profile plot	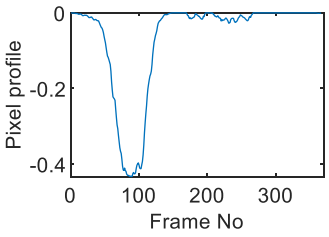	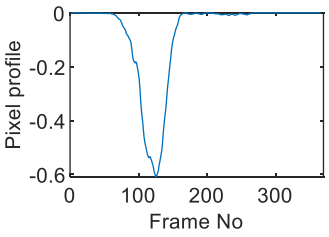	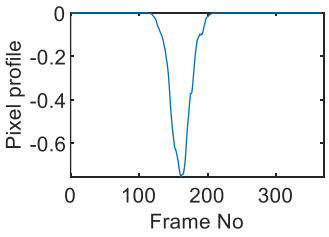
Cross-correlation	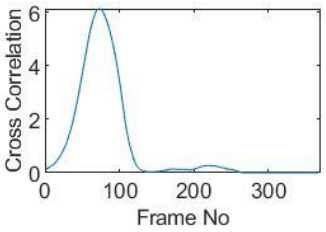	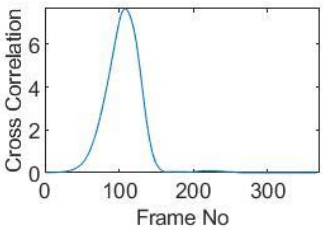	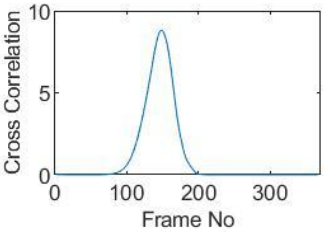
	Pixel 3	**Pixel 7**	**Pixel 11**
Pixel profile plot	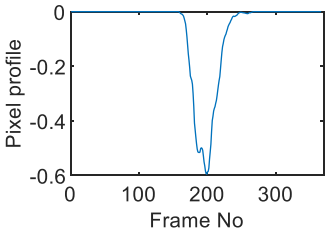	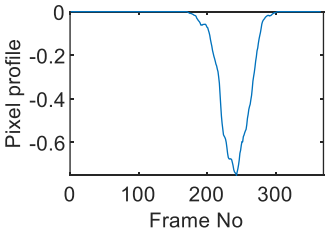	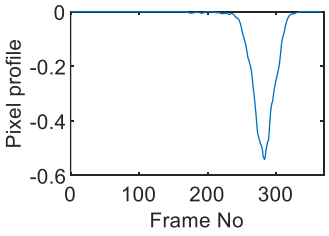

Cross-correlation			
	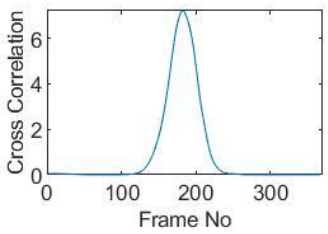	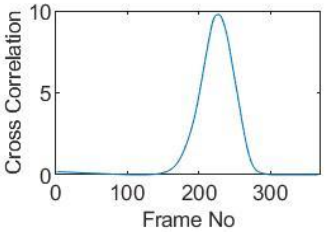	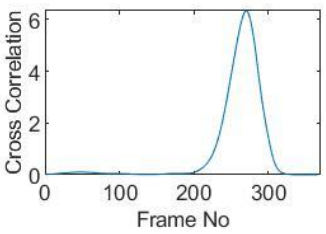

The frame numbers of the peaks in the cross-correlation plots in Table 5.1 are 72, 107, 147, 181, 225 and 269 in the displayed order. The increase in the peak frame numbers in the cross-correlation plots indicates the time shifting.

The angular speed can be performed by:

$$\omega = \frac{\theta}{\tau \times v_{DAQ}} \tag{5.4}$$

where θ is the angular distance between two pixels in radius, τ is the transit time in frames and v_{DAQ} is the data acquisition speed which is 0.072 s per frame. For simplification, a quarter of one lap, which is from pixel 23 to pixel 15, is considered. The cross-correlated transit time, τ, is 107 frames; hence, the angular speed can be calculated as 0.207 rad/s. The accuracy of the speed calculation can be analyzed in comparison with the measured angular speed. The measured time taken for the object to travel over the angular distance of π/2 is 7.81 s, which yields an average angular speed of 0.201 rad/s. Therefore, the relative error of using the cross-correlation method is 2.98% when compared with the measured speed; this is acceptable and proves that the strategy of using cross-correlation to obtain the speed measurements is feasible. The error is partially contributed by the imaging algorithm as the cross-correlation is essentially accomplished from a sequence of reconstructed images and the image quality can play an important role in the success of cross-correlation results. Also, the random error of timing the instance when the object arrives at 90-degree location can result in the difference between the measured time and the cross-correlated time, thereby giving the corresponding speeds.

- *Along Diameter Movements*

Tests were also conducted by moving the object across the domain in vertical and horizontal directions, as mentioned previously. In these tests, it started at pixel 23 in the vertical direction and arrived at the opposite side of the tank, i.e., pixel 3, within 121 frames; started at pixel 11 in the horizontal direction and arrived at pixel 15 in 121 frames of time. Thus, pixel 23 and 11 are set as reference and their characteristic vectors are plotted in Figure 5.12(a), (b) respectively.

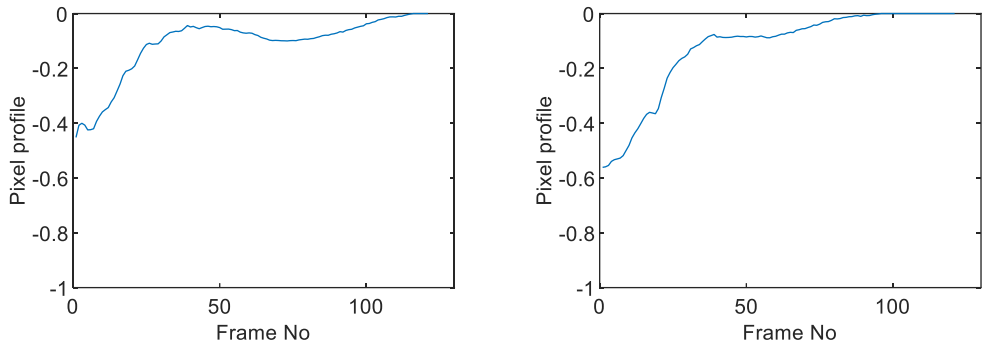

Figure 5.12 Characteristic value vector plot of (a) pixel 23; (b) pixel 11.

Three pixels along the moving path in each case are chosen to cross-correlate against the reference pixels. Similar to the circular movement, the cross-correlation plots peak at the frame numbers that represent the travel time spent on moving from the reference pixels to the corresponding pixels. Results are shown in Table 5.2 and Table 5.3.

Table 5.2 Pixel characteristic vector plots and cross-correlation plots of vertical cross movement.

	Pixel 18	**Pixel 13**	**Pixel 8**
Pixel profile plot	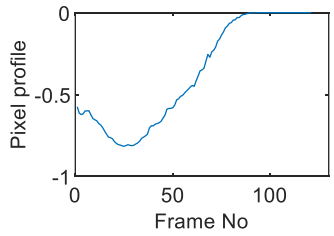	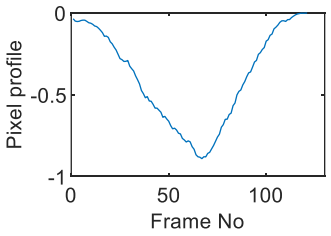	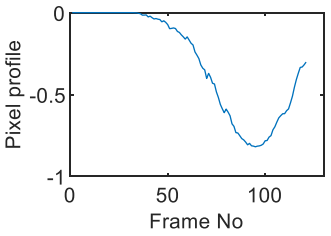
Cross-correlation	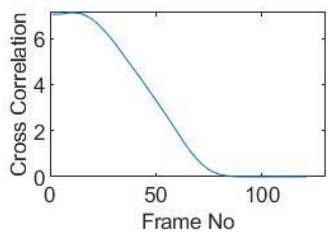	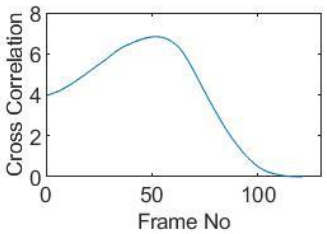	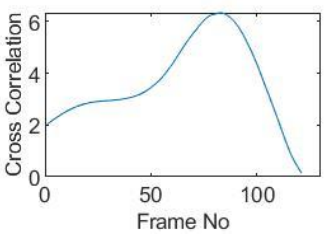

Table 5.3 Pixel characteristic vector plots and cross-correlation plots of horizontal cross movement.

	Pixel 12	Pixel 13	Pixel 14
Pixel profile plot	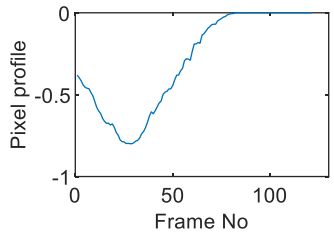	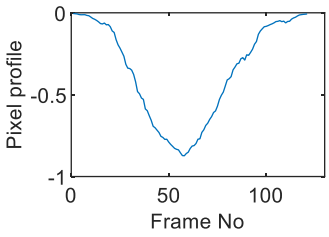	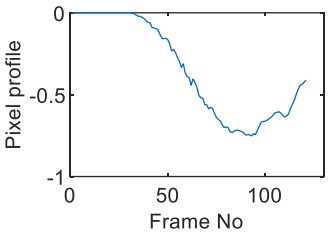
Cross-correlation	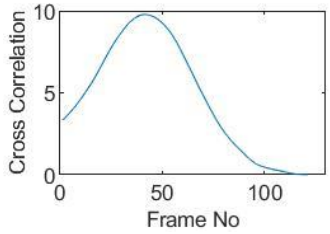	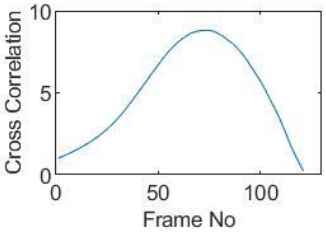	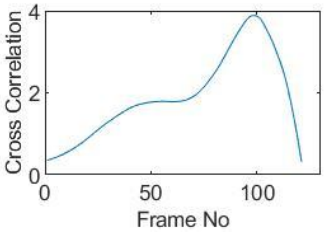

The frame numbers of the peaks of pixel 18, 13 and 8 cross-correlating to the reference pixel are 9, 51 and 82 respectively in the vertical movements; the frame numbers of the peaks in the cross-correlation plots of pixel 12, 13 and pixel 14 against pixel 11 are 41, 73 and 97.

The speed at which the sample travels along the path can be derived by the same principal as Equation 9 but with the metric distance between two targeting pixels instead. To illustrate, the cross-correlated average speed is calculated at which the sample travels from the reference pixel to the centre (pixel 13) in both the vertical and horizontal directions. Again, the accuracy analysis is shown in Table 5.4.

Table 5.4 Speed results of cross movements.

	Measured Speed (m/s)	Cross-Correlated Speed (m/s)	Relative Error (%)
Vertical	0.0265	0.0274	3.39
Horizontal	0.0186	0.0192	3.22

The relative errors of along diameter movements are slightly higher than those of circular movements, yet can still provide the confidence of employing cross-correlation to measure speeds. One of the reasons for to the larger relative errors is the image quality. As discussed, the image quality is one of

the most vital factors that determine the accuracy of the cross-correlated speeds. Circular movements occur near the periphery of the tank whereas the cross movements involve the object travelling across the whole domain. The inherent difficulties of recovering the objects placed away from the center lower the accuracies.

5.4. Conclusions

This chapter studies the dynamical imaging aspect of the ERT system. Demonstrating a functional performance for EIT despite its compromised static imaging ability can provide an opportunity for ERT to be applied in HMI intergrated control systems. In essence, the temporal information can be extracted from time-series ERT measurements taking advantage of its high data collection speed. In this chapter, we perfomed the dynamical imaging functionality in two scenarios: the movement visualization and velocity profile computation. They were demonstrated in a 2D water based phantom in this study and the insight of the tests translates the process parameters and measures for the future field testing.

The movement visualization was implemented by in-water handwriting practice where handwritten letters are recognized by analyzing measured data from electrical imaging in comparison with the background data. The combination of information generated from a series of ERT measurements makes the tracking of complex movements possible. The correlation between real handwriting and the one exactly followed by EIT shows satisfactory output. The second part of this chapter, we have explored the concept of using ERT system to estimate velocity. We use the pixel-correlation method for measuring disperse-phase velocity and presents a phantom feasibility study. The comparison between the true velocity and the measured one verifies the validity of the proposed method. The velocity study is extremely important as in real life it could be used to analyze the status of the flow, help establish flow patterns and indicate early stage of blockages.

The successful recovery of handwritten letters provides the confidence in visualizing dynamical movements globally. This method can extend its applications in tracking dispersed phases or obstacles

over long-term. The graphical representation of movements along with the velocity profiles can be further analyzed and learned to train for decision making in control systems.

Chapter 6 Limited region image reconstruction

The inherent ill-posed nature related to EIT problems has gained interest in developing various method to enhance the reconstruction quality. In this chapter, a limited region image recontruction method is introduced. This method aims to improve the image quality by limiting the reconstruction to the region of interest and hence reduce the impact of boundary noises. In this chapter, the method was proposed to work in the cancer treatment applications where EIT was introduced to track the tumour movements for aiding the traditional anatomial imaging modalities. Such applications would natually work with frequency difference reconstruction as opposed to time difference due to the frequency dependent impedance changes of biomaterials and the absence of time-reference data. The improvement brought in by the limited region reconstruction can be validated by lab-based. This method can also be applied to industrial processing systems to advance the system with better noise immunity and system robustness. Hence, though in this chapter we preliminarily demonstrate this limit region reconstruction for a medical application in frequency difference ERT, it will become useful for limited data ERT in partially full pipes in the next chapter.

6.1. Introduction

EIT is an imaging modality that injects electrical currents to the electrodes attached to the periphery of the electrically conductive objects and takes electrical measurements from the remaining electrodes to image the impedance distribution within the medium. EIT was introduced as a safe, rapid, non-invasive, and non-cumbersome way of visualizing electrical properties of human body tissues, especially large organs, by Barber and Brown [140]. As EIT virtually causes no adverse side effects (lack of radiation, no transport required), the method has become an attractive alternative to CT, MRI or ultrasound examinations. The key advantage of EIT is its relatively high acquisition speed, which can reach up to a few hundreds of frames/s in modern EIT devices as opposed to approx. 150ms/frame in CT and even

a few minutes per frame in PET[126]. Consequently, it provides the availability of powerful temporal filtering techniques, which means that it can detect the dynamic behaviour of tissues or process flows; and hence, it can provide unique temporal information difficult to obtain by other technologies at bedside or on sites. In the medical field, such algorithms allow EIT to be developed in thoracic functional applications, e.g. monitoring of mechanical ventilation, monitoring of heart activity and lung perfusion, and pulmonary function testing [141]. As a result, EIT can be introduced as a guidance during a treatment session, though it may not be available of the same level as in the diagnostic stage. Studies on combining EIT with other slow but high spatial resolution imaging systems, cone beam computed tomography (CBCT) for example, have been done [142-144]. In these works, EIT is employed to exact and provide lung motion information to CBCT for motion compensation so that more accurate tumour imaging can be achieved for image-guided radiation therapy. However, no direct monitoring of the object of interest, i.e. lung tumour, has been reported. Obviously, this is epecially challenging with the existence of pleural cavity together with other organs where the impedance changes due to the movements of the tumour could be shielded or contaminated by the ones caused by other organs. Such problem is also commonly encountered in the flow monitoring that activities/noises happening outside the region of interest (ROI) can pose effect on the measurements and image reconstructions can be disturbed. For example, the deposition on the pipe wall can affect the EIT readings in the flow measurement applications; on the contrary, the liquid or gas in the pipeline can disturb monitoring of on the pipewall. Also, it is common in sewerage that the free-running wastewater normally fills part of the pipes; and solids often settle at the bottom of the pipe. In these cases, we only want to obtain the information near the bottom pipe wall and detect any potential blockages.

In this chapter, EIT is presented as a direct object movement tracking tool. We tackled the problems of system instablity arisen from the noises from outside the region of interest by the localised method. That is restricting the reconstruction to the pre-defined ROI. In the tumour tracking application, the prior diagnostic knowledge provides the ROI within which the tumour is moving; whereas, within the sewers ROI is determined depending on the applications. By applying such localised reconstruction techniques, the sensitivity within the ROI can be refined and the image resolution can therefore be

enhanced [145-147]. Successes of introducing localised reconstruction strategies to improve image quality have been obtained both in industrial and medical areas, such as multi-phase pipeline flow analysis [148], assessment of regional lung ventilation [149-151] and potentially vocal folds monitoring [145]. Additionally, in the cases when baseline data is unavailable, frequency difference EIT (fdEIT) reconstruction that recovers the changes in impedance with respect to stimulation frequencies instead of time (tdEIT) will be implemented. This is based on the frequency dependent impedance of bio-samples and the development of multi-frequency EIT with a high data acquisition speed brings feasibility of fdEIT to clinical tracking applications [152]. It has also been found valueable in the practical industrial operations where the conductivity of continuous phase always varies due to the changes in fluid temperature, ionic concentration, and internal engergy conversion in fluids and it is impossible to find a reference dataset. Feasibility studies of applying fdEIT in industrial applications have been proposed previously[153].

The idea of using fdEIT within the localized region for tumour tracking application was brought up in [154], however, it was only demonstrated with simulation results and was lacking experimental evidence. In this work, following the success of simulation results presented in [154], two-dimensional phantom experiments using bio-samples were implemented to study the feasibility of the proposed technique. Reconstructions were conducted by using the Total Variation (TV) functional [155] to overcome the over-smoothed effect brought by traditional Tikhonov regularization. Results will be compared with traditional global reconstruction as well as mathematically modified global reconstruction to further validate and verify the proposed methodology; and hence offer the confidence in further in vitro or in vivo experiments.

6.2. Methodology

6.2.1. Frequency Difference EIT

EIT reconstruction is mainly categorized into two types, difference imaging and static imaging. Static imaging attempts to recover images of the absolute impedance distribution of the medium, which only

requires one set of measurements at one instance. Nevertheless, it has suffered from a limited amount of measurable information, unknown boundary geometry, uncertainties in electrode positions. Difference imaging, on the other hand, recovers an estimate of the change in impedance, and hence greatly overcomes the drawbacks of absolute EIT by cancelling out common errors through data subtraction to allow reconstructions to remain stable. One approach is to adopt a time-difference (tdEIT) imaging method, where the change of impedance in sensing area between two instances is reconstructed. However, in the cases of tumour imaging or stroke detection when time-referenced data is not available, tdEIT method is not applicable [156, 157]. Given the fact that biological tissues have different frequency responses [158, 159], impedance distribution inside the viewing region can be imaged by frequency difference reconstruction method (fdEIT), where measurements are taken under at least two frequencies.

However, a simple frequency difference may not completely benefit from the advantages provided by difference imaging as various errors may occur at different frequencies. Consequently, weighted fdEIT reconstruction was proposed and has been validated by numerical simulations and phantom experiments[152, 156, 160, 161]. It is particularly useful in medical applications where the background is always composed of other body tissues that also have frequency dependent characteristics, and then the background influence can be eliminated while maintaining the impedance contrast within the anomaly. Then the boundary voltage measurement ΔV_{meas} is denoted as:

$$\Delta V_{meas} = V_{f_2} - aV_{f_1} \quad a = \frac{<V_{f1}, V_{f2}>}{<V_{f1}, V_{f1}>} \tag{6.1}$$

where $\boldsymbol{V_{f_1}}$ and $\boldsymbol{V_{f_2}}$ are the measurements collected at frequencies $\boldsymbol{f_1}$ and $\boldsymbol{f_2}$ respectively; $\boldsymbol{a}$ is a frequency weight factor and $<\cdot,\cdot>$ is the standard inner product of two vectors.

In the medical applications, a set of stimulation frequencies will be carefully selected so that the frequency contrast of the anomalies is distinguishable from that of the background.

6.2.2. Localized Reconstruction

The conventional algorithm reconstructs images over the entire medium without emphasis on the information in the region of interest. The main drawback of the traditional algorithm is that the ill-posedness nature of EIT inherently results in a high sensitivity to the changes occurring near the boundary than those in the middle of the medium [162]. This will impose a more significant effect when the targets to be recovered are rather small and the changes in impedance caused by objects could severely be contaminated by noise occurring at the boundary. A strategy using all boundary measurements to reconstruct images within a pre-defined ROI is proposed in this chapter to enhance image resolution. Applying ROI is equivalent to the conventional reconstruction but with more independent measurements. Since Jacobian is non-uniform and ROI is normally defined to be far away from the boundaries, chances are noises occurring near the boundaries might not be picked up by ROI or not have the same effect as they are to the global reconstructions. In the content of medical tumour tracking applications, the location of the tumour can be initially determined by traditional CT scan and will be utilized as prior knowledge in the EIT reconstruction. Subsequently, a sub-volume, i.e. ROI, in this case can be selected larger than the size of the tumour to allow for the respiration-induced tumour movement. In the case of industrial flow monitoring, the decision of ROI is made dependent on the specific applications. For example, when the aim is to monitor the build-up on the pipe wall then the ROI can be made near the pipe wall with a width of thicker than the deposit allowance; or if we are to focus on the activities within the sewage flow in the partially filled pipe, then the ROI can be chosen to be the area of the continuous phase.

The conventional global reconstruction can be formulated as (6.2) considering that the sensing field is discretized into N_F elements and there are N_M independent measurements.

$$[J]_{N_M \times N_F}[\Delta\sigma]_{N_F \times 1} = [\Delta V]_{N_M \times 1}. \quad \textbf{(6.2)}$$

The principle of ROI reconstruction is restricting the image reconstruction process to a sufficiently large ROI that covers the anomaly completely. Therefore, the original medium can be divided into two areas: one is the conductivity-varying area, which is known as ROI; the other is constant-conductivity area

that $\Delta\sigma$ is zero. Assuming the ROI consists of N_{ROI} elements and the remaining elements N_P correspond to the zero conductivity change. Now the conductivity vector becomes

$$[\Delta\sigma]_{\mathrm{N}_F\times 1} = \left[\Delta\sigma_1, \cdots, \Delta\sigma_{N_{ROI}}, 0, \cdots, 0\right]^T \quad \textbf{(6.3)}$$

and yields the reconstruction equation:

$$[\Delta\sigma]_{\mathrm{N}_F\times 1} = \left[\Delta\sigma_1, \cdots, \Delta\sigma_{N_{ROI}}, 0, \cdots, 0\right]^T \quad \textbf{(6.4)}$$

$$\left[J_{N_M\times N_{ROI}} J_{N_M\times N_P}\right]\begin{bmatrix}\Delta\sigma_{N_{ROI}\times 1}\\ 0_{N_P\times 1}\end{bmatrix} = [\Delta V]_{N_M\times 1}. \quad \textbf{(6.5)}$$

Equation (6.3) can then be reduced to:

$$[J]_{N_M\times N_{ROI}}[\Delta\sigma]_{N_{ROI}\times 1} = [\Delta V]_{N_M\times 1}. \quad \textbf{(6.6)}$$

Therefore, the way of achieving the localised reconstruction is to restrict the Jacobian matrix to that in (6.6). The improvement of imaging can be interpreted by considering Jacobian matrix, which represent the sensitivity of the measurements at the boundary to the changes occurred inside the medium. By properly resizing the Jacobian matrix, the sensitivity to the changes happening outside the ROI can be weakened. This can bring several advantages:

1. The elements with constant conductivity are no longer included in the reconstruction process; therefore, the chances of accumulating zero-conductivity change can be reduced;
2. The condition for (19) to have unique solution is now $N_{ROI} < N_M$ rather than $N_P < N_M$;

6.3. Experiments

Feasibility studies of the proposed method were carried out experimentally. In this chapter, only 2-dimensional models were considered.

6.3.1. Experiment setup

Phantom experiments were established in a cylindrical tank of 19 cm diameter, with 16 equally spaced stainless-steel electrodes on the periphery (Figure 5.5). EIT measurements were carried out with a 16 channel multi-frequency KHU Mark 2.5 EIT system, which injects 2 mA currents over a wide range of

frequencies from 10 Hz to 500 kHz. An adjacent injection method was implemented that results in a total of 208 measurements per frame. To improve the precision of reconstruction, measurements are typically averaged over many data frames, and in the experiments presented, measurements at each location are results of averaging over 20 frames.

Three sets of experimental tests were considered. In all cases, four realizations of EIT measurements were collected: V_{f1} and V_{b1} corresponding to measurements of background only and with inclusion under 1 kHz stimulation respectively; and V_{f2} and V_{b2} corresponding to measurements of background only and with inclusion under 50 kHz stimulation respectively. Potato pieces were chosen to simulate tumour tissue and were placed in 0.5% saline water (conductive background). Objects to be reconstructed are in the sizes of 3.5 cm × 3.5 cm, 2.5 cm × 2.5 cm and 2 cm × 2 cm, and each is placed at horizontally various locations within a pre-defined area (bold yellow circle in Table 6.1, Table 6.2 and Table 6.3) in the phantom.

6.3.2. Experiment procedure

In each of the three cases, reconstructions can be computed in three different protocols:

1. Conventional global weighted frequency difference (GWFD) reconstruction as formulated in equation (6.1).
2. Modified global weighted frequency difference (MGWFD) reconstruction, which subtracts common errors in the background from the measurements

$$\Delta V_{data} = (v_{f_2} - \alpha v_{f_1}) - (v_{b_2} - \beta v_{b_1}),$$
$$\beta = \frac{< V_{b1}, V_{b2} >}{< V_{b1}, V_{b1} >}.$$

3. Limited region weighted frequency difference (ROI_WFD) reconstruction. The region of interest is defined by applying a threshold of 0.6 over the entire view region.

As suggested above, in addition to the conventional global reconstruction, a modified global reconstruction that subtracts the common background noise from the original datasets was also performed to compare with the proposed method. Considering the tumour tracking application, where

background data is no longer available, MGWFD reconstruction is only accessible in the lab scenario for verifying the significance of the proposed technique.

Image reconstructions were performed by solving the forward problem using EIDORS and implementing Split Bregman Total Variation regularization to solve inverse problem. The resulting impedance distribution is normalized since only the size and location of the objects are considered.

6.3.3. Results

In this section, reconstructed images of three samples using the proposed method, i.e. ROI_WFD, as well as the conventional algorithm with and without data modification are presented. All three sets of results are compared with real images. When applying ROI_WFD, the reconstruction region is limited to the ROI which is previously defined and is compared with the view region within the yellow solid circle in each real image. That is the ROI_WFD results presented in Table 6.1-Table 6.3 are zoomed-in view of the phantom region.

Table 6.1 Theoretical model and reconstructions of large sample

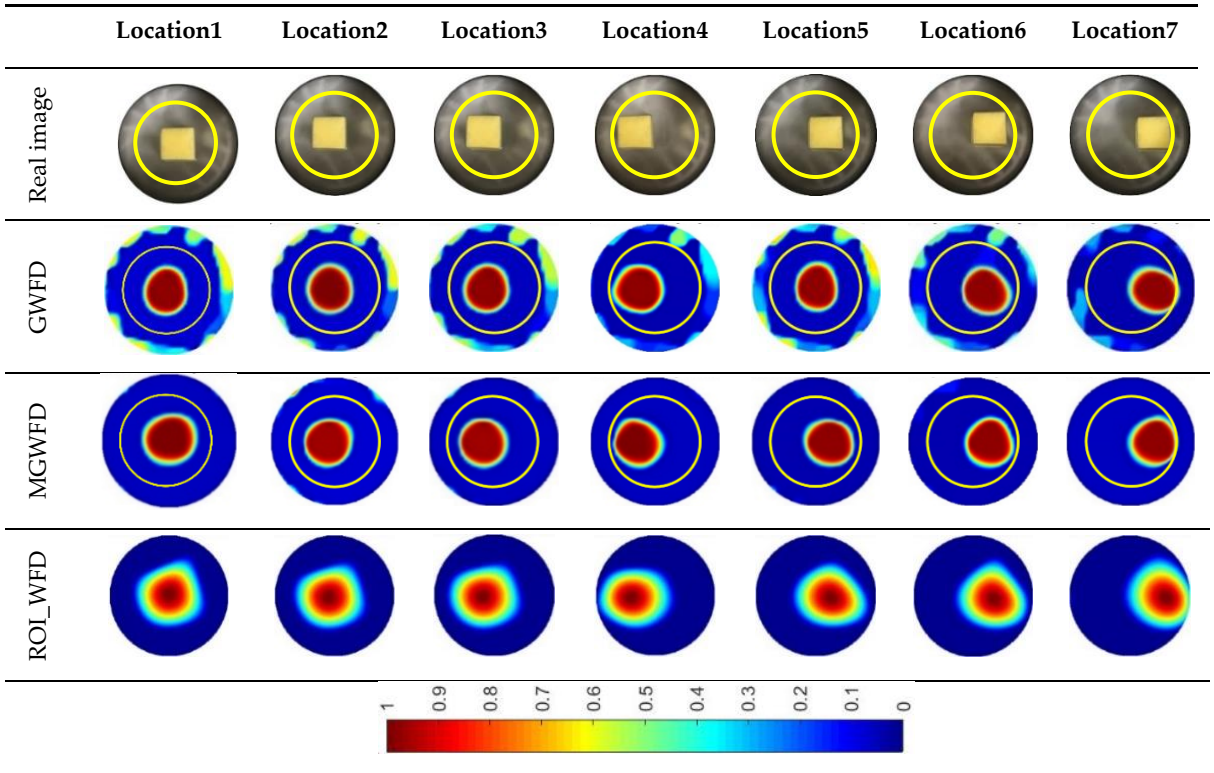

In Table 6.1, all three columns of reconstructed images manage to recover the real images. Yet, it is still worth noting that both MGWFD and ROI_WFD are able to remove the noise effect presented in GWFD.

Table 6.2 Theoretical model and reconstructions of medium sample

	Location1	Location2	Location3	Location4	Location5	Location6	Location7
Real image							
GWFD	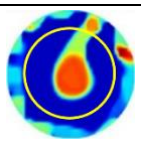	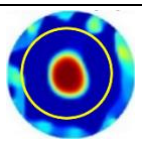	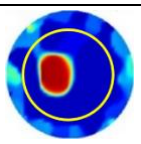	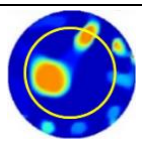	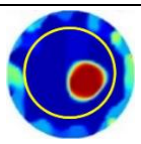	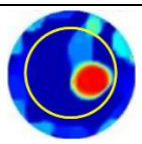	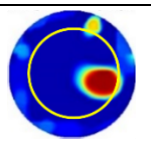
MGWFD	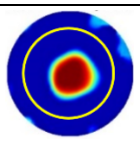	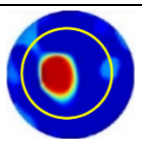	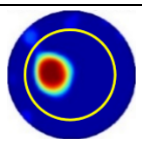	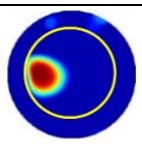	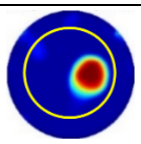	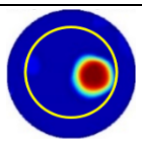	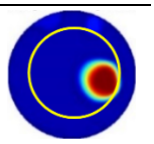
ROI_WFD	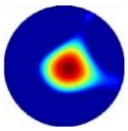	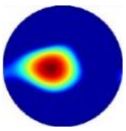	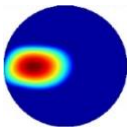	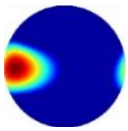	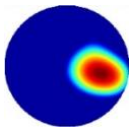	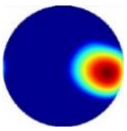	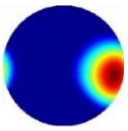
	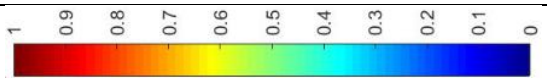						

In Table 6.2, a series of medium objects were tested and image reconstruction results are presented. When compared with the large sample case, a consistency of error existence in the left-top of the tank is seen in the GWFD reconstructed images. Again, a better image quality (in terms of getting rid of the background artefacts) was achieved by both MGWFD and ROI_WFD.

Table 6.3 theoretical model and reconstructions of Small sample

	Location1	Location2	Location3	Location4	Location5
Real image					
GWFD	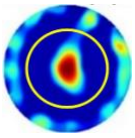	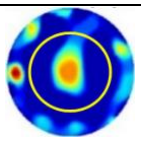	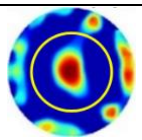	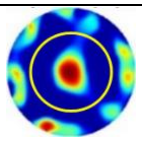	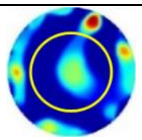
MGWFD	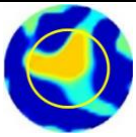	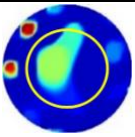	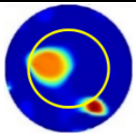	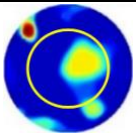	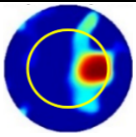
ROI_WFD	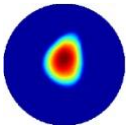	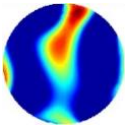	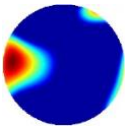	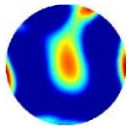	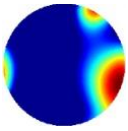
	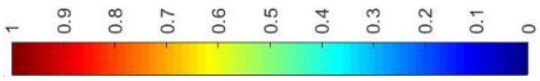				

The small object case unsurprisingly gives the worst image reconstructions as shown in Table 6.3. With the presence of noise, the signal is more prone to be contaminated. Moreover, facts that potato samples can absorb from background saline water by osmosis, the conductivity of potato samples can change as the experiments went along. Therefore, using the GWFD failed to track the movement of object. Even with a modified dataset, the inherent ill-posed nature of EIT still gives rise to difficulties on reconstructing images without the disturbance of the noise signal. Reconstruction using ROI_WFD also experiences a notable image distortion, but still shows a better location matching in comparison with GWFD. Further quantitative image quality analysis is required to justify the significance of ROI_WFD in the next section.

6.4. Analysis and Discussion

To further compare the results of the proposed methods with the other two, three evaluation parameters are selected in this section. Position error (PE), resolution (RES), together with relative error (RE) of

each reconstruction are plotted against different locations to evaluate images. Each image is firstly converted to 200×200 pixels and thresholded using equation **(3.51)**.

1. Position error (PE)

PE is preferably as small as possible so that the it can provide reliable results in locating the tumour; hence PE is of the most importance figure of merit in our case so that the confidence in tumour tracking applications can be assured.

Figure 6.1 plots the position error of three samples in centimetres against location variation.

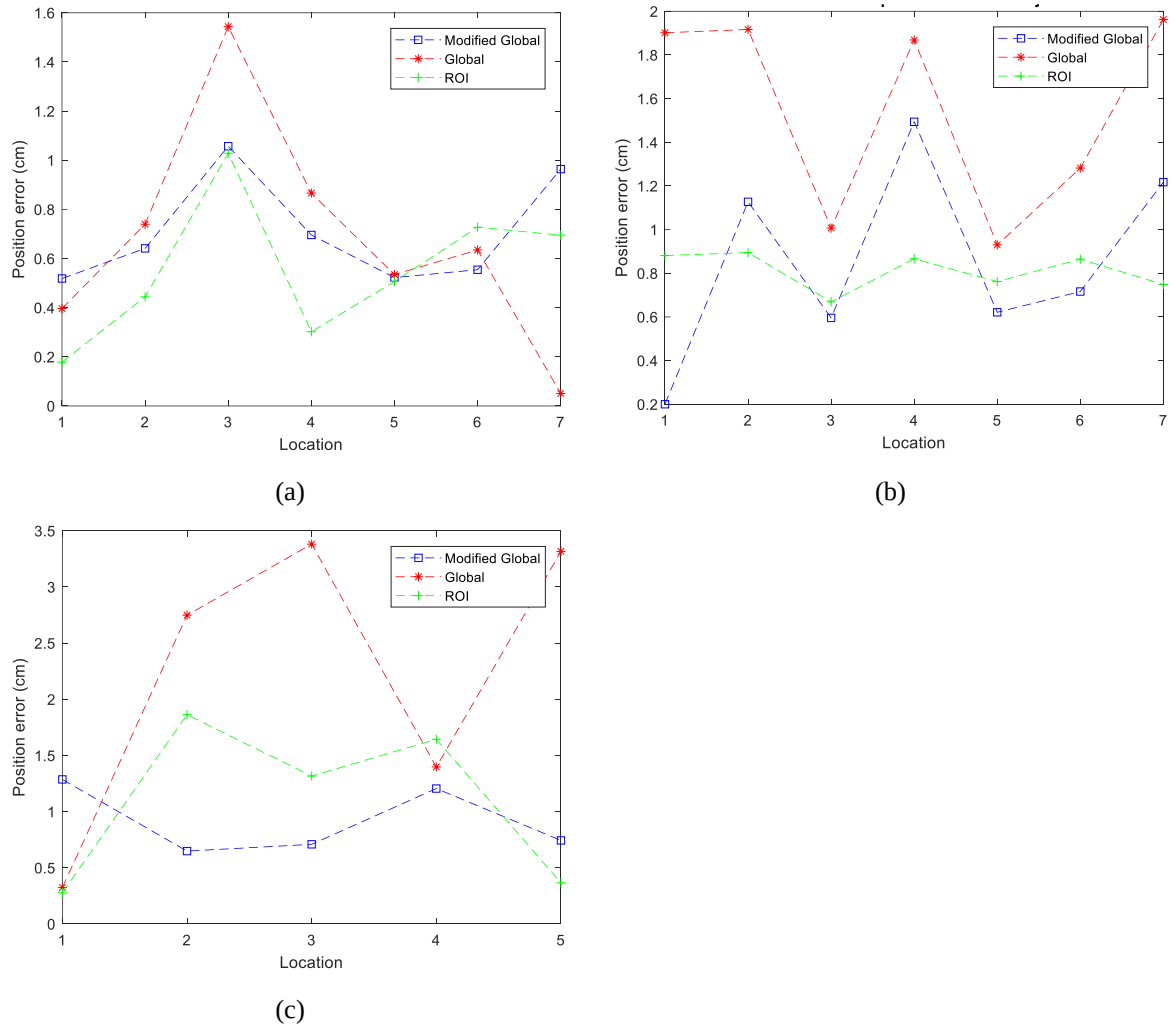

Figure 6.1 Position error plots of (a) Large object (b) Medium object (c) Small object

The position error plot of the large object does not suggest a notable improvement using the proposed method in comparison with the conventional method using both the modified and original datasets. This is due to the sufficient impedance contrast in large sample tests compared to the background noise that

has been introduced. Yet, as the size of the inclusion decreases, position errors tend to increase massively with all three protocols. Using ROI_WFD not only provides comparable results to a de-noised dataset, but also shows a better consistency of position displacements. This is advantageous as it provides the possibility of data calibration in practice.

2. Resolution (RES)

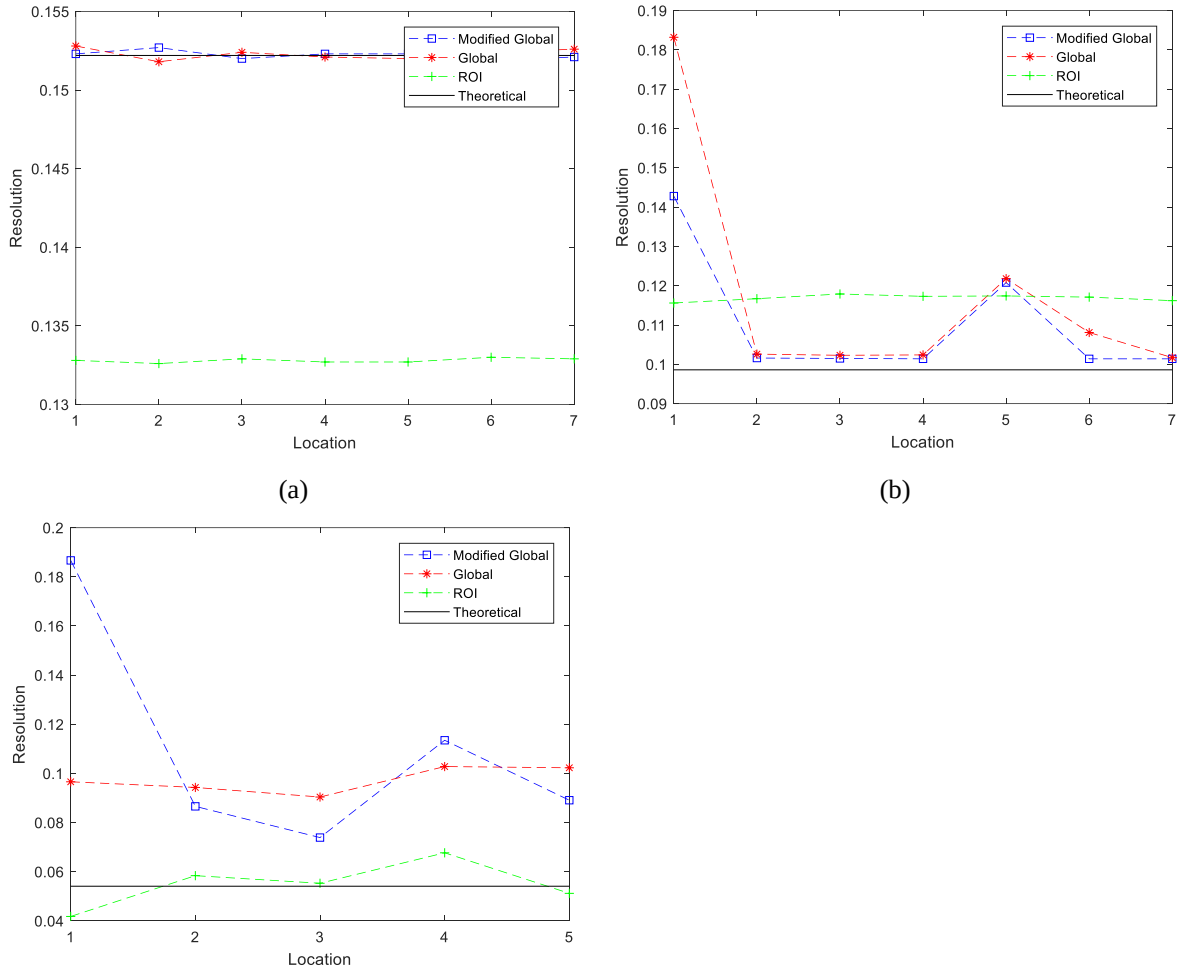

Figure 6.2 Resolution plots of (a) Large object (b) Medium object (c) Small object

Resolution plots of three objects at different locations are presented above in Figure 6.2. Theoretical resolutions calculated from the real image are also plotted in each figure as a reference. Evidently, reconstructions using ROI_WFD perform the best in terms of preserving the uniform resolution. Similar to position error plots, the advantages of using the proposed method become more significant as the object size gets smaller. Interestingly, ROI_WFD is even seen a degradation of matching with the

theoretical RES, which suggests that it will be particularly useful when the tumour size is at least smaller than 13% of the view region.

3. Relative Error (RE)

Figure 6.3 plots relative errors of large, medium and small objects against locations respectively.

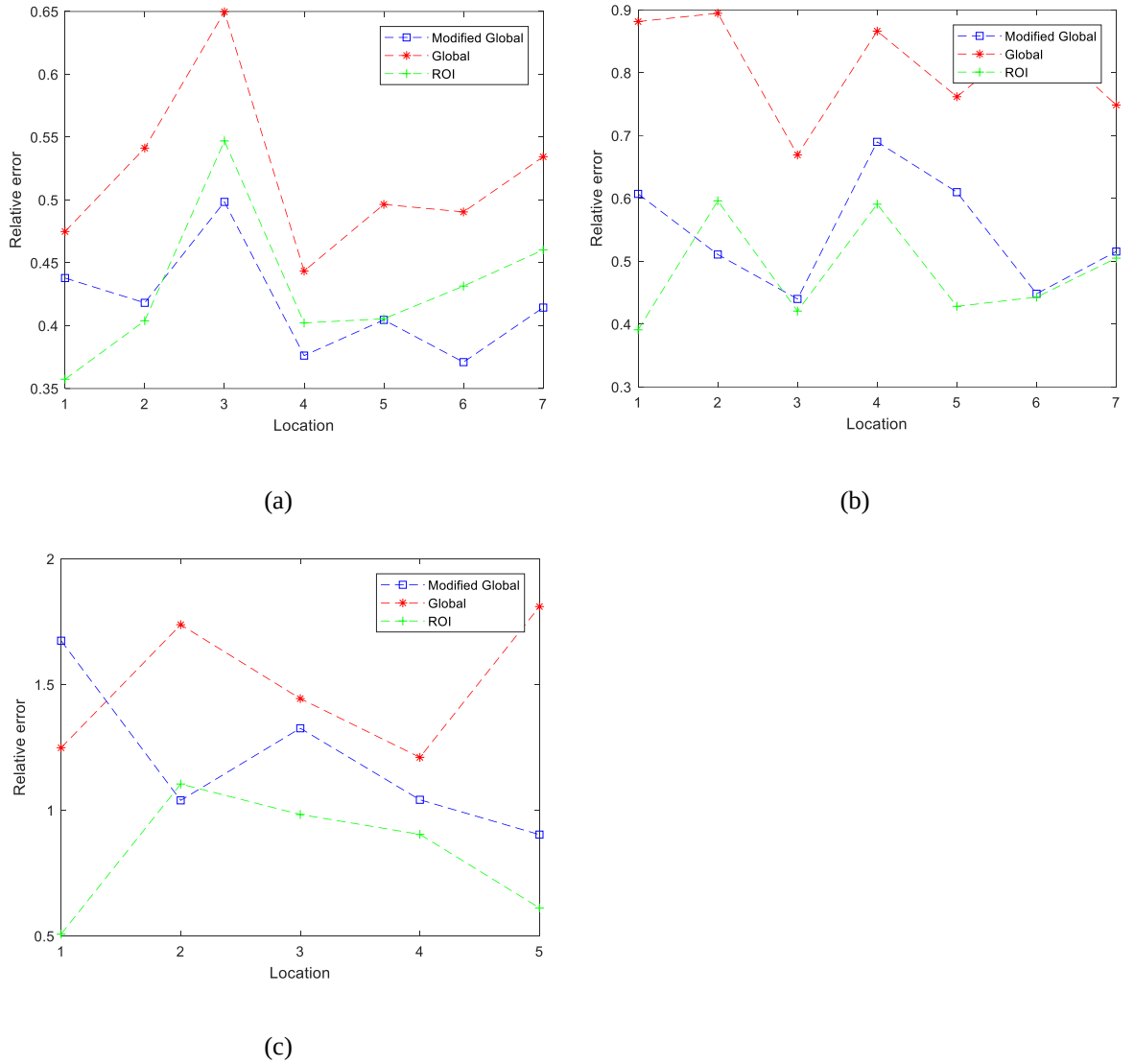

Figure 6.3 Relative Error of (a) large object (b) Medium object (c) Small object

An overall increase of relative error is suggested with the size of the inclusions decreasing. As a smaller object will yield a smaller impedance change and hence a weaker sensing signal, assuming the same amount of noise presented in the system, it will be more difficult to extract the information from the background noise. Among the three methods, ROI_WFD provides the best RE results in small inclusion tests and minimizes the background error to the similar extent as using the modified datasets, MGWFD.

6.5. Conclusion

EIT has been reported as a good monitoring/tracking tool working on its own or together with other conventional medical imaging systems, such as volumetric X-ray CT and PET due to its high temporal resolution. However, low spatial resolution of an EIT sytem can be a significant problem when the changes induced by the target movements do not dominate over the entire view region. In this work, a weighted frequency difference reconstruction within the region of interest is proposed and validated by two dimensional phantom experiments. This method offers EIT an opportunity of monitoring the targets movements even in a complicated setting.

To simulate the proposed application, bio-samples of different sizes were selected and placed at various locations within a pre-defined fraction of area in the phantom. Images were reconstructed using Split Bregman Total Variation regularization and the image quality was analysed by using position error, resolution and relative error. An improvement can then be confirmed by comparing the results from ROI_WDF to conventional GWFD as well as MGWFD, especially in the cases of tracking small samples. Moreover, the proposed method applies a filtering effect of noise as the results are comparable with MGWFD. This is particularly useful in the tumour tracking cases, where the background noises caused by contact impedance between electrodes and skin as well as other organs' movements are significant. These noises cannot be removed by MGWFD in practice due to the lack of background data whereas the proposed method, ROI_WDF, achieves the similar noises subtraction effect, and hence can be introduced into such applications.

With the confidence obtained from both 2-D simulation and experiment results, it can be concluded that the limited region method can bring in the system enhancement. Therefore, this limited region based EIT with frequency difference imaging could potentially be considered as a universal monitoring tool when the view region is rather complex and undergoing notable changes. The clinical value of the proposed localized EIT system is that it could create potential for motion compensation data for PET and CT. Moreover, it can extend to tracking tumours during radiation therapy making an adaptive radiation therapy possible. The proposed method can also make EIT a good candidate in comfortably

measuring and detecting deposition or blockages within complicated sewer flows, especially when the solids mostly are composed of organic matters.

The conductivity contrast of the same object under different stimulation frequencies is normally smaller than that between the object and the background; therefore, the localized method can also be applied in traditional time-difference EIT problems to enhance the overall system immunity to noises. Therefore, the robustness offered by limitted region EIT method proposed in this chapter is followed in an interesting application in following chapter where we deal with a challenging problem of limited data EIT in part full pipes.

Chapter 7 Part full pipe flow imaging

ERT has been studied extensively for visualizing and understanding the flow behaviour of process flow and thus can be a good candidate in supervising the sewer flow. A low cost ERT device has been developed dedicating to monitoring flow in the sewerage systems in Chapter 4. The preliminary study of the proposed design, which was conducted under the lab-scale setup, has demonstrated its capability of detecting obstacles as well as dynamical movements. In the free flowing sewerage system pipes should be partially filled, however, this will lead to several sensing electrodes losing contact with the flow. Consequently, we need the ERT system to be able to handle such part full pipe situations. In this chapter, we will further develop the ERT system in both hardware and software perspectives so that it could fulfill the functionalities in all flow scenarios. Essentially, the hardware modification allows for detecting the out-of-contact electrodes and eliminating the erroneous measurements. The limited region computation method, which is adopted from Chapter 6, mitigates the reconstruction problems resulted from the incomplete datasets. Both simulation and experimental results have shown an enhanced performance brought by the limited region method in comprison with the global reconstruction.

7.1. Introduction

ERT has been developed extensively for visualizing and understanding the concentration distribution and flow behavior within a process instrument [163]. It involves the measurement of the independent mutual impedance between electrode pairs and the reconstruction of cross-sectional images using measured data and suitable algorithm. A conventional ERT system consists of a set of electrodes evenly mounted around the periphery of the object. Mutual impedance is obtained by injecting currents from one pair of electrodes and taking voltage measurements from another pair of electrodes. Typically, ERT sensors are dominantly applied to aqueous-based fluids that possess continuous admittance; hence they are suitable for wastewater flow applications as the operating conditions for fluid conductivity are regulated as 50 to 1200 μS cm−1 [64]. ERT systems offer high temporal speed and the ability of visualization of multiphase flow. Therefore, they outperform other traditional non-tomographic

flowmeters, e.g., ultrasonic Doppler velocity profilers, electromagnetic meters, Coriolis mass meters, and Venturi meters, and become good candidates for monitoring and analyzing sewage flow behaviors.

In [164], it was advised that foul sewers and lateral drains should be designed to run at no more than 75% of pipe full conditions. In other words, in the free-flowing sewers, the pipes are mostly part full. In such cases, the electrodes above the liquid surface will lose their electrical contact with the sensing field, which causes a great phase-shift in response potentials on these electrodes. Since the data acquisition system (DAQ) of the ERT system neglects the phase shifts among all measurements, voltage data on these electrodes cannot reflect the true conductivity distribution. To address this problem, [165] developed a novel sensor design which uses a single conductive ring to replace the discrete electrodes to guarantee a continuous current excitation. However, the performance of the design relies on the fluid conductivity and thickness ratios; hence, in the case of sewage flow monitoring, where a large conductivity variation could exist, the reconstruction quality would decay. Reconstruction methods have been focused on extracting the conductive phase surface. For instance, [166] proposed a liquid level detection method that directly analyses raw voltage measurements collected from a conventional ERT hardware system to estimate the liquid levels; [167] estimated the free-surface in two-phase flow by using the boundary element method to formulate the forward problem and the iterative Levenberg–Marquardt method for inverse problem. However, these methods can only provide the information on water surface levels as suggested, but fail to visualize within the flow. [168] proposed two methods based on the valid dataset and the new sensitivity field to reconstruct the stratified flow in a traditional ERT system. Firstly, the electrodes that are above the liquid level are identified and any measurements that involve these electrodes are eliminated from the dataset. The remaining valid dataset is used for image reconstruction. However, this incomplete set of data will worsen the ill-posed nature of ERT as fewer measurements are available for the reconstruction. Previous studies have investigated the ERT reconstruction methods for solving the partial data and limited angle problems [70]. However, the problem assessed previously considered the energy distribution over the entire continuous domain caused by an electric current injection through a partially accessible boundary. However, the part full pipe problems essentially divide the domains into two subsets, as the electric currents cannot propagate

beyond the conductive phase. [168] took advantage of such prior knowledge of the region where the continuous phase exists and proposed the limited region reconstruction method by reformulating the sensitivity matrix. The simulation results were presented to compare the reconstruction within the localized region with only using the valid dataset. The advancement of such reconstruction method has also been proven experimentally in [14], however, with a better prior knowledge of location in the medical application.

In this chapter, we will further develop the ERT device designed in [12] so that it could accommodate for incomplete data application at low cost; and a comprehensive study of the advantages brought by Jacobian matrix reformulation will be quantitatively investigated using both numerical simulations and stationary phantom experiments. Inclusions of different sizes will be added into the continuous phase at various locations. Position error (PE), amplitude response (AR), shape deformation (SD) [126], as well as correlation coefficient (CC), relative error (RE) and computation time will be compared to justify the advantages brought by applying the localised method.

7.2. Modified ERT Hardware

The high temporal and low spatial resolution nature of ERT offer an opportunity to capture the flow profile in sewer systems. In [169], a 16-channel ERT device was designed for wastewater flow monitoring applications, as shown in Figure 7.1(a). The reported 14 frames/second data acquisition speed and the smallest detectable size being 0.04% of the phantom area allow for a successful motion tracking practice. Additionally, the compact design, which was prototyped at 14 × 7 × 6 cm, and the cost effectiveness make it preferable for mass deployment in the sewer network, and hence facilitate maintenance and minimize disruptions to the networks.

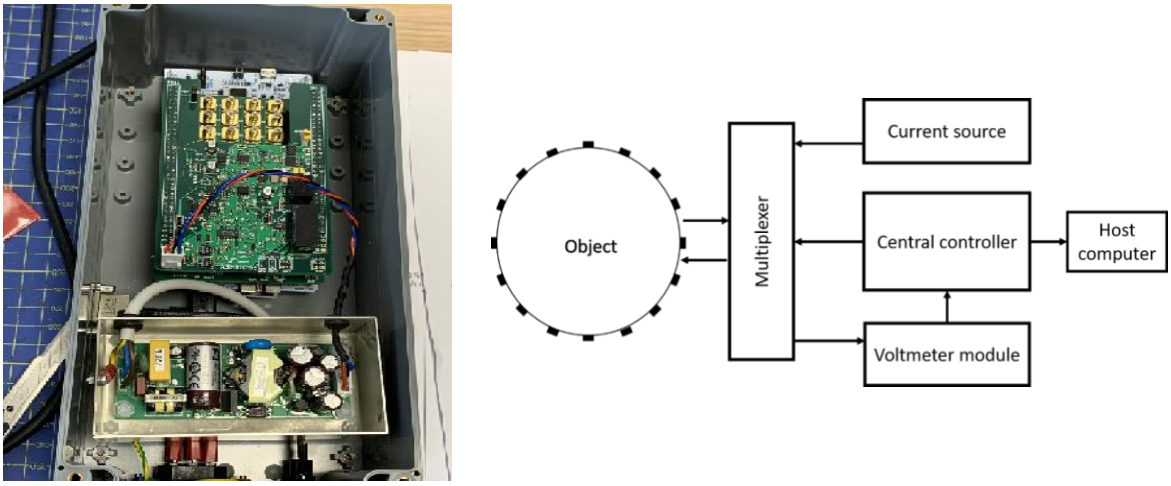

(**a**) (**b**)

Figure 7.1 (a) 16-channel ERT device designed in [170] (b) ERT system overview.

Figure 7.1(b) presents an overview of the 16-channel ERT system architecture. It operates at 50 kHz and uses the adjacent driving and measuring mechanism, which produces an overall 208 measurements per frame, with a user configurable current injection over the range of 6 to 18 mA. Since the ERT technique only concerns the in-phase response, a peak detector was introduced in the system for capturing the in-phase component. Consequently, the phase shifts caused by the discontinuous phase is then ignored.

7.2.1.Current Sensing Module

Since the traditional current-injecting-voltage-sensing mechanism has difficulty producing accurate measurements when the electrodes involved are present in the air, these data points will have to be eliminated from the dataset. To obtain the knowledge of the electrodes that are not submerged in the liquid, a current sensing module, as illustrated in Figure 7.2, is therefore added to the previous ERT hardware. Specifically, a current sensing resistor is included in the return loop of the current-stimulation circuit such that the current flowing through it in the form of a voltage drop is fed into the controller; hence the open circuit formed by any electrode of the injecting/receiving electrode pair that is exposed in the air will be acknowledged by proper thresholding. Here, 500 instead of 0 was chosen in the reception module, which includes a 12-bit Analogue to Digital Converter to account for any voltage drop across the resistance over transmission. Once the non-contact electrodes are determined, the non-

contact electrode numbers will be sent together with the measurements to the host PC. Subsequently, the data post-processing will allow the measurements taken from any of these electrodes to be automatically eliminated from one frame of data. Such current sensing module can indicate any electrodes that cannot allow for the required amount of currents to flow through, and this may include those that are not in good contact with the interior fluid. This is especially useful since in these cases the measurements can also be erronoues and cannot contribute to the image reconstructions.

The current sensing module will be validated in the simulated stable stratified flows in the lab tests in 7.4. However, when the device is working in the turbulant flows where the fluid undergoes irregular fluctuations, the chances are there are a couple of electrodes encountering on and off contact with the fluid. The transmission mechanism is designed to incorporate such situations by including the non-contact electrode numbers into every frame of measurements. Therefore, the image reconstruction will be adjusted accordingly.

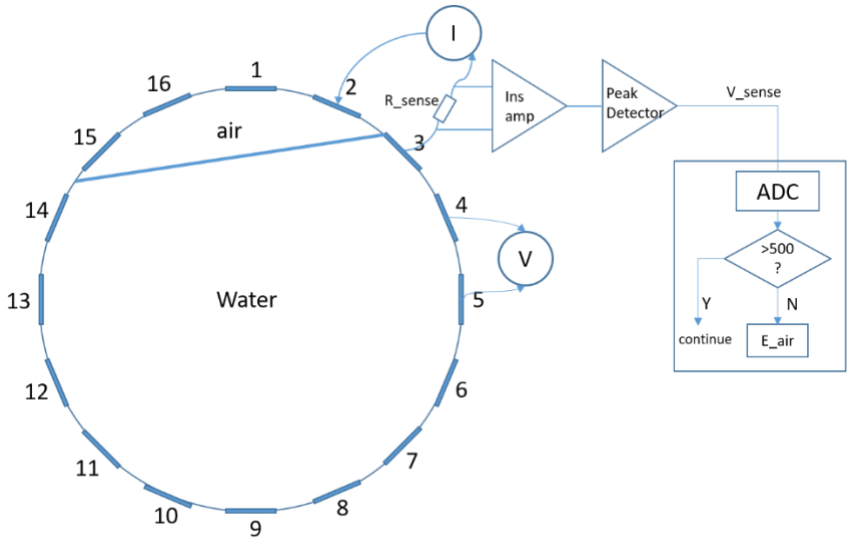

Figure 7.2 Current sensing module.

7.2.2.Incomplete Dataset Model

In our 16-channel ERT device, with all electrodes being capable of providing informative measurements, there are $N_M = N \times (N - 3)$ independent measurements, where N is the channel number of the ERT device. In the stratified flow applications, some electrodes will lose contact with the

continuous phase, as illustrated in Figure 7.3, and thus fail to provide valid measurements to the reconstruction, in which case the dataset is incomplete. The number of independent measurements available in such system now drop to $N_M = (N_v - 2)(N_v - 3)/2$, where N_v is the number of valid electrodes and $N_v < N$.

The ERT image reconstruction problem is known as being ill-posed, as the problem is formulated using an ill-conditioned sensitivity (Jacobian) matrix. The singular value decomposition analysis of the Jacobian matrix can be introduced to evaluate the degree-of-ill-posedness of such problems [169]. According to the Picard condition, the number of singular values above the noise level of the measurements represents the amount of information that can be extracted. Evidently, the decrease in the available independent measurements makes the singular values decay much faster and therefore fewer singular values will carry relevant information in the noisy case.

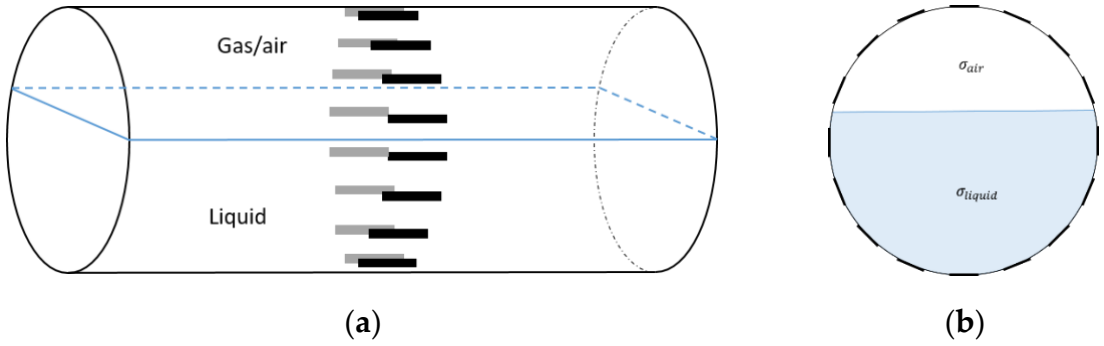

Figure 7.3 Gas-liquid ERT system model: (a) gas-liquid stratified flow in a horizontal pipe; (b) cross-sectional distribution of ERT system.

7.3. ERT Reconstruction method

For stable and fast image reconstruction, a linearized inverse problem is solved using traditional L2-norm regularizing penalty term, e.g., the Tikhonov regularization method. The system is based on time difference imaging, which means it reconstructs the changes in electrical conductivities $\Delta\sigma$ from the differential voltages Δu obtained at time t_1 and t_2. Here, we consider the two sets of measurements u_i and u_b as the measurements taken before and after the insertion of inclusions. Accordingly, the inverse problem can be solved following Equation (3.39). This chapter presents cases for static imaging mode, in dynamical imaging mode temporal based algorithms could be adapted [171].

- *Limited region method*

The conventional algorithm reconstructs images over the entire domain without emphasis on the information in the region of interest (ROI). The inherent problem that an ERT system suffers is linked with the ill-conditioned sensitivity matrix. The incomplete datasets generated from partially-filled phantoms further increase the condition number and can result in the even more significant numerical errors in the reconstructed images. A strategy of using the valid measurements to reconstruct images restricted to a pre-defined ROI was introduced in Chapter 6 and is now adopted. Essentially, only the conductivity changes within the continuous phase is concerned, since the electromagnetic waves are not able to propagate into the non-conductive phase. Therefore, the ROI should be chosen equivalent to the conductive area as closely as possible. Given the gap existing between two adjacent electrodes and the uncertainty of the exact liquid level, the ROI boundary is defined as the lowest level of the invalid electrodes to ensure the coverage of all the potential conductivity changes under the water as demonstrated in Figure 7.4.

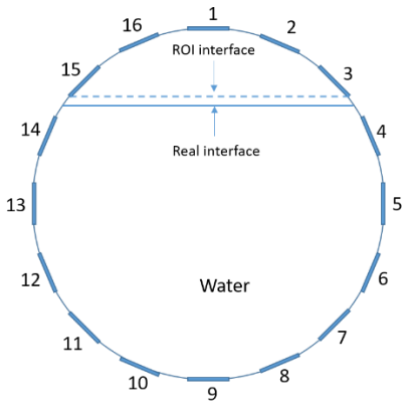

Figure 7.4 Region of interest (ROI) definition in a partially filled pipe.

The principal of limited region reconstruction is restricting the process to the ROI defined by the water level estimator. Therefore, the original domain Ω can be divided into two areas: one is the continuous phase area, denoted as $\Omega_{liquid} \subseteq \Omega$, where conductivity changes will be picked up in the voltage measurements (also known as the ROI); the other is the discontinuous phase area that theoretically $\sigma_{air} = 0$. Then, the conductivity changes Δσ can be mapped to

$$\Delta\sigma = \begin{cases} \Delta\sigma_{\text{liquid}}, & x \in \Omega_{\text{liquid}} \\ 0, & x \in \Omega \backslash \Omega_{\text{liquid}} \end{cases} \quad \textbf{(7.1)}$$

Now the limited region reconstruction equation can be derived as:

$$\Delta V = J_{x \in \Omega_{liquid}} \Delta\sigma_{liquid} \quad \textbf{(7.2)}$$

where ΔV is the difference boundary measurements, $J_{x \in \Omega_{liquid}}$ is the reformulated Jacobian matrix. Here we have identified the conductivity changes with their finite elements approximations.

By limiting the imaging area, which consequently reduces the number of unknown pixels, we could enhance the system robustness when the same amount of accessible measurements are used. Other than a better accuracy, a faster computation can also be achieved using the limited region method when compared with the global reconstruction due to the reduction in the number of pixels involved in the imaging process.

7.4. Results and Analysis

7.4.1. Simulation Study

In this section, a series of numerical simulations were performed on a unit domain $\Omega = \{(x,y): x^2 + y^2 < 1\}$ with 16 electrodes equally spaced around its circumference. We set the region $\Omega_1 = \{(x,y): y < \text{Level}\}$ represent the continuous (liquid) phase, where *Level* serves as the interface between the liquid and gas phases; and the conductivity value of region Ω_1 is 1. As for the conductivity value of region $\Omega_1 \backslash \Omega$, which is to simulate the gas phase, should theoretically be 0 Sm^{-1}; but this will lead to stimulation currents unable to be injected into the system and hence the simulation failure. Consequently, we set it to 1×10^{-4} Sm^{-1}, which is small enough to be distinguished from the liquid phase [87].

In the single inclusion simulation tests, we created three different scenarios:

1. Case1: Level = 0.5 and we apply an anomaly $\Omega_2 = 0.1$ to region D1 = $\{(x,y): x^2 + (y + 0.2)^2 < 0.04\}$;
2. Case2: Level = 0.2 and we apply an anomaly $\Omega_2 = 0.1$ to region D2 = $\{(x,y): x^2 + (y + 0.4)^2 < 0.04\}$.
3. Case3: Level = -0.2 and we apply an anomaly $\Omega_2 = 0.1$ to region D3 = $\{(x,y): x^2 + (y + 0.6)^2 < 0.04\}$.

The forward problem is numerically solved using a MATLAB toolkit, i.e., EIDORS [170], to generate simulated boundary measurements, v_i and v_h, and we added randomly generated 12 dB Gaussian noise to the simulated data. The reconstructions using global and limited region methods were then compared in Table 7.1. The apparent improvements of image qualities are seen especially with the existence of noise in the localized images, which justify the benefits of using such method. It is worth pointing out that in Case 3, where only seven electrodes are simulated submerged in the water, we would expect the worst image quality among these three scenarios. However, due to the space limitation, the anomaly can only be placed very close to the boundary; hence, recovering images using the limited region method in particular did not experience more difficulty than the other two cases. This is the major difference between the problem arising from part full pipe flow and the general incomplete data problems. Accordingly, water levels were only advised to decrease to half full in the following phantom experiments for a better justification of applying the proposed methods at various locations.

Table 7.1 Single inclusion simulation results.

	Case 1		**Case 2**		**Case 3**	
	Without Noise	**With 12 dB Noise**	**Without Noise**	**With 12 dB Noise**	**Without Noise**	**With 12 dB Noise**
Localized	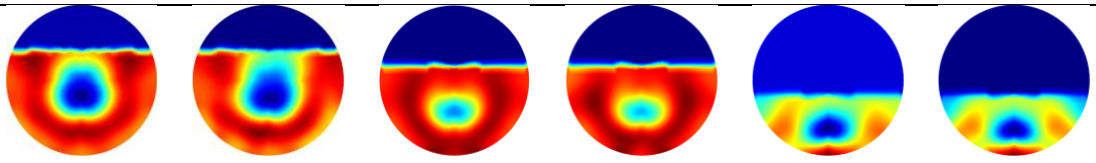					
Global	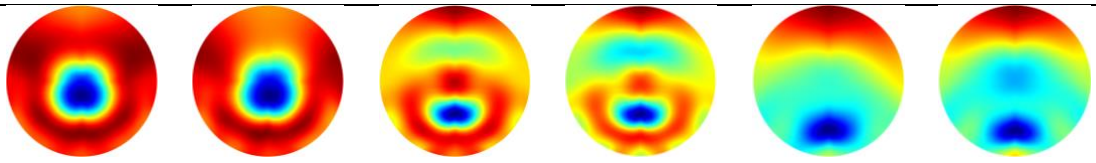					

Real	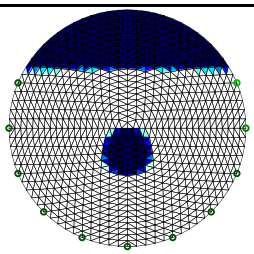	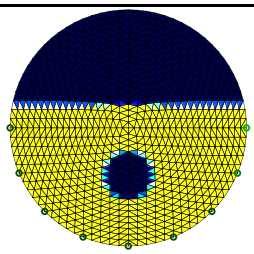	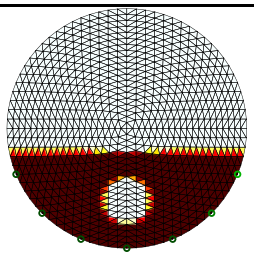

In the multiple inclusion simulation model, two anomalies of $\Omega_d = 0.1$ were defined by D within the unit domain under the two liquid levels:

$$D = \{(x_1,y_1): (x_1 + 0.4)^2 + (y_1 + 0.6)^2 < 0.01; (x_2,y_2): (x_2 - 0.4)^2 + (y_2 + 0.6)^2 < 0.01\}$$

$$\text{Level } 1 = 0;$$

$$\text{Level } 2 = -0.38$$

Again, 12 dB Gaussian noise was added to the simulated boundary measurements as shown in Table 7.2. Naturally, the reconstructions involving multiple inclusions are more challenging than the single inclusion problems due to the increased complexity. The lack of measurements makes it even more difficult to solve the inverse problems particularly with the disturbance of added noises. The localised images give improved results with a better reveal of objects, whereas those of the global images are rather distorted, especially in the Level 2 simulation.

Table 7.2 Multiple inclusion simulation results.

Level 1			**Level 2**		
Real Distribution		**Image**	**Real Distribution**		**Image**
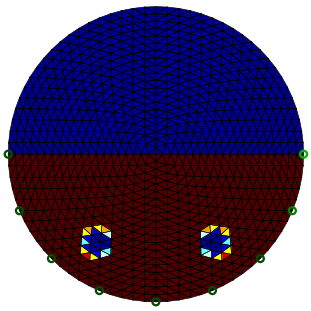	**Localised**	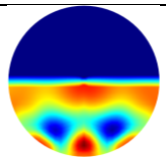	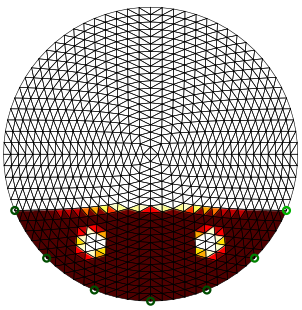	**Localised**	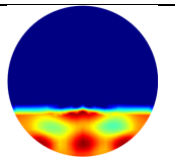
	Global	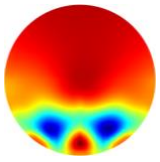		**Global**	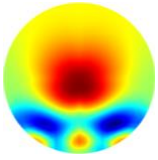

7.4.2. Experimental study

7.4.2.1. Experiment Set up

In this section, feasibility studies were carried out experimentally considering only 2-dimensional models. Phantom experiments were established in a horizontally placed 11 cm diameter cylindrical tank with 16 electrodes of 1.2 × 1 cm size equally spaced stainless-steel electrodes shown in Figure 7.5. The modified ERT device was used to collect measurements under the stimulation currents of 10 mA.

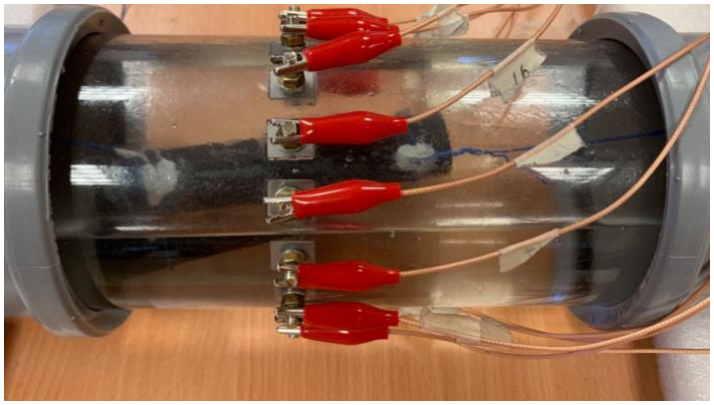

Figure 7.5 Phantom set up.

7.4.2.2. Reconstructions Based on Valid Datasets

As discussed previously, the existence of electrodes not in contact with conductive medium would introduce errors into the conventional ERT system. We established a current sensing module to locate the erroneous electrodes and eliminate the incorrect measurements accordingly. In this section, the necessity of identifying the valid datasets for reconstructions in the cases of part full pipe applications is justified by comparing images of inclusions recovered from the valid against those from the full datasets.

Experiments were conducted by collecting the background datasets with the tank full and second datasets after inserting a small and medium inclusion under five different liquid levels, as shown in Table 7.3 and 7.4. The real distributions of the phantoms are also provided for reference.

Evidently, with no knowledge of erroneous measurements, the inaccurate measurements can seriously distort the images, especially in the small inclusion tests. On the other hand, the valid datasets managed to recover both the gas void and the inclusion in all tests.

Table 7.3 Small inclusion tests comparison.

	Level 1	Level 2	Level 3	Level 4	Level 5
Real	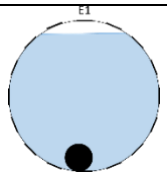	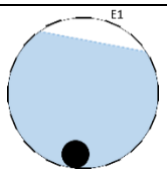	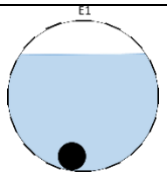	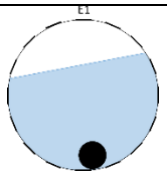	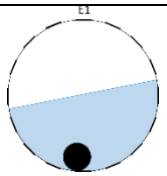
Full Dataset	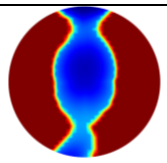	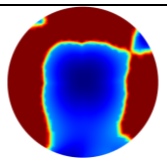	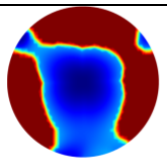	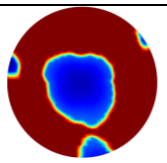	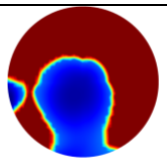
Valid Dataset	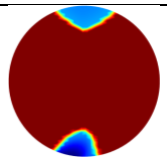	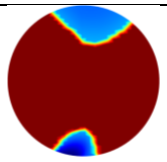	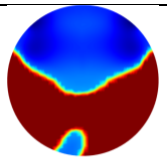	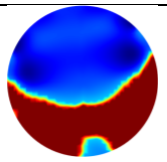	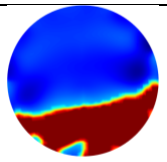

Table 7.4 Medium inclusion test comparison.

	Level 1	Level 2	Level 3	Level 4	Level 5
Real	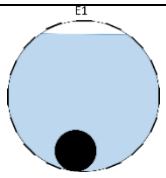	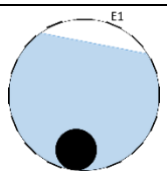	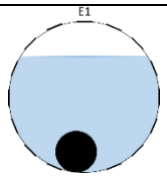	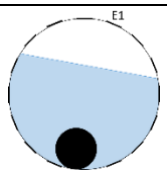	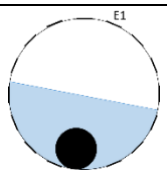
Full Dataset	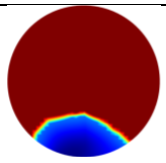	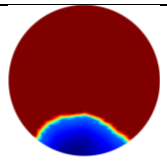	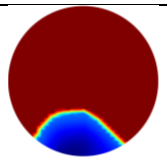	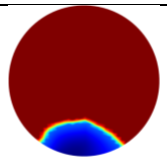	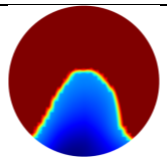
Valid Dataset	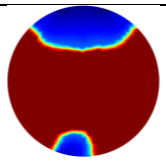	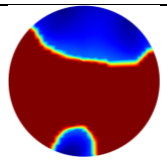	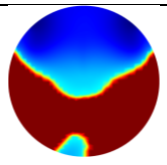	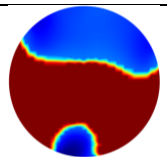	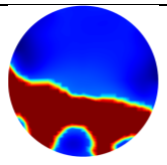

7.4.2.3. Investigation on Limited Region Method

With the confidence of reconstructions using incomplete datasets, a further investigation on the advantages of applying prior knowledge of the conductive phase area will be discussed in this section.

Three different water levels were considered in both single and multiple inclusion tests:

- *Level 1: Electrodes 4–14 are submerged in the water;*
- *Level 2: Electrodes 5–13 are submerged in the water;*
- *Level 3: Electrodes 5–12 are submerged in the water,*

where the electrode numbering is referred to in Figure 7.4.

As suggested previously, sewers are advised to run at part full conditions under normal operation; thus the full tank data are mostly inaccessible. To model such circumstances, we conducted the experiments using datasets taken before and after the insertion of the anomalies in the part full pipes. The influence of liquid level increase caused by the insertions was also ignored to simplify the problem and focus on recovering targets within the conductive phase. That is to say, the liquid level is kept the same for both before and after adding the inclusions to make sure conductivity changes are entirely generated by the addition of targets. Reconstructions were completed and compared between the global method and the limited region method.

- *Single inclusion test*

In all cases, small (2 cm diameter) and medium (3 cm diameter) plastic rods were placed at various locations under the water within the pipe.

The reconstructed images of two objects using the global and localised methods (ROI) are presented in comparison to the real distribution within the phantom in Table 7.5-Table 7.7. As previously explained, the purpose of this work is to reconstruct the changes within the conductive phase rather than finding the interface between the liquid and gas phases. The distinct boundaries in the localised reconstructed images, i.e., in ROI columns, are used to mark the ROI area, above which the conductivity changes were set to zero.

Table 7.5 Reconstructed images of small and medium objects in Level 1 tests.

	Small			Medium		
	Real	Global	ROI	Real	Global	ROI
P 1	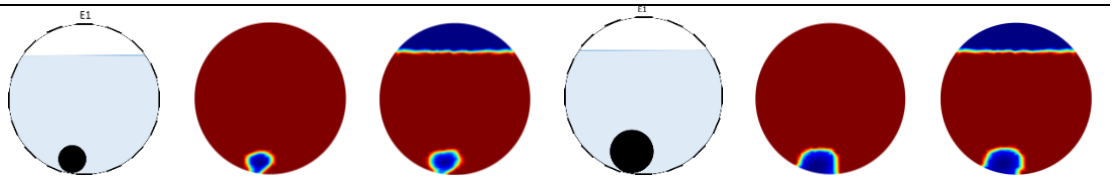					
P 2	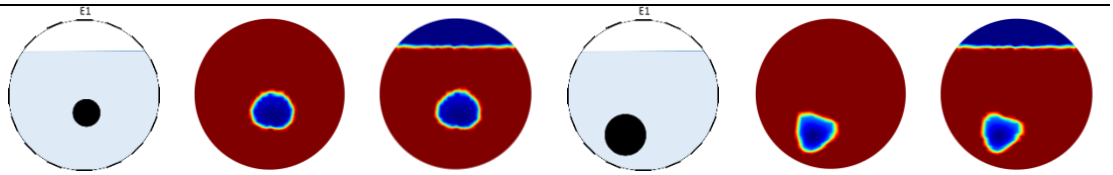					
P 3	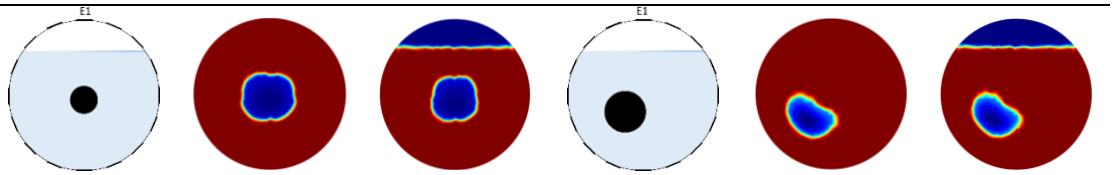					

Table 7.6 Reconstructed images of small and medium objects in Level 2 tests.

	Small			Medium		
	Real	Global	ROI	Real	Global	ROI
P 1	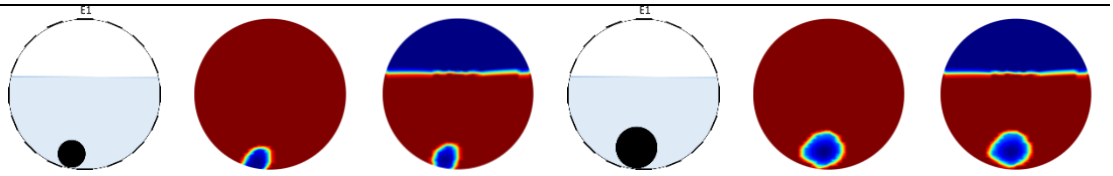					
P 2	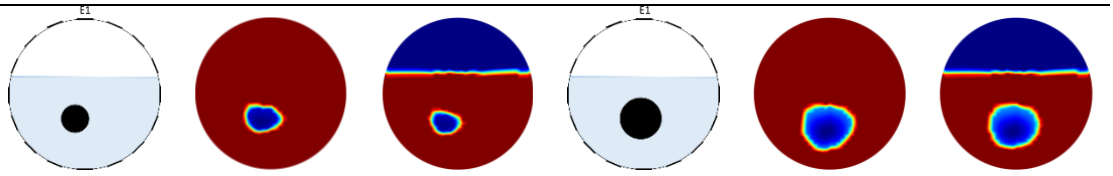					
P 3	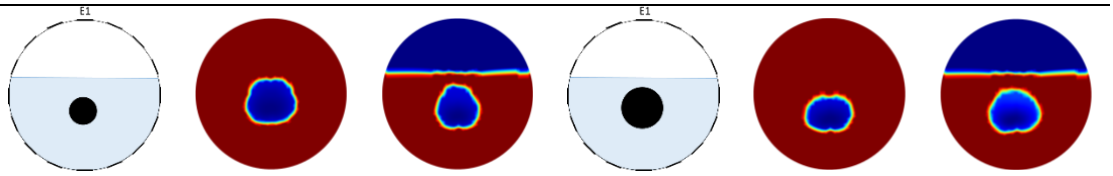					

Table 7.7 Reconstructed images of small and medium objects in Level 3 tests.

	Small			Medium		
	Real	Global	ROI	Real	Global	ROI
P 1	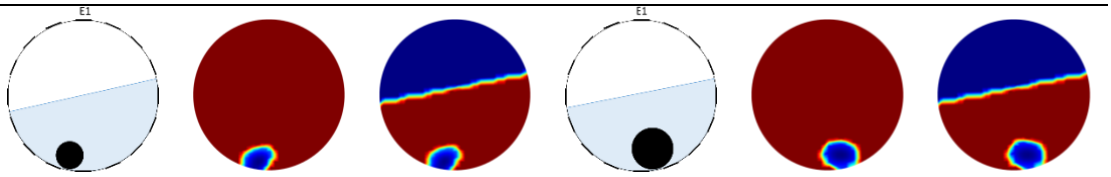					
P 2	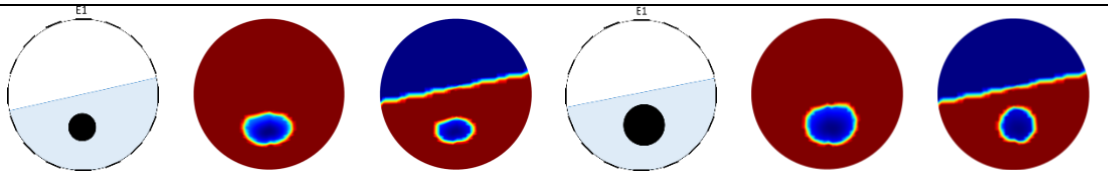					
P 3	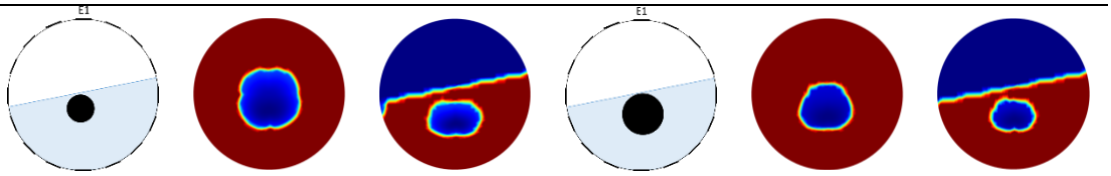					

In Table 7.5, the ROI images do not show an obvious improvement in image quality as the water level is relatively high and not much information is missing due to the exclusion of erroneous measurements. However, a notably better shape preservation of objects can be observed from the ROI images in Tables Table 7.6 and Table 7.7 as opposed to the global images. Additionally, as the objects move from the edge (P1) to the centre (P3) of the pipe in each table, both reconstruction methods tend to generate severely distorted images. Yet, with the global images in P3 rows of Table 7.7 inaccurately spread beyond the conductive area, which would massively mislead the information processing, the ROI method brings the robustness by reliably localising the objects.

- *Multiple inclusion test*

Another set of tests were carried out with more than one sample in the tank and the results are presented in Table 7.8. As the small object tends to generate low amplitude responses, we placed the small object closer to the boundary of the phantom to simplify the problem. As stated before, when the water level is sufficiently high, which is Level 1 in our case, applying the localised method does not make an impressive difference to the image qualities. This can also be confirmed in the multiple sample test in the Level 1 row of Table 7.8. It is also notable that in the Level 1 simulation, both global and ROI

methods struggled to separate these two inclusions. This is due to the fact that one inclusion is placed next to the boundary whereas the other is closer to the centre. Nevertheless, the better distinguishability of two objects brought by ROI method can be noted in the Level 3 test.

Table 7.8 Reconstructed images of multiple samples using global and ROI methods.

	Real	Global	ROI
Level1	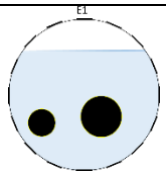	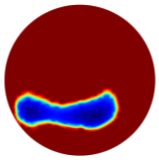	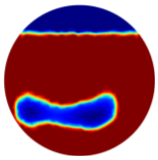
Level2	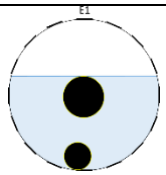	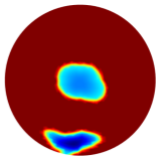	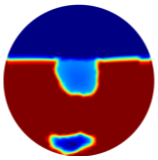
Level 3	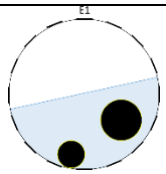	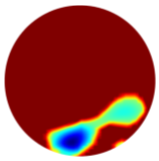	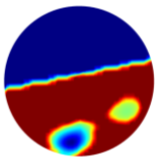

7.4.2.4. *Image Analysis of Single Inclusion Experiments*

To further quantitatively analyse the effect of applying limited region method in the single inclusion tests, four evaluation parameters were introduced. Due to the complexity of the images and image reconstructions involved in ERT problems, we introduced two sets of evaluation parameters to make a comprehensive inspection. Firstly, we adopted three figures of merits defined in [126], which focus on the quality of targets, namely position error (PE), shape deformation (SD), and amplitude response (AR). The significance of these parameters in the wastewater flow applications were discussed in [164]. Secondly, three additional parameters were introduced to make judgements on the overall performance of reconstructions, including the correlation coefficient (CC), relative error (RE), and computational time (CT).

Each reconstructed image is comprised of 50 × 50 pixels and for a better accuracy of the evaluation parameters, images are resized to 200 × 200 pixels and can be represented by a column vector $\hat{x}$. In the

reconstructed images $\hat{x}_q$, a threshold of one-fourth of the maximum amplitude is applied, which detects most of the visually significant effects:

1. Position error

In Figure 7.6, the position errors of using two methods are plotted against various locations in all three level cases. The PE plot of the medium object at Location 1 in Figure 7.6(a) does not suggest a significant improvement by using the localised method. As the liquid level goes down and the objects are placed further away from the boundary, PEs see a notable increase with all reconstruction mechanisms. However, applying the localised algorithm manages to lower the PEs for both small and medium objects when compared with the images reconstructed using traditional global method.

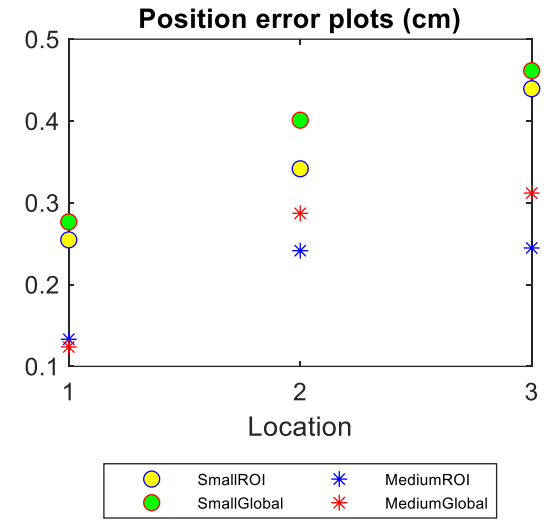

(**a**)

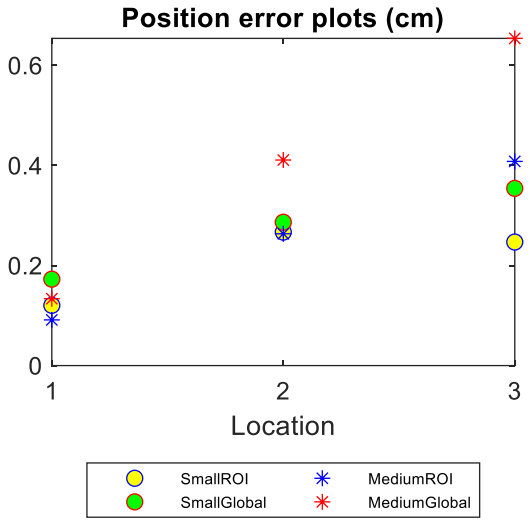

(**b**)

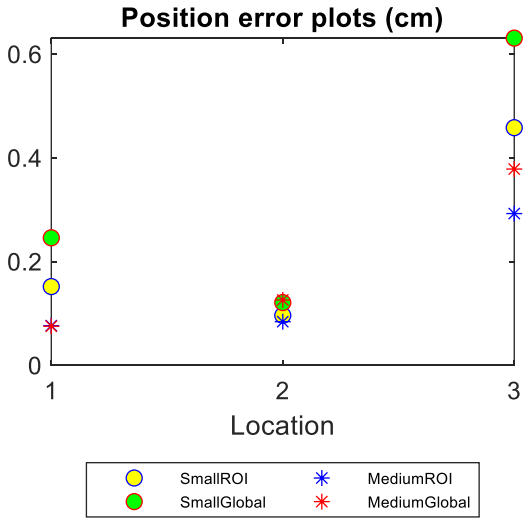

(c)

Figure 7.6 Position errors (PE) of small and medium objects inserted into the pipe filled up to three water levels: (a) Level 1 (b) Level 2 (c) Level 3.

2. Shape deformation

The shape deformation is compared between the global and limited region methods in Figure 7.6. An increase in SD for both methods is seen as the objects get further away from the boundary, which again confirms the reconstruction difficulty due to the ill-posed nature of ERT problems. The lower value of SD produced by the ROI reconstruction, especially in the cases of lower water level cases (in Figure 7.7(b), (c)), however, can confirm a better preservation of using such method.

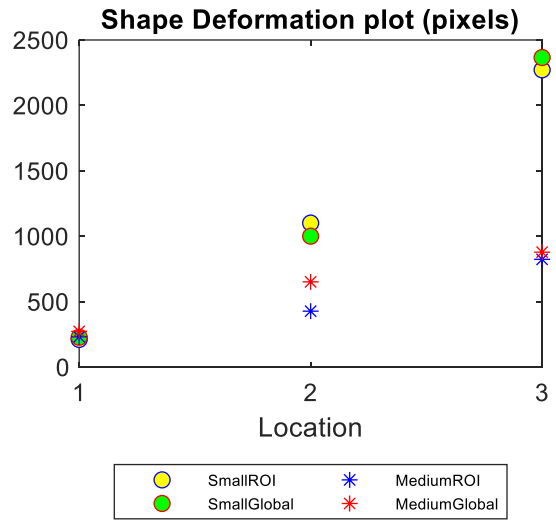

(a)

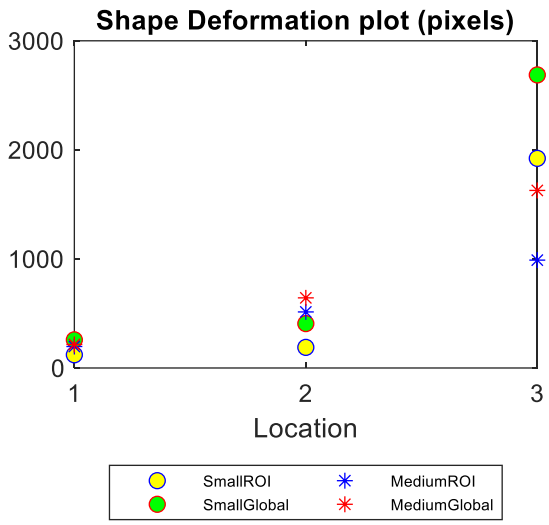

(b)

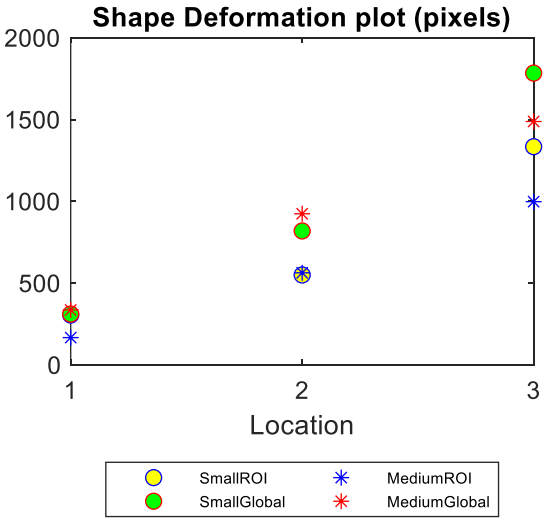

(**c**)

Figure 7.7 Shape deformation (SD) of small and medium objects inserted into the pipe filled up to three water levels: (a) Level 1 (b) Level 2 (c) Level 3.

3. Amplitude response

In Figure 7.8, the sizes of the objects are known and the AR of the reconstructed images using the global and localised methods can be compared against the real distribution. In each plot, the theoretical amplitude response is plotted in dashed lines as a reference. The reconstructions using the localised method perform better than those using the global method as ARs of ROI images are closer to the corresponding theoretical values.

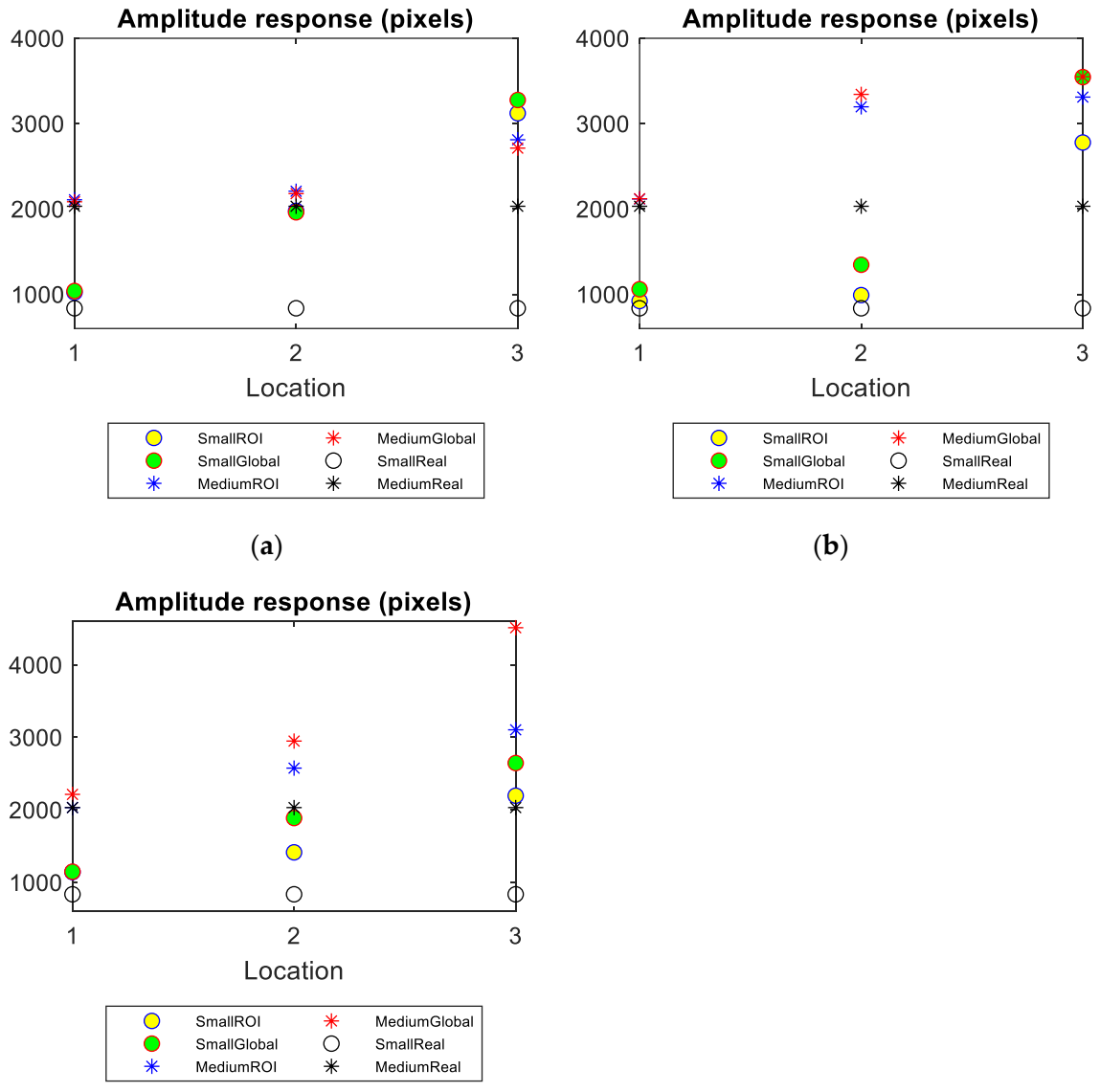

(**c**)

Figure 7.8 Amplitude response (AR) of small and medium objects inserted into the pipe filled up to three water levels: (a) Level 1 (b) Level 2 (c) Level 3.

4. Pearson's correlation coefficient

The plots of CC of the experimental tests under three water levels are presented in Figure 7.9. As discussed before, a low water level, the close position to the centre of inclusions and a small inclusion size could lead to the difficulty of image reconstruction. This can also be observed as a decrease in correlation coefficient between the reconstructed and the true images. Moreover, the CCs of ROI images are generally smaller than those of global images, which advises an improvement made by the limited region reconstruction method.

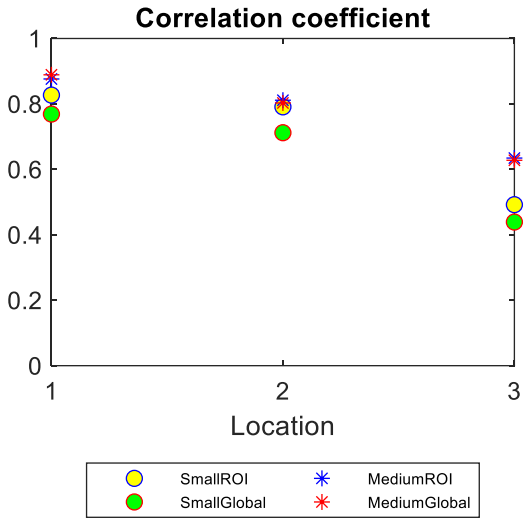

(**a**)

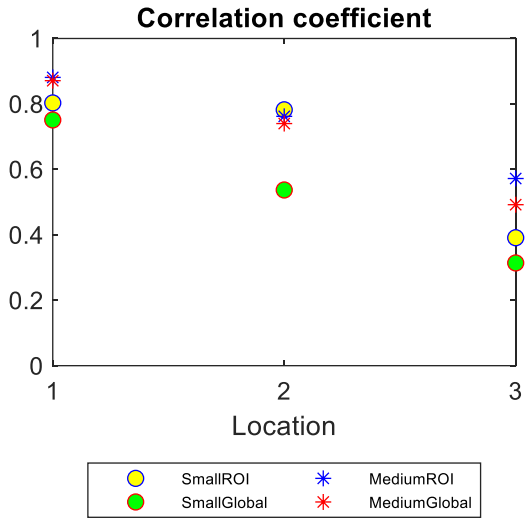

(**b**)

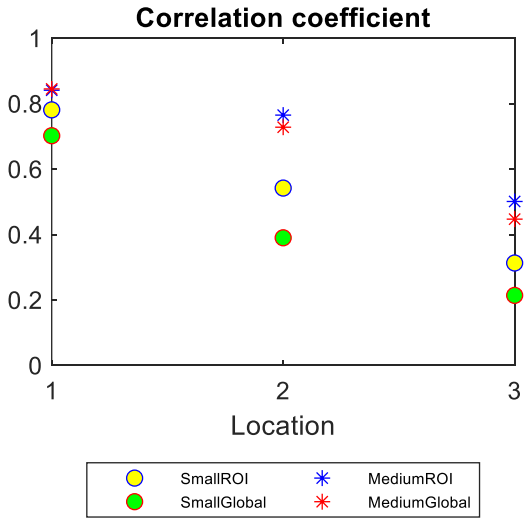

(**c**)

Figure 7.9 Correlation coefficient (CC) of small and medium objects inserted into the pipe filled up to three water levels: (a) Level 1 (b) Level 2 (c) Level 3.

5. Relative error

As suggested from the definition of RE, a smaller value indicates a better reconstruction quality. Figure 7.10 compares the RE plots of the reconstructed images using global and limited region methods. The advantages of applying the proposed method become noticeable when fewer valid measurements are available. As mentioned previously, RE, as well as CC, is introduced to assess the overall reconstruction performances rather than only the target qualities. However, as the demonstrations were set up with one inclusion for simplification, the overall performance of the reconstructions agrees with the target qualities. This can be confirmed by lower REs and Higher CCs offered by ROI mechanism in Figure 7.9 and Figure 7.10. That is to say, the CCs and REs manifest a better recovery of the real images offered by using ROI method as opposed to the global method, as suggested in PE, SD and AR analysis.

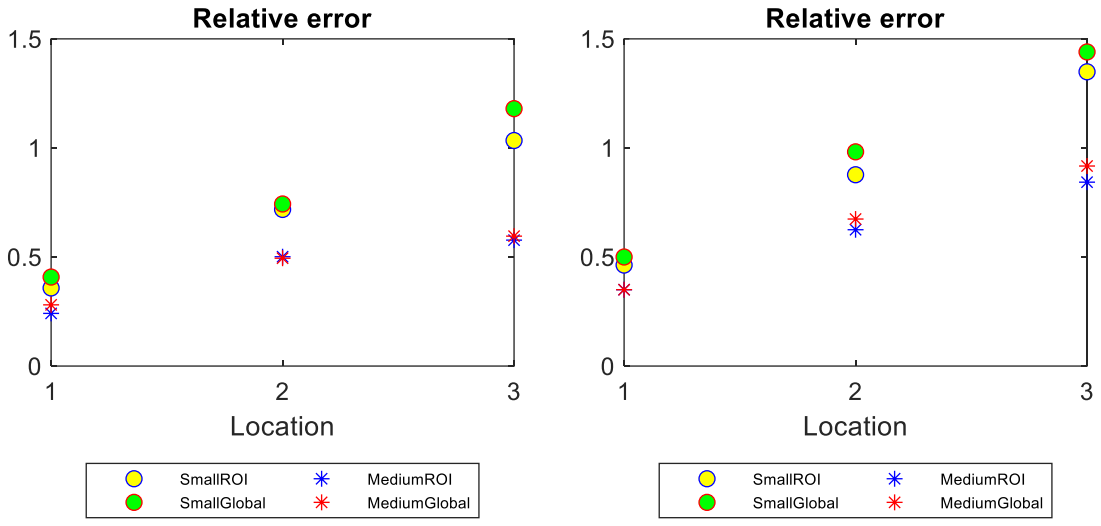

(**a**) (**b**)

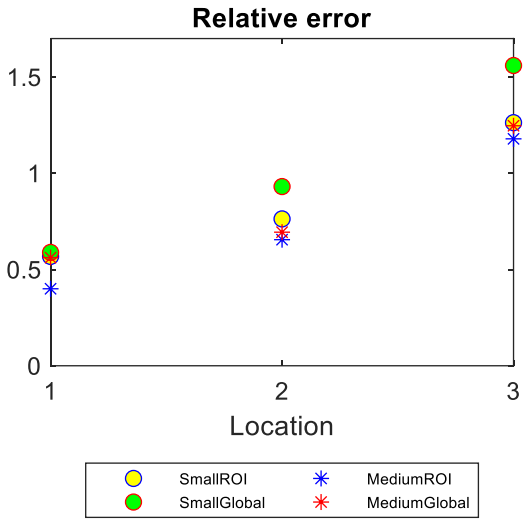

(c)

Figure 7.10 Relative error (RE) of small and medium objects inserted into the pipe filled up to three water levels: (a) Level 1 (b) Level 2 (c) Level 3.

6. Computational time

The computation time is the time required for executing the image reconstruction. As we introduced FEM to simplify the continuous problem into a discretized problem, the image reconstruction is concretely a matrix calculation problem in practice. In the limited region method, the sensitivity matrices involve fewer elements when the size of individual element remains the same; and hence it will spend less time in the mathematical calculation. The computation time is dependent on the processing unit as well as the software platform that the reconstruction is performed on. For making a fair comparison between the two methods, both image reconstructions were accomplished using MATLAB on Intel i7-8550U CPU @ 1.80GHz, which is sufficient for such tasks; and no other programmes were running at the same time. The computation time (in seconds) taken for recovering small and medium objects in the three water level tests is listed below in Table 7.9.

Table 7.9 Computation time of reconstructing small and medium sample using global and ROI methods

Unit (s)	**Medium**						**Small**					
	Global			**ROI**			**Global**			**ROI**		
	P1	**P2**	**P3**	**P1**	**P2**	**P3**	**P1**	**P2**	**P3**	**P1**	**P2**	**P3**
Level 1	0.45	0.47	0.50	0.30	0.38	0.37	0.49	0.48	0.49	0.38	0.36	0.34

Level 2	0.42	0.44	0.47	0.23	0.26	0.30	0.42	0.43	0.42	0.23	0.23	0.22
Level 3	0.43	0.43	0.42	0.18	0.19	0.22	0.44	0.45	0.41	0.19	0.21	0.17

As discussed before, in both the medium and small object tests, the computation time of the limited region method is always smaller than that of global region method. It is also worth noting that, as the water level drops, the ROI area shrinks accordingly, which results in a shorter computation time. This also offers an opportunity for using the localised method to increase the spatial resolution with a finer segmentation under the same computation time.

7.5. Conclusions

This chapter has added an important new feature to the previously developed ERT system for wastewater monitoring into serving part full horizontal pipes. Such improvements involve both hardware modification as well as imaging algorithm advancement. An electrode sensing module has been introduced to determine the instructive electrodes and hence extract the valid measurements, and a dedicated reconstruction method that restricts the reconstruction area to the region of interest (ROI), which is the conductive section within the pipe, is employed to improve the robustness of the system. The impact of this chapter is to provide a solution for recovering the additional information on local concentration profiles within the flow. The proposed localised method was validated by both simulation and experiments under the different levels of flow in comparison with the conventional method. Both profiles have been compared to the real distributions graphically and quantitatively; and it suggests a better agreement between the localised profile and the reality. Therefore, the limited region ERT can be employed to compensate for the system's weak immunity to noise resulting from the incomplete data.

Chapter 8 Conclusion and Future work

8.1. Summary

This work has focused on taking on a promising technology, ERT, and developing it further so that it could be used for measuring wastewater flows. This has involved design and fabrication of a bespoke low-cost ERT data acquisition system that coule be massively deployed for monitoring dynamical flows, together with exploring image reconstruction methods to for a better flow visualization.

At the beginning of this work, in order to understand how ERT systems can help measure flows in sewer networks, the current sewage flow measuring technologies and regulations were reviewed. This, along with the ERT operation principles in its popular multiphase flow applications, sets the specifications of an ERT based wastewater flow meter. Accordingly, an ERT hardware system was designed and presented in Chapter 4. This ERT device was designed to maintain low cost to achieve a well-intergreted sensing system for large-scale deployment. It is accomplished by using analogue circuitry and working in a series driving and measuring strategy under a single stimulation frequency. Obviously such arrangement would compromise some performance aspects, such as very high data acquisition speed and mutifrequency operation mode. However, it has been demonstrated that the proposed system is able to provide measurements with high signal to noise ratio, which can even be increased by data post-processing; and it can collect the data at a speed that can capture some dynamical movements.

Dynamical imaging has been recognized as one of the most important attribute to an ERT system thanks to its high temporal resolution and can contribute to various applications in different domains. In Chapter 5, the dynamical functionality was exploited by post-processing a series of ERT measurements considering two key aspects, movements visualization and velocity profiles. The visualization was demonstrated in the example of in-water handwriting, where an ERT system can reveal handwritten letters/shapes with the help of temporal information whereas this would have been impossible with one frame of data. This involved using temporal image reconstruction based on improved Tikhonov regularization for dynamical imaing processes. In these applications, the correlation between adjacent

frames of data was synthesized when the flows move faster than the data capture speed. The impact of the movement capture and visualization capacity is to track and understand flow behaviours; moreover, it can be equipped with novel machine learning technique to potentially facilitate automated long-term flow behaviour analysis. Following on from the visualization, the flow velocity was estimated by cross-correlating time serires ERT images in the chapter. Preliminary 2D tests compared the ERT based velocity calcuations with the recored velocities and presented a good agreement between these two. The velocity profile estimation plays an important role in analying flow regimes, estimating flowrates, etc. This dynamical imaging capability of the proposed ERT system makes it a good fit in flow measurements and provides an opportunity to integrate the device into a flow control system.

Built upon this initial hardware development, the capability of fucntioning in partially full pipes was addressed to be a requisite for ERT to work in sewerage. The main problem related to such circumstances is the loss of contact with the fluid of some electrodes. This would challenge the system in the way that these electrodes could not provide accurate measurements. To resolve it, the hardware system was further improved accordingly in Chapter 7 Section 7.2 so that it could indicate the not-in-contact electrdoes and eliminate the errorneous measurements. However, this measurement elimination could result in a reduced number of data points in one frame and thus could worsen the ill-posed problem of the reconstruction.

The second investigation was therefore aiming at exploring the image reconstruction methods that could incorporate the partially full pipe flow scenario. This particularly requires an image reconstruction algorithm to deal with the incomplete datasets. A limited region imaging method was proposed in Chapter 6 originally in the context of tumour tracking applications. This method was experimentally compared with the conventional full region recontruction using the primary datasets as well as using the post-processed datasets. The results have shown that the limited region method can achieve the similar denoising effect as the data post-processing; and thus can enhance the system robustness. This method is then applied to the partially full pipe setting in Chapter 7. In these cases, the reconstruction can be limited to the continuous phase region, which was defined by the ‘normal’ electrodes indicated

by the hardware. The sensor was then tested in the lab-scale experiments to demonstrate its capability of revealing inclusions within the fluid phase.

Referring back to the objectives in the introduction in Chapter 1, the conclusion is that these have all been met. Objective 1 was achieved through the hardware development work in Chapter 4. Objective 2 was met in Chapter 5 examining the ERT hardware dynamical ability. Objective 3 has been identified as the most important factor for sewer flow measurements specifically and this has been acomplished by modifying the ERT device in Chpater 7, and creating and applying a limited region reconstruction method in Chapter 6 and Chapter 7. All together, new cost-efficient ERT sensing system which captures dynamical flows, detects liquid level, and reconstructs objects within flows, will bring forward the potential to use ERT in the future for sewer networks monitoring. It should also be noted that although the main focus of this work was wastewater flow measurements, a lot of the advancement and improvements made to ERT can be applied in other fields, such as medical cancer treatment and human and machine interaction.

8.2. Future work

This thesis was the first step towards making ERT a feasible technology in the sewer network operation monitoring. Previously, few devices had been designed for large-scale deployment in this field specifically. In this work, only preliminary studies were established and it is clear that there is still a long way to go for ERT to be effectively used in the aid of sewer monitoring. Commercial evaluation are under way by the company for deployment.

- *ERT Hardware improvement*

Firstly, the system can be extended to be an EIT system, which means the data demodulation module can be altered to make the system able to provide both the amplitude and the phase information. Although the ERT system contains the essential information for process tomography measurements, there are some bio-related processes where phase shift carries useful information - hence EIT can be beneficial.

Secondly, the ERT devive needs to be further developed for long time operation. A current source self-calibration function can also be included to ensure a constant current injection over long period of operation. In addition, a more comprehensive power management module can be considered to allow for different function modes, which can improve the power efficiency and product life span.

Thirdly, more dedicated ERT sensors need to be designed and manufactured to work in the corrosive and hazarous environment, i.e. sewers. Different materials that can be used for electrodes or sensor body need to be thouroughly investigated, concerning operation temperature, pressure, chemical resistance and abrasive resistance, and processing regulation approvals.

- *Field tests*

As suggested, in this thesis only lab-scale tests were presented. These preliminary studies are essential to prove the principle, however, not sufficient. Therefore the next step would be flow loop tests where an in-house flow system can be initially built to simulate the real sewer flows. This setup is still a simplification of a real sewage system, and parameters, such as flowrate, flow conductivity and flow regimes are manageable. Obviously, once the ERT system have successfully functioned in flow loop tests, it could be deployed for trials.

- *Multiplane ERT deployment*

In this work, the ERT system was only validated in 2D experiments. Many dual-plane or even multiplane tomographic systems have been established in the literature. In these studies, the multiplane setup can either improve the reconstructions by accounting for the fringe effects or capture the flow transitions over time. The ERT device developed in this work can offer the possiblity of operating in 3D context by having two rings of electrodes with eight in each ring. To minimize the cross-talk between the planes, previous attempt has been made to employ the 'interleaved' current driving protocol such that only one plane of electrodes is active at any time. This will easily extend the velocity calcuation from the 2D angular calculation to 3D axial computation along the flow direction by cross-correlating the signals obtained at two planes. However, problems possesses with the available electrodes in each plane halved which lead to the reduced number of independent measurements for

image reconstruction of individual plane. This could worsen the ill-posed nature of EIT problem and hence the resulting image qualities. Consequently, the pixel-based cross-correlation technique can potentially suffer. This could potentially be resolved by applying the limited region reconstruction method if a prior knowledge of the ROI is available. Otherwise more sophisicated reconstruction algorithm needs to be adopted.

Reference

[1] C. Putensen, B. Hentze, S. Muenster, and T. Muders, "Electrical Impedance Tomography for Cardio-Pulmonary Monitoring," *Journal of Clinical Medicine,* vol. 8, p. 1176, 08/07 2019, doi: 10.3390/jcm8081176.

[2] L. Gattinoni *et al.*, "Lung Recruitment in Patients with the Acute Respiratory Distress Syndrome," *New England Journal of Medicine,* vol. 354, no. 17, pp. 1775-1786, 2006/04/27 2006, doi: 10.1056/NEJMoa052052.

[3] N. D. Harris, A. J. Suggett, D. C. Barber, and B. H. Brown, "Applications of applied potential tomography (APT) in respiratory medicine," *Clinical Physics and Physiological Measurement,* vol. 8, no. 4A, pp. 155-165, 1987/11 1987, doi: 10.1088/0143-0815/8/4a/020.

[4] H. R. van Genderingen, A. J. van Vught, and J. R. C. Jansen, "Estimation of regional lung volume changes by electrical impedance pressures tomography during a pressure-volume maneuver," *Intensive Care Medicine,* vol. 29, no. 2, pp. 233-240, 2003/02/01 2003, doi: 10.1007/s00134-002-1586-x.

[5] M. C. Bachmann *et al.*, "Electrical impedance tomography in acute respiratory distress syndrome," *Critical Care,* vol. 22, no. 1, p. 263, 2018/10/25 2018, doi: 10.1186/s13054-018-2195-6.

[6] I. Rosemeier, K. Reiter, V. Obermeier, and G. K. Wolf, "Mechanical Ventilation Guided by Electrical Impedance Tomography in Children With Acute Lung Injury," (in eng), *Crit Care Explor,* vol. 1, no. 7, pp. e0020-e0020, 2019, doi: 10.1097/CCE.0000000000000020.

[7] F. Dickin and M. Wang, "Electrical resistance tomography for process applications," *Measurement Science and Technology,* vol. 7, no. 3, pp. 247-260, 1996/03/01 1996, doi: 10.1088/0957-0233/7/3/005.

[8] G. C. Cook, "Construction of London's Victorian sewers: the vital role of Joseph Bazalgette," *Postgraduate Medical Journal,* vol. 77, no. 914, p. 802, 2001, doi: 10.1136/pgmj.77.914.802.

[9] Southernwater. "The wastewater process." https://www.southernwater.co.uk/water-for-life/education/the-wastewater-process (accessed 07/07, 2020).

[10] J. Bourn, "Out of Sight not out of mind: OFWAT AND THE PUBLIC SEWER NETWORK IN ENGLAND AND WALES," The National Audit Office London, 2004.

[11] M. S. Chenning Wu, "Low cost design of Electrical Impedance Tomography hardware system for industrial application," presented at the World Congress on Industrial Process Tomography, Bath, UK, 2018.

[12] C. W. M. H. M. Soleimani, "Smart Water Meter Using Electrical Resistance Tomography," *Sensor,* vol. 19, no. 3043, 2019.

[13] C. Wu and M. Soleimani, "In-water handwriting in multi-medium using electrical impedance imaging," *IOP SciNotes,* vol. 1, no. 2, p. 025001, 2020/07/21 2020, doi: 10.1088/2633-1357/ab9724.

[14] C. Wu and M. Soleimani, "Frequency Difference EIT With Localization: A Potential Medical Imaging Tool During Cancer Treatment," *IEEE Access,* vol. 7, pp. 21870-21878, 2019, doi: 10.1109/ACCESS.2019.2898091.

[15] C. Wu, M. Hutton, and M. Soleimani, "Limited Angle Electrical Resistance Tomography in Wastewater Monitoring," *Sensors,* vol. 20, no. 7, 2020, doi: 10.3390/s20071899.

[16] T. Zhao, C. Wu, and M. Soleimani, "Ionic liquid based distributed touch sensor using electrical impedance tomography," *IOP SciNotes,* vol. 1, no. 2, p. 025005, 2020/09/10 2020, doi: 10.1088/2633-1357/abb345.

[17] (2012). *Waste water treatment in the United Kingdom 2012: Implementation of the European Union Urban Waste Water Treatment Directvie-91/271/EEC*.

[18] A. D. F. Moy, "Wipes in sewer blockages study-Final report," Water UK, London, 2017.

[19] M. T. Bin Ali, Horoshenkov,K.V., Tait, S.J., "Rapid detection of sewer defects and blockages using acoustiv-based instrumentation," *Water science and technology,* vol. 64, no. 8, 2011.

[20] S. Arthur, H. Crow, and L. Pedezert, "Understanding blockage formation in combined sewer networks," *Proceedings of the Institution of Civil Engineers - Water Management,* vol. 161, no. 4, pp. 215-221, 2008, doi: 10.1680/wama.2008.161.4.215.

[21] *Hydro-Logic Smart Monitoring Application Flow, Level, Weather, Quality*.

[22] VEGA. "Measuring techniques for continuous level measurement." https://www.vega.com/en/home_us/products/product-catalog/level (accessed.

[23] "Sector Guidance in relation to the adoption of sewerage assets by sewerage companies in England," in *Code for Adoption Agreements - For water and sewerage companies operating wholly or mainly in England*, ed. England, 2019.

[24] *Industry-Leading Flow Measurement Technologies*. Flow, Density and Viscosity Measurement. [Online]. Available: https://www.emerson.com/documents/automation/brochure-emerson-flow-density-measurement-micro-motion-en-64622.pdf

[25] Omega. "Flow meters." https://www.omega.com/en-us/resources/flow-meters (accessed March 10th, 2020).

[26] rshydro. "Flow Meters for liquid flow in pipes." https://www.rshydro.co.uk/liquid-pipe-flowmeters/ (accessed March 10th, 2020).

[27] F. E. Inc. "Conductivity, Salinity and Total Dissolved Solids." https://www.fondriest.com/environmental-measurements/parameters/water-quality/conductivity-salinity-tds/ (accessed.

[28] F. Prieto, E. Barrado, M. Vega, and L. Deban, "Measurement of Electrical Conductivity of Wastewater for Fast Determination of Metal Ion Concentration," *Russian Journal of Applied Chemistry,* vol. 74, no. 8, pp. 1321-1324, 2001/08/01 2001, doi: 10.1023/A:1013710413982.

[29] E. Levlin, "Conductivity measurements for controlling municipal wastewater treatment," vol. 15, 01/01 2007.

[30] I. Fondriest Environmental. "Conductivity, Salinity and Total Dissolved Solids." https://www.fondriest.com/environmental-measurements/parameters/water-quality/conductivity-salinity-tds/#cond21 (accessed 02/07, 2020).

[31] "water quality measurement." aquaread. https://www.aquaread.com/water-quality-measurement-equipment/ (accessed 02/07, 2020).

[32] "Conductivity Sensor/Resistivity Sensor." Mettler Toledo. https://www.mt.com/gb/en/home/products/Process-Analytics/conductivity-sensor.html (accessed 02/07, 2020).

[33] "Conductivity sensors." KROHNE group. https://krohne.com/en/products/process-analytics/analytical-sensors/conductivity-sensors/ (accessed 02/07, 2020).

[34] "SMART Sewer Project." https://www.em-solutions.co.uk/innovation/smart-sewer-project/ (accessed.

[35] "Smart sewers promise $500m capex savings for Indiana city," *Smart water*, vol. 18, no. 6, 2017.

[36] M. S. Beck and R. A. Williams, "Process tomography: a European innovation and its applications," *Measurement Science and Technology,* vol. 7, no. 3, pp. 215-224, 1996/03/01 1996, doi: 10.1088/0957-0233/7/3/002.

[37] X. J. Robert M. West, R. A. Williams, "Parametric modelling in industrial process tomography," presented at the 1st World Congress on Industrial Process Tomography, Greater Manchester; United Kingdom, 1999.

[38] R. A. Williams *et al.*, "Industrial monitoring of hydrocyclone operation using electrical resistance tomography," *Minerals Engineering,* vol. 12, no. 10, pp. 1245-1252, 1999/10/01/ 1999, doi: https://doi.org/10.1016/S0892-6875(99)00109-0.

[39] D. Vlaev, M. Wang, T. Dyakowski, R. Mann, and B. D. Grieve, "Detecting filter-cake pathologies in solid–liquid filtration: semi-tech scale demonstrations using electrical resistance tomography

(ERT)," *Chemical Engineering Journal,* vol. 77, no. 1, pp. 87-91, 2000/04/15/ 2000, doi: https://doi.org/10.1016/S1385-8947(99)00142-4.

[40] T. Dyakowski *et al.*, "Imaging nylon polymerisation processes by applying electrical tomography," *Chemical Engineering Journal,* vol. 77, no. 1, pp. 105-109, 2000/04/15/ 2000, doi: https://doi.org/10.1016/S1385-8947(99)00132-1.

[41] W. Daily and A. Ramirez, "The role of electrical resistance tomography in the U.S. nuclear waste site characterization program," 01/01 1999.

[42] A. Ramirez, W. Daily, A. Binley, D. LaBrecque, and D. Roelant, "Detection of Leaks in Underground Storage Tanks Using Electrical Resistance Methods," *Journal of Environmental and Engineering Geophysics - J ENVIRON ENG GEOPHYS,* vol. 1, 12/01 1996, doi: 10.4133/JEEG1.3.189.

[43] M. Gasulla, J. Jordana, and R. Pallas-Areny, *2D and 3D subsurface resistivity imaging using a constrained least-squares algorithm*. 1999.

[44] J. Jordana, M. Gasulla, and R. Pallas-Areny, "Electrical resistance tomography to detect leaks from buried pipes," *Measurement Science and Technology,* vol. 12, p. 1061, 07/18 2001, doi: 10.1088/0957-0233/12/8/311.

[45] M. Wang and J. J. Cilliers, "Detecting non-uniform foam density using electrical resistance tomography," *Chemical Engineering Science,* vol. 54, no. 5, pp. 707-712, 1999/03/01/ 1999, doi: https://doi.org/10.1016/S0009-2509(98)00277-2.

[46] M. V. Sardeshpande, G. Kumar, T. Aditya, and V. V. Ranade, "Mixing studies in unbaffled stirred tank reactor using electrical resistance tomography," *Flow Measurement and Instrumentation,* vol. 47, pp. 110-121, 2016/03/01/ 2016, doi: https://doi.org/10.1016/j.flowmeasinst.2016.01.003.

[47] Y. Faraj, M. Wang, and J. Jia, *Application of the ERT for slurry flow regime characterisation*. 2013.

[48] M. Wang, S. Johnstone, W. Pritchard, and T. York, "Modelling and Mapping Electrical Resistance Changes Due to Hearth Erosion in a 'Cold'Model of a Blast Furnace," 05/14 1999.

[49] D. M. S. a. O. W. Gutsche, "ECT Studies of Bead Fluidization in Vertical Mills," presented at the World congress on industrial process tomography, Buxton, UK, 1999.

[50] A. J. Jaworski and T. Dyakowski, "Application of electrical capacitance tomography for measurement of gas-solids flow characteristics in a pneumatic conveying system," *Measurement Science and Technology,* vol. 12, no. 8, pp. 1109-1119, 2001/07/18 2001, doi: 10.1088/0957-0233/12/8/317.

[51] M. Young, E. Pickup, R. Deloughry, T. Hartley, S. A. Nixon, and L. Barratt, "Development of a variable density flowmeter for an industrial application using tomographic imaging," in *IEE Colloquium on Advances in Electrical Tomography (Digest No: 1196/143)*, 19-19 June 1996 1996, pp. 14/1-14/3, doi: 10.1049/ic:19960842.

[52] R. Waterfall, R. He, P. Wolanski, and Z. Gut, "Monitoring Flame Position and Stability in Combustion Cans using ECT," 05/14 1999.

[53] W. Wang and H. Yang, "Imaging a rectangular fluidised bed by electrical capacitance tomography: Preliminary results," *Sensor Review,* vol. 31, pp. 315-320, 09/13 2011, doi: 10.1108/02602281111169721.

[54] M. Bennett, S. Luke, X. Jia, R. West, and R. Williams, "Analysis and flow regime identification of bubble column dynamics," *1st World Congress on Industrial Process Tomography,* 05/14 0002.

[55] S. J. Wang, D. Geldart, M. S. Beck, and T. Dyakowski, "A behaviour of a catalyst powder flowing down in a dipleg," *Chemical Engineering Journal,* vol. 77, pp. 51-56, 04/15 2000, doi: 10.1016/S1385-8947(99)00144-8.

[56] R. A. Williams, S. P. Luke, K. L. Ostrowski, and M. A. Bennett, "Measurement of bulk particulates on belt conveyor using dielectric tomography," *Chemical Engineering Journal,* vol. 77, no. 1, pp. 57-63, 2000/04/15/ 2000, doi: https://doi.org/10.1016/S1385-8947(99)00146-1.

[57] K. Tomkiewicz, A. Pląskowski, M. S. Beck, and M. Byars, "Testing of the failure of a solid rocket propellant with tomography methods," *Chemical Engineering Journal,* vol. 77, no. 1, pp. 73-78, 2000/04/15/ 2000, doi: https://doi.org/10.1016/S1385-8947(99)00147-3.

[58] R. Binns, A. R. A. Lyons, A. J. Peyton, and W. D. N. Pritchard, "Imaging molten steel flow profiles," *Measurement Science and Technology,* vol. 12, no. 8, pp. 1132-1138, 2001/07/18 2001, doi: 10.1088/0957-0233/12/8/320.

[59] L. Ma, S. Spagnul, and M. Soleimani, "Metal Solidification Imaging Process by Magnetic Induction Tomography," *Scientific Reports,* vol. 7, no. 1, p. 14502, 2017/11/06 2017, doi: 10.1038/s41598-017-15131-z.

[60] T. York, "Status of electrical tomography in industrial applications," *Journal of Electronic Imaging,* vol. 10, no. 3, pp. 608-619, 2001.

[61] H. Xue, Z. Fan, H. Wei, L. Wei, and M. Lixiang, "Chemical waste water filtration monitoring based on electrical capacitance tomography," in *2015 12th International Conference on Fuzzy Systems and Knowledge Discovery (FSKD)*, 15-17 Aug. 2015 2015, pp. 1893-1897.

[62] J. Lillo, D. Gomez-Ortiz, T. Crespo, F. Carreño, I. De Bustamante, and P. Espí, "Using electrical resistivity tomography (ERT) to evaluate the infiltration in land application systems. A case study in the Carrión de los Céspedes wastewater treatment plant (Seville, Spain)," *Desalination and Water Treatment - DESALIN WATER TREAT,* vol. 4, pp. 111-115, 04/01 2009, doi: 10.5004/dwt.2009.364.

[63] S. Hosseini, D. Patel, F. Ein-Mozaffari, and M. Mehrvar, "Study of Solid-liquid Agitated Tanks through Electrical Resistance Tomography," *Chemical Engineering Science - CHEM ENG SCI,* vol. 65, pp. 1374-1384, 02/01 2010, doi: 10.1016/j.ces.2009.10.007.

[64] *Performance Standards and Test Procedures for Continuous Water Monitoring Equipment Part 3: Performance standards and test procedures for water flowmeters,* E. Agency, 2020.

[65] J. Yao and M. Takei, "Application of Process Tomography to Multiphase Flow Measurement in Industrial and Biomedical Fields: A Review," *IEEE Sensors Journal,* vol. 17, no. 24, pp. 8196-8205, 2017, doi: 10.1109/JSEN.2017.2682929.

[66] M. G. Rasteiro, R. C. C. Silva, F. A. P. Garcia, and P. M. Faia, "Electrical Tomography: a review of Configurations and Applications to Particulate Processes," *KONA Powder and Particle Journal,* vol. 29, pp. 67-80, 2011, doi: 10.14356/kona.2011010.

[67] J. Jia, M. Wang, H. I. Schlaberg, and H. Li, "A novel tomographic sensing system for high electrically conductive multiphase flow measurement," *Flow Measurement and Instrumentation,* vol. 21, no. 3, pp. 184-190, 2010/09/01/ 2010, doi: https://doi.org/10.1016/j.flowmeasinst.2009.12.002.

[68] B. KarKi, Faraj, Y; Wang, M, "Electrical conductivity based flow regime recognition of two phase flows in horizontal pipeline," in *8th World congress on Industrial Process Tomography* Iguassu Falls, PR, Brazil, 2016: International Society for Industrial Process Tomography.

[69] Y. Zhang and Y. Chen, "A Novel PCA-GRNN Flow Pattern Identification Algorithm for Electrical Resistance Tomography System," in *Advances in Computer Science and Information Engineering*, Berlin, Heidelberg, D. Jin and S. Lin, Eds., 2012// 2012: Springer Berlin Heidelberg, pp. 249-254.

[70] C. Tan, F. Dong, and M. Wu, "Identification of gas/liquid two-phase flow regime through ERT-based measurement and feature extraction," *Flow Measurement and Instrumentation,* vol. 18, no. 5, pp. 255-261, 2007/10/01/ 2007, doi: https://doi.org/10.1016/j.flowmeasinst.2007.08.003.

[71] F. Dong, C. Xu, Z. Zhang, and S. Ren, "Design of Parallel Electrical Resistance Tomography System for Measuring Multiphase Flow," *Chinese Journal of Chemical Engineering,* vol. 20, no. 2, pp. 368-379, 2012/04/01/ 2012, doi: https://doi.org/10.1016/S1004-9541(12)60400-5.

[72] C. Tan, F. Dong, C. Xu, Z. Zhang, and S. Ren, "Electrical resistance tomography system for two-phase flow monitoring," *Dongnan Daxue Xuebao (Ziran Kexue Ban)/Journal of Southeast University (Natural Science Edition),* Article vol. 41, no. SUPPL. 1, pp. 125-129, 2011, doi: 10.3969/j.issn.1001-0505.2011.S1.027.

[73] J. L. G. Oliveira, J. C. Passos, R. Verschaeren, and C. v. d. Geld, "Mass flow rate measurements in gas–liquid flows by means of a venturi or orifice plate coupled to a void fraction sensor," *Experimental Thermal and Fluid Science,* vol. 33, no. 2, pp. 253-260, 2009/01/01/ 2009, doi: https://doi.org/10.1016/j.expthermflusci.2008.08.008.

[74] M. Henningsson, K. Östergren, and P. Dejmek, "Plug flow of yoghurt in piping as determined by cross-correlated dual-plane electrical resistance tomography," *Journal of Food Engineering,* vol. 76, no. 2, pp. 163-168, 2006/09/01/ 2006, doi: https://doi.org/10.1016/j.jfoodeng.2005.05.004.

[75] M. Sharifi and B. Young, "Qualitative visualization and quantitative analysis of milk flow using electrical resistance tomography," *Journal of Food Engineering,* vol. 112, no. 3, pp. 227-242, 2012/10/01/ 2012, doi: https://doi.org/10.1016/j.jfoodeng.2012.04.008.

[76] C. Tan, N.-n. Wang, and F. Dong, "Oil–water two-phase flow pattern analysis with ERT based measurement and multivariate maximum Lyapunov exponent," *Journal of Central South University,* vol. 23, no. 1, pp. 240-248, 2016/01/01 2016, doi: 10.1007/s11771-016-3067-3.

[77] F. Dong, Y. Xu, L. Hua, and H. Wang, "Two Methods for Measurement of Gas-Liquid Flows in Vertical Upward Pipe Using Dual-Plane ERT System," *IEEE Transactions on Instrumentation and Measurement,* vol. 55, no. 5, pp. 1576-1586, 2006, doi: 10.1109/TIM.2006.881564.

[78] J. Sun and W. Yang, "A dual-modality electrical tomography sensor for measurement of gas–oil–water stratified flows," *Measurement,* vol. 66, pp. 150-160, 2015/04/01/ 2015, doi: https://doi.org/10.1016/j.measurement.2015.01.032.

[79] G. Annamalai, S. Pirouzpanah, S. R. Gudigopuram, and G. L. Morrison, "Characterization of flow homogeneity downstream of a slotted orifice plate in a two-phase flow using electrical resistance tomography," *Flow Measurement and Instrumentation,* vol. 50, pp. 209-215, 2016/08/01/ 2016, doi: https://doi.org/10.1016/j.flowmeasinst.2016.07.003.

[80] J. Polansky and M. Wang, "Proper Orthogonal Decomposition as a technique for identifying two-phase flow pattern based on electrical impedance tomography," *Flow Measurement and Instrumentation,* vol. 53, pp. 126-132, 2017/03/01/ 2017, doi: https://doi.org/10.1016/j.flowmeasinst.2016.10.004.

[81] T. Zhao, T. Eda, S. Achyut, J. Haruta, M. Nishio, and M. Takei, "Investigation of pulsing flow regime transition and pulse characteristics in trickle-bed reactor by electrical resistance tomography," *Chemical Engineering Science,* vol. 130, pp. 8-17, 2015/07/07/ 2015, doi: https://doi.org/10.1016/j.ces.2015.03.010.

[82] J. N. Gao ZK., Wang WX, "Definition of Flow Patterns," in *Nonlinear Analysis of Gas-Water/Oil-Water Two-Phase Flow in Complex Networks*: Springer, Berlin, Heidelberg, 2014.

[83] F. Dong, Y. B. Xu, L. J. Xu, L. Hua, and X. T. Qiao, "Application of dual-plane ERT system and cross-correlation technique to measure gas–liquid flows in vertical upward pipe," *Flow Measurement and Instrumentation,* vol. 16, no. 2, pp. 191-197, 2005/04/01/ 2005, doi: https://doi.org/10.1016/j.flowmeasinst.2005.02.010.

[84] J. Jia, M. Wang, and Y. Faraj, "Evaluation of EIT systems and algorithms for handling full void fraction range in two-phase flow measurement," *Measurement Science and Technology,* vol. 26, no. 1, p. 015305, 2014/12/15 2014, doi: 10.1088/0957-0233/26/1/015305.

[85] C. Tan and F. Dong, "Gas-water two-phase flow regime identification with feature fusion from an ERT system and a V-cone meter," in *2009 IEEE International Workshop on Imaging Systems and Techniques*, 11-12 May 2009 2009, pp. 307-312, doi: 10.1109/IST.2009.5071655.

[86] C. E. Brennen, "Flow patterns," in *Fundamentals of Multiphase Flows*: Cambridge University Press, 2008, ch. 7.

[87] M. Wang, "2 - Electrical impedance tomography," in *Industrial Tomography*, M. Wang Ed.: Woodhead Publishing, 2015, pp. 23-59.

[88] B. H. Brown and A. D. Seagar, "The Sheffield data collection system," *Clinical Physics and Physiological Measurement,* vol. 8, no. 4A, pp. 91-97, 1987/11 1987, doi: 10.1088/0143-0815/8/4a/012.

[89] A. J. Wilson, P. Milnes, A. R. Waterworth, R. H. Smallwood, and B. H. Brown, "Mk3.5: a modular, multi-frequency successor to the Mk3a EIS/EIT system," *Physiological Measurement,* vol. 22, no. 1, pp. 49-54, 2001/02/01 2001, doi: 10.1088/0967-3334/22/1/307.

[90] H. Wi, H. Sohal, A. McEwan, E. J. Woo, and T. Oh, "Multi-Frequency Electrical Impedance Tomography System With Automatic Self-Calibration for Long-Term Monitoring," *IEEE Transactions on Biomedical Circuits and Systems,* vol. 8, pp. 119-128, 06/11 2013, doi: 10.1109/TBCAS.2013.2256785.

[91] A. Hartov, T. Kerner, M. Markova, K. Osterman, and K. Paulsen, "Dartmouth's next generation EIS system: Preliminary hardware considerations," *Physiological measurement,* vol. 22, pp. 25-30, 03/01 2001, doi: 10.1088/0967-3334/22/1/304.

[92] R. D. Cook, G. J. Saulnier, D. G. Gisser, J. C. Goble, J. C. Newell, and D. Isaacson, "ACT3: a high-speed, high-precision electrical impedance tomograph," *IEEE Transactions on Biomedical Engineering,* vol. 41, no. 8, pp. 713-722, 1994, doi: 10.1109/10.310086.

[93] C. N. McLeod, F. J. Lidgey, and Q. S. Zhu, "Multiple drive EIT systems," in *IEE Colloquium on Electrical Impedance Tomography/Applied Potential Tomography*, 13-13 Oct. 1992 1992, pp. 1/1-1/3.

[94] M. M. Mellenthin *et al.*, "The ACE1 Electrical Impedance Tomography System for Thoracic Imaging," *IEEE Transactions on Instrumentation and Measurement,* vol. 68, no. 9, pp. 3137-3150, 2019, doi: 10.1109/TIM.2018.2874127.

[95] W. Mi, M. Yixin, N. Holliday, D. Yunfeng, R. A. Williams, and G. Lucas, "A high-performance EIT system," *IEEE Sensors Journal,* vol. 5, no. 2, pp. 289-299, 2005, doi: 10.1109/JSEN.2005.843904.

[96] J. J. Cilliers, W. Xie, S. J. Neethling, E. W. Randall, and A. J. Wilkinson, "Electrical resistance tomography using a bi-directional current pulse technique," *Measurement Science and Technology,* vol. 12, no. 8, pp. 997-1001, 2001/07/18 2001, doi: 10.1088/0957-0233/12/8/302.

[97] I. Frerichs *et al.*, "Chest electrical impedance tomography examination, data analysis, terminology, clinical use and recommendations: consensus statement of the TRanslational EIT developmeNt stuDy group," *Thorax,* vol. 72, no. 1, p. 83, 2017, doi: 10.1136/thoraxjnl-2016-208357.

[98] T. Goldstein and S. Osher, "The Split Bregman Method for L1-Regularized Problems," *SIAM Journal on Imaging Sciences,* vol. 2, no. 2, pp. 323-343, 2009, doi: 10.1137/080725891.

[99] Rocsole;. "Rocsole Flow Water." (accessed 22/02, 2019).

[100] itoms;. "Flow-ITOMETER for visualizing flows." https://www.itoms.com/products/flow-visualiser/ (accessed 22/02, 2019).

[101] R. W. M. Smith, I. L. Freeston, and B. H. Brown, "A real-time electrical impedance tomography system for clinical use-design and preliminary results," *IEEE Transactions on Biomedical Engineering,* vol. 42, no. 2, pp. 133-140, 1995, doi: 10.1109/10.341825.

[102] B. H. Brown *et al.*, "High frequency EIT data collection and parametric imaging," 1994.

[103] W. R. B. Lionheart, "EIT reconstruction algorithms: pitfalls, challenges and recent developments," *Physiological Measurement,* vol. 25, no. 1, pp. 125-142, 2004/02/01 2004, doi: 10.1088/0967-3334/25/1/021.

[104] J. S. Martins, C. S. Moura, and R. M. F. Vargas, "Image reconstruction using simulated annealing in electrical impedance tomography: a new approach," *Inverse Problems in Science and Engineering,* vol. 26, no. 6, pp. 834-854, 2018/06/03 2018, doi: 10.1080/17415977.2017.1361420.

[105] D. Holder, "Electrical Impedance Tomography: Methods, History and Applications," vol. 32, 2005.

[106] M. Cheney, D. Isaacson, J. C. Newell, S. Simske, and J. Goble, "NOSER: An algorithm for solving the inverse conductivity problem," *International journal of imaging systems and technology,* vol. 2, no. 2, pp. 66-75, 1990, doi: 10.1002/ima.1850020203
info:doi/10.1002/ima.1850020203.

[107] N. Polydorides, "Image reconstruction algorithms for soft-field tomography," Doctor of Philosophy, Department of Electrical engineering and Electronics, University of Manchester Institute of Science and Technology, Manchester, UK, 2002.

[108] J. Wang, J. Ma, B. Han, and Q. Li, "Split Bregman iterative algorithm for sparse reconstruction of electrical impedance tomography," *Signal Processing,* vol. 92, no. 12, pp. 2952-2961, 12// 2012, doi: http://dx.doi.org/10.1016/j.sigpro.2012.05.027.

[109] G. S. d. S. Zhou Zhou, Thomas Dowrick, James Avery, Zhaolin Sun, Hui Xu, David Holder, "Comparison of Total variation algorithms for electrical impedance tomography " *Phys. Med. Biol.,* vol. 36, no. 6, 2015.

[110] Z. Zhou *et al.*, "Comparison of total variation algorithms for electrical impedance tomography," *Physiological Measurement,* vol. 36, no. 6, pp. 1193-1209, 2015/05/26 2015, doi: 10.1088/0967-3334/36/6/1193.

[111] A. Adler, T. Dai, and W. R. B. Lionheart, "Temporal image reconstruction in electrical impedance tomography," *Physiological Measurement,* vol. 28, no. 7, pp. S1-S11, 2007/06/26 2007, doi: 10.1088/0967-3334/28/7/s01.

[112] M. Vauhkonen, P. A. Karjalainen, and J. P. Kaipio, "A Kalman filter approach to track fast impedance changes in electrical impedance tomography," *IEEE Transactions on Biomedical Engineering,* vol. 45, no. 4, pp. 486-493, 1998, doi: 10.1109/10.664204.

[113] P. J. Vauhkonen, M. Vauhkonen, T. Makinen, P. Karjalainen, and J. Kaipio, "Dynamic electrical impedance tomography - Phantom studies," *INVERSE PROBLEMS IN ENGINEERING,* vol. 8, pp. 495-510, 10/01 2000, doi: 10.1080/174159700088027743.

[114] K. Y. Kim, B. S. Kim, M. C. Kim, Y. J. Lee, and M. Vauhkonen, "Image reconstruction in time-varying electrical impedance tomography based on the extended Kalman filter," *Measurement Science and Technology,* vol. 12, no. 8, pp. 1032-1039, 2001/07/18 2001, doi: 10.1088/0957-0233/12/8/307.

[115] M. Yasin, S. Böhm, P. O. Gaggero, and A. Adler, "Evaluation of EIT system performance," *Physiological Measurement,* vol. 32, no. 7, pp. 851-865, 2011/06/07 2011, doi: 10.1088/0967-3334/32/7/s09.

[116] P. O. Gaggero, A. Adler, A. D. Waldmann, Y. Mamatjan, J. Justiz, and V. M. Koch, "Automated robust test framework for electrical impedance tomography," *Physiological Measurement,* vol. 36, no. 6, pp. 1227-1244, 2015/05/26 2015, doi: 10.1088/0967-3334/36/6/1227.

[117] A. Javaherian, A. Movafeghi, R. Faghihi, and E. Yahaghi, "An exhaustive criterion for estimating quality of images in electrical impedance tomography with application to clinical imaging," *Journal of Visual Communication and Image Representation,* vol. 24, no. 7, pp. 773-785, 2013/10/01/ 2013, doi: https://doi.org/10.1016/j.jvcir.2013.05.003.

[118] A. Adler *et al.*, "GREIT: a unified approach to 2D linear EIT reconstruction of lung images," *Physiological Measurement,* vol. 30, no. 6, pp. S35-S55, 2009/06/01 2009, doi: 10.1088/0967-3334/30/6/s03.

[119] tech4imaging;. "Multi-Phase Flow Meters." https://www.tech4imaging.com/multiphase-flow/multiphase-flow-meter/ (accessed 22/02, 2019).

[120] S. R. Aw, R. A. Rahim, M. H. F. Rahiman, F. R. M. Yunus, and C. L. Goh, "Electrical resistance tomography: A review of the application of conducting vessel walls," *Powder Technology,* vol. 254, pp. 256-264, 2014/03/01/ 2014, doi: https://doi.org/10.1016/j.powtec.2014.01.050.

[121] Y. L. Zhao, M. Wang, and J. Yao, *Electrical Impedance Tomography Spectroscopy Method for Characterising Particles in Solid-Liquid Phase*. 2014.

[122] Y. Kim, A. Simpson, and M. Lambert, *Behavior of orifices and blockages in unsteady pipe flows*. 2007.

[123] M. Wang, "Electrical impedance tomography on conducting walled process vessels," Doctoral, University of Manchester, 1994.

[124] K. G. Boone and D. S. Holder, "Current approaches to analogue instrumentation design in electrical impedance tomography," *Physiological Measurement,* vol. 17, no. 4, pp. 229-247, 1996/11/01 1996, doi: 10.1088/0967-3334/17/4/001.

[125] J. Lee, U. Ha, and H. Yoo, "30-fps SNR equalized electrical impedance tomography IC with fast-settle filter and adaptive current control for lung monitoring," in *2016 IEEE International*

Symposium on Circuits and Systems (ISCAS), 22-25 May 2016 2016, pp. 109-112, doi: 10.1109/ISCAS.2016.7527182.

[126] A. Adler *et al.*, "GREIT: a unified approach to 2D linear EIT reconstruction of lung images," (in eng), *Physiol Meas,* vol. 30, no. 6, pp. S35-55, Jun 2009, doi: 10.1088/0967-3334/30/6/s03.

[127] E. O. Etuke and R. T. Bonnecaze, "Measurement of angular velocities using electrical impedance tomography," *Flow Measurement and Instrumentation,* vol. 9, no. 3, pp. 159-169, 1998/09/01/ 1998, doi: https://doi.org/10.1016/S0955-5986(98)00020-X.

[128] C. Amma, M. Georgi, and T. Schultz, "Airwriting: Hands-Free Mobile Text Input by Spotting and Continuous Recognition of 3d-Space Handwriting with Inertial Sensors," in *2012 16th International Symposium on Wearable Computers*, 18-22 June 2012 2012, pp. 52-59, doi: 10.1109/ISWC.2012.21.

[129] M. Chen, G. AlRegib, and B. Juang, "Air-Writing Recognition—Part I: Modeling and Recognition of Characters, Words, and Connecting Motions," *IEEE Transactions on Human-Machine Systems,* vol. 46, no. 3, pp. 403-413, 2016, doi: 10.1109/THMS.2015.2492598.

[130] J. Gan and W. Wang, "In-air handwritten English word recognition using attention recurrent translator," *Neural Computing and Applications,* vol. 31, no. 7, pp. 3155-3172, 2019/07/01 2019, doi: 10.1007/s00521-017-3260-9.

[131] E. Knapp, "Chapter 5 - How Industrial Networks Operate," in *Industrial Network Security*, E. Knapp Ed. Boston: Syngress, 2011, pp. 89-110.

[132] Y. Dai, M. Wang, N. Panagiotopoulos, G. Lucas, and R. Williams, *3-D visualisation of a swirling flow using electrical resistance tomography*. 2005.

[133] A. Saoud, V. Mosorov, and K. Grudzien, "Measurement of velocity of gas/solid swirl flow using Electrical Capacitance Tomography and cross correlation technique," *Flow Measurement and Instrumentation,* vol. 53, pp. 133-140, 2017/03/01/ 2017, doi: https://doi.org/10.1016/j.flowmeasinst.2016.08.003.

[134] H. Li and Y. Tomita, "Characterization of pressure fluctuation in swirling gas-solid two-phase flow in a horizontal pipe," *Advanced Powder Technology,* vol. 12, no. 2, pp. 169-185, 2001/01/01/ 2001, doi: https://doi.org/10.1163/15685520052385005.

[135] X. Deng, F. Dong, L. J. Xu, X. P. Liu, and L. A. Xu, "The design of a dual-plane AB - Combining electrical resistance tomography (ERT) with the cross-correlation flow measurement technique can provide more information on the flow than usual. A dual-plane ERT system for use on laboratory- and plant-scale process equipment has been developed on the basis of this idea. This paper focuses on the design of it. The principle of measurement of the local gas velocity distribution in a bubbly gas/liquid pipe flow based on pixel-pixel cross correlation of two plane images is described. Methods to improve the real-time performance of the system are also discussed in detail. Initial experimental results illustrate the feasibility of the method presented here. ERT system for cross correlation measurement of bubbly gas/liquid pipe flow," *Measurement Science and Technology,* vol. 12, no. 8, pp. 1024-1031, 2001/07/18 2001, doi: 10.1088/0957-0233/12/8/306.

[136] Y. Wu, H. Li, M. Wang, and R. A. Williams, "Characterization of Air-Water Two-Phase Vertical Flow by Using Electrical Resistance Imaging," *The Canadian Journal of Chemical Engineering,* vol. 83, no. 1, pp. 37-41, 2005/02/01 2005, doi: 10.1002/cjce.5450830107.

[137] D. Silvera-Tawil, D. Rye, and M. Velonaki, "Interpretation of Social Touch on an Artificial Arm Covered with an EIT-based Sensitive Skin," *International Journal of Social Robotics,* vol. 6, no. 4, pp. 489-505, 2014/11/01 2014, doi: 10.1007/s12369-013-0223-x.

[138] D. Silvera-Tawil, D. Rye, M. Soleimani, and M. Velonaki, "Electrical Impedance Tomography for Artificial Sensitive Robotic Skin: A Review," *IEEE Sensors Journal,* vol. 15, no. 4, pp. 2001-2016, 2015, doi: 10.1109/JSEN.2014.2375346.

[139] T. Schlegl, T. Kröger, A. Gaschler, O. Khatib, and H. Zangl, "Virtual whiskers — Highly responsive robot collision avoidance," in *2013 IEEE/RSJ International Conference on Intelligent Robots and Systems*, 3-7 Nov. 2013 2013, pp. 5373-5379, doi: 10.1109/IROS.2013.6697134.

[140] D. C. Barber and B. H. Brown, "Applied potential tomography," *Journal of Physics E: Scientific Instruments,* vol. 17, no. 9, p. 723, 1984. [Online]. Available: http://stacks.iop.org/0022-3735/17/i=9/a=002.

[141] I. Frerichs *et al.*, "Chest electrical impedance tomography examination, data analysis, terminology, clinical use and recommendations: consensus statement of the TRanslational EIT developmeNt stuDy group," *Thorax,* vol. 72, no. 1, pp. 83-93, 2017, doi: 10.1136/thoraxjnl-2016-208357.

[142] T. Pengpan, N. D. Smith, W. Qiu, A. Yao, C. N. Mitchell, and M. Soleimani, "A motion-compensated cone-beam CT using electrical impedance tomography imaging," *Physiological Measurement,* vol. 32, no. 1, p. 19, 2011. [Online]. Available: http://stacks.iop.org/0967-3334/32/i=1/a=002.

[143] M. D. Ander Biguri, Steven Hancock, Manuchehr Soleimani, "A general method for motion compensation in X-ray computed tomograph," presented at the CERN-OPEN-2017-018, Geneva, Switzerland, 2016.

[144] T. Gupta and C. A. Narayan, "Image-guided radiation therapy: Physician's perspectives," *Journal of Medical Physics / Association of Medical Physicists of India,* vol. 37, no. 4, pp. 174-182, Oct-Dec

01/17/received

07/09/revised

10/08/accepted 2012, doi: 10.4103/0971-6203.103602.

[145] K. V. Liu D, Siltanen S, Laukkanen A M and Seppänen A "Estimation of conductivity changes in a region of interest with electrical impedance tomography," *Inverse Probl. Imaging,* vol. 9, no. 211, p. 29, 2015.

[146] L. Miao, Y. Ma, and J. Wang, "ROI-Based Image Reconstruction of Electrical Impedance Tomography Used to Detect Regional Conductivity Variation," *IEEE Transactions on Instrumentation and Measurement,* vol. 63, no. 12, pp. 2903-2910, 2014, doi: 10.1109/TIM.2014.2326765.

[147] H. Kwon, A. L. McEwan, T. I. Oh, A. Farooq, E. J. Woo, and J. K. Seo, "A Local Region of Interest Imaging Method for Electrical Impedance Tomography with Internal Electrodes," *Computational and Mathematical Methods in Medicine,* vol. 2013, p. 9, 2013, Art no. 964918, doi: 10.1155/2013/964918.

[148] M. Wang, Q. Wang, and B. Karki, "Arts of electrical impedance tomographic sensing," *Philosophical transactions. Series A, Mathematical, physical, and engineering sciences,* vol. 374, no. 2070, p. 20150329, 03/14/accepted 2016, doi: 10.1098/rsta.2015.0329.

[149] J. A. Victorino *et al.*, "Imbalances in Regional Lung Ventilation," *American Journal of Respiratory and Critical Care Medicine,* vol. 169, no. 7, pp. 791-800, 2004, doi: 10.1164/rccm.200301-133OC.

[150] S. Lindgren, H. Odenstedt, C. Olegård, S. Söndergaard, S. Lundin, and O. Stenqvist, "Regional lung derecruitment after endotracheal suction during volume- or pressure-controlled ventilation: a study using electric impedance tomography," *Intensive Care Medicine,* journal article vol. 33, no. 1, pp. 172-180, January 01 2007, doi: 10.1007/s00134-006-0425-x.

[151] S. Leonhardt and B. Lachmann, "Electrical impedance tomography: the holy grail of ventilation and perfusion monitoring?," *Intensive Care Medicine,* journal article vol. 38, no. 12, pp. 1917-1929, December 01 2012, doi: 10.1007/s00134-012-2684-z.

[152] T. I. Oh *et al.*, "Validation of a multi-frequency electrical impedance tomography (mfEIT) system KHU Mark1: impedance spectroscopy and time-difference imaging," *Physiological Measurement,* Article vol. 29, no. 3, pp. 295-307, Mar 2008, doi: 10.1088/0967-3334/29/3/002.

[153] H. Wu, Y. Yang, J. Escudero, and J. Jia, *Feasibility Study of Frequency-difference Electrical Impedance Tomography on Industrial Applications*. 2016.

[154] C. L. Yang, Zhang, T. T., Seo, J. K. and Soleimani, M., "Localized frequency difference EIT for lung tumour monitoring " presented at the The 15th International Conference on Biomedical Applications of Electrical Impedance Tomography, 2014.

[155] A. Borsic, B. Graham, A. Adler, and W. Lionheart, "Total Variation Regularization in Electrical Impedance Tomography," *MANCHESTER,* vol. 1824, 01/01 2007.

[156] J. Sung Chan, K. Jihyeon, L. Jeehyun, W. Eung Je, H. David, and S. Jin Keun, "Frequency-difference EIT (fdEIT) using weighted difference and equivalent homogeneous admittivity: validation by simulation and tank experiment," *Physiological Measurement,* vol. 30, no. 10, p. 1087, 2009. [Online]. Available: http://stacks.iop.org/0967-3334/30/i=10/a=009.

[157] J. Jang and J. K. Seo, "Detection of admittivity anomaly on high-contrast heterogeneous backgrounds using frequency difference eit," *Physiological Measurement,* vol. 36, no. 6, pp. 1179-1192, 2015, doi: 10.1088/0967-3334/36/6/1179.

[158] J. Gao, S. Yue, J. Chen, and H. Wang, "Classification of normal and cancerous lung tissues by electrical impendence tomography," (in eng), *Biomed Mater Eng,* vol. 24, no. 6, pp. 2229-41, 2014, doi: 10.3233/bme-141035.

[159] S. Grimnes and Ø. G. Martinsen, "Chapter 4 - PASSIVE TISSUE ELECTRICAL PROPERTIES," in *Bioimpedance and Bioelectricity Basics (Second Edition)*. New York: Academic Press, 2008, pp. 93-137.

[160] A. Sujin, O. Tong In, J. Sung Chan, S. Jin Keun, and W. Eung Je, "Validation of weighted frequency-difference EIT using a three-dimensional hemisphere model and phantom," *Physiological Measurement,* vol. 32, no. 10, p. 1663, 2011. [Online]. Available: http://stacks.iop.org/0967-3334/32/i=10/a=013.

[161] A. Sujin, O. Tong In, J. Sung Chan, L. Jeehyun, S. Jin Keun, and W. Eung Je, "Weighted frequency-difference EIT measurement of hemisphere phantom," *Journal of Physics: Conference Series,* vol. 224, no. 1, p. 012059, 2010. [Online]. Available: http://stacks.iop.org/1742-6596/224/i=1/a=012059.

[162] O. Tong In, L. Kyung Heon, K. Sang Min, K. Hwan, W. Eung Je, and H. David, "Calibration methods for a multi-channel multi-frequency EIT system," *Physiological Measurement,* vol. 28, no. 10, p. 1175, 2007. [Online]. Available: http://stacks.iop.org/0967-3334/28/i=10/a=004.

[163] T. Khan and S. Ling, "Review on Electrical Impedance Tomography: Artificial Intelligence Methods and its Applications," *Algorithms,* vol. 12, p. 88, 04/26 2019, doi: 10.3390/a12050088.

[164] (2019). *Design and Construction Guidance for foul and surface water sewers offered for adoption under the code for adoption agreements for water and sewerage companies operating wholly or mainly in England*.

[165] M. Wang, W. Yin, and N. Holliday, "A highly adaptive electrical impedance sensing system for flow measurement," *Measurement Science and Technology,* vol. 13, no. 12, pp. 1884-1889, 2002/11/04 2002, doi: 10.1088/0957-0233/13/12/311.

[166] Y. Z. Ma, Zhichu. Xu, Lian Yong. Liu, Xiaoping. Wu, Yingxiang, "Application of electrical resistance tomography system to monitor gas/liquid two-phase flow in a horizontal pipe," in *Flow Measurement and Instrumentation* 2001.

[167] S. Ren, F. Dong, C. Tan, and Y. Xu, "A boundary element approach to estimate the free surface in stratified two-phase flow," *Measurement Science and Technology,* vol. 23, no. 10, p. 105401, 2012/08/01 2012, doi: 10.1088/0957-0233/23/10/105401.

[168] J. Zhao and F. Dong, "Image reconstruction methods for two-phase stratified flow with incomplete data of ERT," *Yi Qi Yi Biao Xue Bao/Chinese Journal of Scientific Instrument,* Article vol. 35, no. 11, pp. 2574-2581, 2014. [Online]. Available: https://www.scopus.com/inward/record.uri?eid=2-s2.0-84919482236&partnerID=40&md5=535269a9b2a1322d05998d9e872fa065.

[169] F. Qianqian, P. M. Meaney, and K. D. Paulsen, "Singular value analysis of the Jacobian matrix in microwave image reconstruction," *IEEE Transactions on Antennas and Propagation,* vol. 54, no. 8, pp. 2371-2380, 2006, doi: 10.1109/TAP.2006.879192.

[170] N. Polydorides and W. R. B. Lionheart, "A Matlab toolkit for three-dimensional electrical impedance tomography: a contribution to the Electrical Impedance and Diffuse Optical

Reconstruction Software project," *Measurement Science and Technology,* vol. 13, no. 12, pp. 1871-1883, 2002/11/04 2002, doi: 10.1088/0957-0233/13/12/310.

[171] S. Liu, R. Cao, Y. Huang, T. Ouypornkochagorn, and J. Jia, "Time Sequence Learning for Electrical Impedance Tomography Using Bayesian Spatiotemporal Priors," *IEEE Transactions on Instrumentation and Measurement,* pp. 1-1, 2020, doi: 10.1109/TIM.2020.2972172.